Summer 8-6-2019

Investigation of the Electrode Polarization Effect for Biosensor Applications

Anil Koklu
Southern Methodist University, akoklu@smu.edu

INVESTIGATION OF THE ELECTRODE POLARIZATION EFFECT FOR BIOSENSOR APPLICATIONS

Approved by:

_____
Prof. Ali Beskok
Professor of Mechanical Engineering

_____
Prof. Vladimir Ajaev
Professor of Mathematics

_____
Prof. Peter Raad
Professor of Mechanical Engineering

_____
Prof. Paul S. Krueger
Professor of Mechanical Engineering

_____
Prof. MinJun Kim
Professor of Mechanical Engineering

INVESTIGATION OF THE ELECTRODE POLARIZATION EFFECT FOR BIOSENSOR APPLICATIONS

A Dissertation Presented to the Graduate Faculty of

Lyle School of Engineering

Southern Methodist University

in

Partial Fulfillment of the Requirements

for the degree of

Doctor of Philosophy

with a

Major in Mechanical Engineering

by

Anil Koklu

(B.Sc., Mechanical Engineering, Istanbul Technical University, Turkey, 2014)
(M.Sc., Mechanical Engineering, Southern Methodist University, USA, 2015)

August 6, 2019

Acknowledgements

I would like to thank to my dissertation advisor Prof. Ali Beşkök, for his incessant support through my graduate studies as well as his mentoring, encouragements and his friendship during this period. He has been always helpful and kind in my all-academic and non-academic activities. This thesis would not have been accomplished without his wise advices. Furthermore, without him, I would not have had the chance to meet exceptional people that I have met through my graduate years. I am also very grateful to Prof. Vladimir Ajaev for his scientific advice and knowledge and my insightful discussions and suggestions. I also would like to thank my other advisory committee members, Professors Peter Raad, Paul S. Krueger, and MinJun Kim for their contributions in this dissertation.

Additionally, I would like to especially thank to Prof. Ahmet Can Sabuncu for his guidance and friendship, with whom I worked closely and frequently shared ideas and discussed about our common research interests. I am also grateful for much invaluable help and support of our current and past group members namely Alper Tunga Celebi, Amin Mansoorifar, Barbaros Cetin, Chinh Nguyen, Jafar Ghorbanian, and Yigit Akkus. I also would like to thank Roy Beavers for his support to my research.

Finally, a special thanks to my family without their love and support this dissertation would not exist.

Koklu, Anil B.Sc., Istanbul Technical University, Turkey, 2014
M.Sc., Southern Methodist University, USA, 2015

Investigation of The Electrode Polarization Effect for Biosensor Applications

Advisor: Professor Ali Beskok

Doctor of Philosophy conferred August 6, 2019
Dissertation completed May 31, 2019

My research focuses on electrokinetic transport. Particularly, in this dissertation, we focus on fabrication and testing of micro electrodes with nanostructured surfaces to minimize the electrode polarization (EP) effects for biosensor applications. In the first study, electrochemical deposition of gold nanoparticles on to planar gold electrodes was used to generate rough surfaces. Dendritic nanostructures that reduced EP up to two orders of magnitude was obtained by optimizing the deposition conditions. These structures also enhanced dielectrophoresis (DEP) response of our bio-chips, making them usable in physiological buffers. In further studies we discovered a *universal scaling* of EP in the frequency domain, which reduced hundreds of dimensional impedance vs frequency experimental data to a single nondimensional equation. This finding is crucial, since one can now determine EP effects for any electrode size and buffer conductivity before electrode fabrication and experimentation. We also showed that the universal scaling applies to the dendritic nanostructured electrodes, which behaves like planar electrodes in much lower conductivity solutions with larger electric double layer thickness.

TABLE OF CONTENTS

LIST OF FIGURES

Chapter 1

INTRODUCTION

When a solid surface is in contact with a polarizable electrolyte solution, surface charges form at the liquid/solid boundary. The electrical state of a charged surface is determined by the spatial distribution of ions in its vicinity. Such a distribution of charges at electrode/electrolyte interface has traditionally been called the electrical double layer (EDL). Understanding the time-dependent formation of EDL in response to varying external effects is a fundamental problem in diverse fields such as electrochemistry [1], colloid sciences [2], biophysics [3], and micro/nanofluidics [4]. The properties and structure of EDL determine the feasibility of applications including biosensors [5], supercapacitors [6, 7], desalination devices [8-10], blue engines [11], and thermocapacitive heat to current converters [12]. These applications are used for impedance spectroscopy [13, 14], micro/nanoparticles detection [15], fuel cells [16], capacitive energy storage [17], capacitive deionization of water [18], and energy harvesting technologies [19].

Impedance characterization at the electrode/electrolyte interface is of great importance in the fields of impedance-based biosensing [20-27], neuro prostheses [28], vitro communication with electrogenic cells [29], rechargeble lithium-ion batteries [30, 31], and most recently for *in vivo* energy sources to power implantable devices [32, 33]. Due to low cost, low power, non-invasive, and ease of miniaturization, impedance based sensors pose many advantages for applications, where decreasing size and cost are crucial, such as in point-of-care diagnostics and biowarfare agent detection. Moreover, they can be easily integrated into microfluidic platforms [34-38].

Microfluidics based impedance spectroscopy offers many advantages over the conventional methods for detection of cells, pathogenic bacteria, toxigenic substances, etc., in food and water matrices [23, 24, 39, 40]. In addition to cell detection, impedance measurements over a wide frequency range can provide information on membrane, cytoplasm, and nucleoplasm dielectric properties [41, 42]. Despite all these advantages, microelectrodes are often limited in performance at the low frequency spectrum in biologically relevant media, which are of predominant interest in physiological research. This limitation arises from the well-known electrode polarization (EP) phenomenon [43-45]. Application of an electric potential to the electrodes induces ion accumulation on electrodes that are in contact with an electrolyte. EP is the large interfacial impedance that forms at the electrode/electrolyte interface, which results in a large electric potential drop and decrease in the overall sensitivity and accuracy of the measurements [46, 47]. In the case of miniaturized electrodes, this effect can lead to small capacitance values causing enormous impedances which deteriorate the measurements, particularly at low AC frequencies.

It is well-known that the interfacial impedance is influenced by the geometry and surface morphology of the electrode, as well as its chemistry (reactive surface groups or atoms) [48, 49]. Due to their simple geometry and common use, several research groups have focused on the characterization of EP for circular (disk) electrodes. Newman provided a relation for the impedance response of disk electrodes, where the capacitance and Ohmic resistance are functions of the applied frequency [50]. Ahuja et al. [51] confirmed this relation by performing impedance measurements using different diameter platinum disk electrodes and have shown that impedance scales inversely with the diameter in the high

frequency spectrum ($\sim$ 1MHz). Hasni et al. [52] also investigated the electrode size effects on impedance spectra using gold disk electrodes immersed in phosphate buffer saline (PBS, $\sigma_{PBS} = 1.5\ S/m$) solution and their results were also consistent with Newman's relation. The influence of electrode surface morphology on the impedance spectra was studied by Alexander et al. [53-55] using finite element simulations, and the surface enlargement factor obtained by dividing the effective polarizable surface area by the electrode foot-print area was shown to directly affect the electric double layer (EDL) charging time. Optimization of electrode geometry and its surface morphology have been the subject of much research with the interest of diminishing the EP effect [56, 57]. Since the EP effect can be very diverse, there is no widely accepted simple correction method to minimize it and various techniques are used such as variation of the inter-electrode separation [43, 44, 58], four electrode designs [59, 60], and high surface area electrodes [46, 49, 61]. One of the methods to minimize the EP effect is to utilize large electrodes but this results in increasing the device size and sample volume required for the measurements [62]. Therefore, the most effective and reliable way to reduce the EP effect is maximizing the interfacial surface area by generating complex nanostructures on the smooth electrode surfaces so that small electrode sizes suitable for microfluidic applications are maintained. Among a wide variety of techniques, electrochemical deposition has become an attractive nanofabrication technique for many emerging fields of technology with the recent developments because of its ease of control, highly pure depositions, and simple operation [63-66]. In electrochemical deposition, the growth rate can be readily and independently controlled by deposition potential without changing the concentration of the reactants [67-74].

Due to their unique physical and chemical properties, gold nanostructures (GNs) have been used in many diverse fields such as biosensors, catalysis, nanoelectronics, plasmonics, biomedicine, surface-enhanced Raman scattering (SERS), impedance spectroscopy, dielectric spectroscopy, and dielectrophoresis [75-78]. GNs enhance nanoscale topological complexity on the surface of electrodes and reduce EP effects by increasing the effective surface area [46]. Recently, it has been shown that GNs can preserve their mechanical and electrical characteristics under mechanical contact for long term electrical measurements [46]. Moreover, the good bio-compatibility characteristics of GNs make them an excellent material for biological measurements compared to other chemically deposited nano-materials [46]. The intrinsic properties of GNs largely depend on their size and shape, and these properties can be tuned through control of morphology and structure [64, 79-85]. Among the many morphologies investigated, the dendritic shaped nanostructures have attracted great attention over the last decade due to their unique properties originating in their shape and their potential impact on new technologies [86, 87]. Because of their higher structural complexity, compared to nanospheres, nanowires and nanodiscs, these branched nanostructures are expected to have a wide range of technological applications. Effective manufacturing of GNs is an essential step towards applying nanoscale fabrication to complex functional devices. However, growing dendritic nanostructures effectively is still a challenge [88-90]. In order to address this challenge, optimization of the deposition conditions is required by changing the applied potential and duration time.

Electrodes with nanostructures and tailored morphology hold great promise to enhance the energy and power densities of electrical energy storage devices [91, 92]. Therefore, in the past few years, much effort has been devoted to generate well-ordered arrays of low-

dimensional nanomaterials such as nanorods with high density and aspect ratio. Many different methods, which involve vacuum evaporation [93], magnetron sputtering [94], electroplating [95], ion beam chemical vapor deposition [96], nanolithography [97], electro-spinning [98], electrophoretic deposition [99], mechanical drawing [100], and template assisted electrochemical deposition [101, 102], have been applied for fabrication of metallic nanorods. Among these, the template assisted electrochemical deposition approach seems to be the most appropriate method for the fabrication of highly ordered, vertically aligned nanorod arrays in a fast and cost effective fashion [102]. The great advantage of the template assisted electrodeposition technique is its ability to control the length, diameter and chemical composition of the nanorods [102].

There is also a growing demand to understand the dynamics of EP. The equations used to investigate the EP behavior are highly nonlinear and contain multiple time scales due to the different physical effects. The starting point for analytical models of EP dynamics in electrolytes are the Poisson-Nernst-Planck (PNP) equations, a set of coupled partial differential equations that capture the time-varying electric potential and ionic concentrations [103-106]. The distribution of electrical potential and ion concentrations in the diffuse layer for an ideally polarizable electrode was derived originally by Gouy [107] and Chapman [108] assuming equilibrium, although several important aspects of physics of electrode/electrolyte interfaces were elucidated much earlier by Helmholtz [109]. The two most natural relaxation times controlling the evolution in electrochemical parallel plate systems are the Debye time (λ^2/D) and bulk time scale (L^2/D), where D is the diffusion coefficients of chemical species, and λ and L correspond to Debye length and bulk length scales, respectively. The seminal paper of Bazant et al [110] considers a situation when an

electrode is subject to a suddenly applied DC potential. The authors show that the system initially behaves like an RC circuit with a response time of $\lambda_D L/D$, where λ_D is the Debye length, L is the electrode separation distance, and D is the ionic diffusivity. Later studies have considered electrode porosity [111], electrode heterogeneities [112], adsorption [113], and Faradaic reactions [114] at the electrode surfaces. Furthermore, various analytical and numerical techniques have been used to study the PNP equations at large applied potentials which are of interest for supercapacitor applications [115]. In contrast, the present study focuses on electrodes subjected to an applied AC potential smaller in amplitude than the thermal voltage ($V_{thermal} = 25\ mV$). The low applied potential limit is relevant for most biomicrofluidic applications [116-118] [119] which justifies consideration of the problem using the linear approximation for the underlying evolution equations. Under the low applied potential condition, the linearization of the PNP equations leads to the Debye-Falkenhagen (DF) equation [120]. An important advantage of this approach is that one can solve for the space charge density instead of solving for ion concentrations and potential distribution separately. Furthermore, linearity of the governing equations opens up the possibility of using analytical methods [110].

However, the EDL charging time scale needs to be modified for porous electrodes. The elements that affect time scales for porous electrodes are the structural factors including thickness, composition, porosity and tortuosity [30, 121]. Porous electrode theory, pioneered by J. Newman and collaborators, provides the standard modeling framework for electrochemical cell simulations [122]. Porous electrode theories utilize a number of assumptions regarding the morphology of the electrochemical cells. The electrode materials are assumed to be made out of spherical, cylindrical or planar particles with

predetermined sizes [110, 123-126]. The porous electrode theory equations were derived using mass and charge conservation equations combined with the Nernst-Planck equation and a modified form of the Butler-Volmer equation [121]. Although much progress has been made in distinct communities, the porous electrode theory is not yet widely adopted, and it may not be appropriate for randomly grown nanostructures presented in this study.

In this thesis, the EP effect is investigated and its characteristic time scales for planar and porous gold electrodes are presented for biosensor applications. I present the theory of charge equilibrium models in section 2. In section 3, I first present the materials and methods, followed with the theory of microfluidic impedance spectroscopy. Then, the optimization of electrochemical deposition conditions in terms of EP reduction is discussed using constant phase element (CPE) model parameters. Changing of the shape and density of GNs at different applied voltages are explained using Nernst equilibrium. Wettability of electrodes coated at different electric potentials is examined using contact angle (CA) measurements. The sequence of dendritic shape GNs growth is investigated using scanning electron microscopy (SEM). The effects of electrode size and surface morphology on EP are discussed, and enhancement of device performance is shown by generating the Jurkat cells suspension spectrum. Finally, conclusions are presented. In section 4, I first describe the charging time scale and experimentally proved that EP exhibits a universal trend, when normalized by a proper impedance magnitude and time scale, resulting in a self-similar behavior for parallel plate capacitor configuration. Next, we performed unsteady one dimensional finite element simulations of the fully coupled PNP equations and numerically verified our experimental observations. I investigated the behavior of porous gold electrodes and showed that EP of porous electrodes in high conductivity buffers behave

like EP of planar electrodes in low conductivity media. Finally, a constant phase element (CPE) model is used to account for the self-similar impedance spectra. The resulting formula can be used for different channel heights and solution conductivities having prior information on electrodes configuration and effective electric Debye layer thickness. In section 5, an analytical model based on the DF equation is developed and shown to be applicable for a wide range of frequencies. In the limit of thin EDL, the well-known relaxation timescale ($\tau_c = \lambda_D L/D$) is recovered. We then nondimensionalize the experimental data based on the conclusions of the model and show that universal behavior for space charge density and impedance expressions is observed over many orders of magnitude in the applied electric field frequency. The analytical results are in excellent agreement with numerical and experimental findings for various channel heights and solution concentrations. Based on the results, one can obtain the space charge density for a given applied AC voltage and construct a relation between experimentally measured impedance and corresponding space charge density. In section 6, the influence of electrode geometry on the impedance response was investigated and the characteristic time scale was defined in terms of the electrode diameter, Debye length, ionic diffusion coefficient, and surface enlargement factor for the planar and nanorod structured disk electrodes. This study focuses on validating proposed time scales to obtain self-similar impedance spectra using both experimental measurements and numerical simulation. The last section is organized as follows: the Materials and Methods section outlines the electrode fabrication processes and impedance measurements. Next, unsteady 2D axisymmetric fully coupled Poisson-Nernst-Planck (PNP) equations were solved using COMSOL for planar and nanorod coated electrodes. Cyclic voltammetry (CV) was used to attain the surface enlargement factor for

nanorod structured disk electrodes. Finally, a constant phase element (CPE) model was used to demonstrate self-similar behavior of normalized impedance spectra, which can be used for different potassium chloride (KCl) solution conductivities, electrode sizes and nanostructured electrodes with no EDL overlap.

Chapter 2

THEORY

In this section, the basic theory behind electrode polarization (EP) is explained.

2.1. Equilibrium Models

2.1.1. Helmholtz Model

Helmholtz [109] was the first to introduce the concept of electric double layer (EDL). He comprehended that electrodes immersed in electrolyte solutions repel the co-ions while attracting counter-ions to their surfaces. The compact layer of charges forming at the electrode/electrolyte interfaces was defined as EDL. Figure 2.1a shows a schematic of the EDL structure formed near the surface of a positively charged electrode as envisioned by Helmholtz [127-129]. In the Helmholtz model, all the counter-ions were assumed to be attached at the electrode surface and they were treated as immobile ions [129]. This structure is equivalent to that of conventional dielectric capacitors with two planar electrodes separated by a distance H [129].

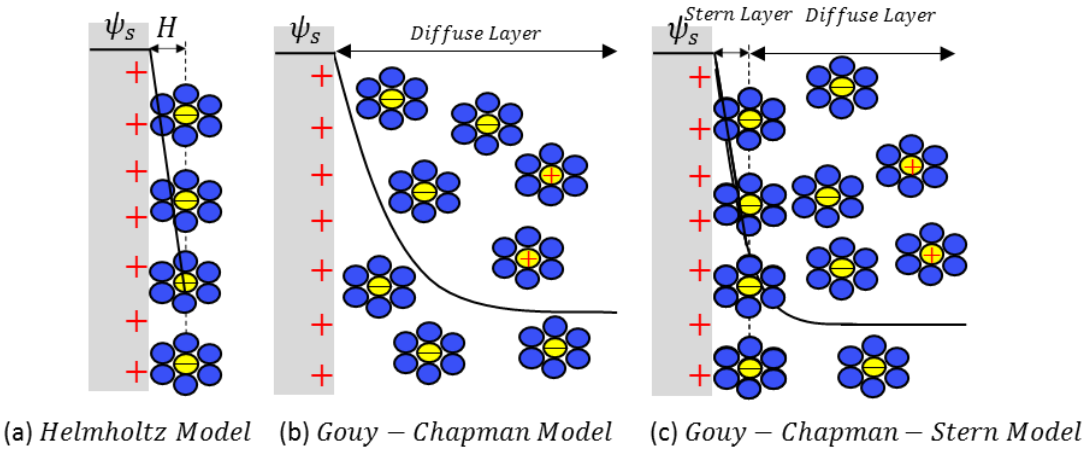

Figure 2.1. Schematics of the EDL structure showing the arrangement of solvated anions and cations near the electrode/electrolyte interface. (a) Helmholtz model, (b) Gouy-Chapman model, and (c) Gouy-Chapman-Stern model.

Therefore, the capacitance per unit surface area of the Helmholtz EDLS denoted by C_s^H (F/m^2) is given by [130, 131],

$$C_s^H = \frac{\varepsilon_0 \varepsilon_r}{H} \tag{2.1}$$

where ε_0 and ε_r are the free space permittivity and the relative permittivity of the electrolyte solutions, respectively. The thickness H of the Helmholtz EDL can be approximated as the radius of solvated ions [132].

2.1.2 Gouy-Chapman Model

Gouy [133] and Chapman [108] considered the EDL model proposed by Helmholtz accounting for the fact that the ions are mobile in the electrolyte solutions and are driven

by the effect of both diffusion and electrostatic forces [132]. The layer which contains the mobile ions was described as diffuse layer shown in Figure 2.1b. In this model, the ions are treated as point-charges and the equilibrium concentration c_i of ion species "i" is obtained by the Boltzmann distribution as [134, 135] ,

$$c_i = c_{i\infty} \exp\left(\frac{-z_i e\psi}{k_B T}\right) \tag{2.2}$$

where z_i and $c_{i\infty}$ are the valence and bulk molar concentration of ion species "i", respectively. The temperature is denoted by T, ψ is the potential, e is the electron charge, while k_B is the Boltzmann constant ($k_B = 1.381 \times 10^{-23}\ m^2 kg K^{-1} s^{-2}$). In the Gouy-Chapman model, the formation of the local electric potential is governed by the Poisson-Boltzmann (PB) equation assuming constant electrolyte permittivity [135]. For binary, symmetric electrolytes, valances and concentration of ions can be written as, $z_1 = -z_2 = z$ and $c_{1\infty} = c_{2\infty} = c_\infty$. Then, the PB equation is expressed as [135],

$$\nabla \cdot (\varepsilon_0 \varepsilon_r \nabla\psi) = 2zeN_A c_\infty \sinh\left(\frac{ze\psi}{k_B T}\right) \tag{2.3}$$

where N_A is the Avogadro's number ($N_A = 6.022 \times 10^{23}\ mol^{-1}$).

For planar surface electrodes and constant electrolyte properties, the exact solution of Equation (2.3) was derived by Debye-Falkenhagen for the direct current (DC) potential case by applying the following boundary conditions (i) $\psi(0) = \psi_D$ and (ii) $\psi(\infty) = 0$. Then, the specific capacitance corresponding to the diffuse layer C_s^D is given by [135],

$$C_s^D = \frac{q_s}{\psi_D} = \frac{4zeN_A c_\infty \lambda_D}{\psi_D} \sinh\left(\frac{ze\psi_D}{2k_B T}\right) \tag{2.4}$$

where q_s is the surface charge density and λ_D is the Debye length for symmetric electrolytes defined as $\lambda_D = (\varepsilon_0 \varepsilon_r k_B T / 2e^2 z^2 N_A c_\infty)^{1/2}$ [135].

2.1.3 Gouy-Chapman-Stern Model

Stern [92] combined the Helmholtz model and the Gouy-Chapman model and described the EDL as two layers (Figure 2.1c), namely: (i) the Stern layer (or Helmholtz layer or compact layer), referring to the immobile ions attached to the electrode surface, and (ii) the diffuse layer where the ions are mobile as Gouy-Chapman model [Equation (2.3)] states [135]. The total EDL consists of the Stern layer and diffuse layer capacitances in series [2]. Gouy-Chapman-Stern (GCS) model for symmetric electrolytes is expressed as [136] for grounded and sinusoidally excited electrodes ,

$$\nabla \cdot (\varepsilon_0 \varepsilon_r \nabla \psi) = \begin{cases} 0 \\ 2ze N_A c_\infty \sinh\left(\dfrac{ze\psi}{k_B T}\right) \end{cases} \tag{2.5}$$

2.1.4 Modified Poisson-Boltzmann Models

The point-charge assumption associated with the PB equation [Equations (2.3) and (2.5)] is only valid for relatively low ion concentration c_∞ and low electric potential [129]. In fact, the ions have finite size and hence, a maximum ion concentration c_{max} exists corresponding to the closed packing of ions. The maximum ion concentration can be obtained by $c_{max} = 1/(N_A a^3)$ which corresponds to cubic packing of ions with effective diameter a [137].

Many studies have been reported to comprise the effect of finite ion size in the electrolyte solution [138, 139]. Among all of them, the modified Poisson-Boltzmann (MPB) models based on the local-density and mean-field approximations are relatively convenient both mathematically and numerically [139]. Bikerman [140] established the first equilibrium MPB model including finite ion size. This model pertains to electrolytes with anions and cations having different volumes but symmetric valence. Borukhov *et al.* [141] and Silalahi *et al.* [142] developed MPB models valid for binary electrolytes with asymmetric valence for same ion diameters. Later on, they extended the models to binary asymmetric electrolytes with unequal ion diameters [143, 144]. Biesheuvel and co-workers [144, 145] and Alijo *et al.* [146] created more general MPB models valid for even asymmetric electrolytes and/or multiple ion species with different ion sizes and valencies. This was achieved by considering an excess chemical potential term based on the Boublik-Mansoori Carnahan-Starling-Leland equation-of-state. It relates the excess chemical potential to the local ion concentrations, effective diameters of ions, and their volumes [146]. Moreover, Tresset [147] developed a more general model, which is called as Poisson-Fermi model, for asymmetric electrolytes and multiple ion species based on the Lattice-Boltzmann approach by assuming different volumes of ions. In addition, Li and co-workers [148, 149] expanded the model for asymmetric electrolytes based on the variation principle while considering the finite sizes of both ions and solvent molecules. Alternatively, Horno and coworkers [150, 151] developed a MPB model for asymmetric electrolytes by directly applying a “Langmuir-type” correction to the equilibrium ion concentration given by the Boltzmann distribution.

For binary and symmetric electrolytes, the MPB models were reduced by M. Bazant and his coworkers to [141, 152],

$$\nabla \cdot (\varepsilon_0 \varepsilon_r \nabla \psi) = \frac{2zeN_A c_\infty sinh\left(\frac{ze\psi}{k_B T}\right)}{1+2\upsilon_p sinh^2\left(\frac{ze\psi}{2k_B T}\right)} \tag{2.6}$$

where the packing parameter is defined as $\upsilon_p = 2a^3 N_A c_\infty = 2c_\infty / c_{max}$ [152]. The term "MPB model" will be used to refer to Equation (2.6). As it can be understood by equation 2.6, for the case that $a = 0$ nm and $\upsilon_p = 0$, MPB model reduces to the Gouy-Chapman model given by Equation (2.3). For planar surface electrodes and constant electrolyte properties, the surface charge density and diffuse layer specific capacitance are given by [137],

$$C_s^D = \frac{q_s}{\psi_D} = \frac{2zeN_A c_\infty \lambda_D}{\psi_D} \sqrt{\frac{2}{\upsilon_p} \log\left[1 + 2\upsilon_p sinh^2\left(\frac{ze\psi_D}{2k_B T}\right)\right]} \tag{2.8}$$

Note that when $\psi_D = 0$, Equation (2.8) predicts an extremum for the diffuse layer capacitance, i.e.,$C_s^D = \varepsilon_0 \varepsilon_r / \lambda_D$ (based Tylor expansion). This capacitance could be either a maximum or a minimum value depending on the packing parameter υ_p as discussed in Refs. [139, 153].

2.2 Dynamic Models

Equivalent RC circuit models have been widely used to investigate the performance of biosensors. However, equivalent RC circuit models require prior knowledge of macroscopic parameters such as the resistance and capacitance of the device which are

typically determined experimentally or by other methods. In fact, these models are typically used to fit the experimental data [154-156] rather than predict the performance of biosensors. Moreover, the classical RC circuit models inherently neglect ion diffusion and non-uniform ion concentration in the electrolyte [110, 157, 158] which are significant for high concentration of electrolyte and high applied voltages. Therefore, the aforementioned models can be used for biosensor application where the applied voltages is quite low and concentration of physiological solutions are still in the range of mathematical models. However, they may not be valid for supercapacitor applications due to high applied voltages and concentration of ions[157-159].

2.2.1 Poisson-Nernst-Planck Model

The classical Poisson-Nernst-Planck (PNP) model governs the transient electric potential and ion concentration profiles in the diffuse layer [127, 160, 161]. It is expressed as,

$$\nabla \cdot (\varepsilon_0 \varepsilon_r \nabla \psi) = -\sum_{i=1}^{N} z_i N_A c_i \tag{2.9a}$$

$$\frac{\partial c_i}{\partial t} = \nabla \cdot \left(D_i \nabla c_i + \frac{z_i D_i}{R_u T} F c_i \nabla \psi - c_i \boldsymbol{u} \right) \tag{2.9b}$$

where t is time and c_i is the molar concentration for ion species i, respectively. Here, D_i is the mass diffusion coefficient of ion species i (m^2/s), $F = eNA = 9.65 \times 10^4$ C/mol is the Faraday constant, $R_u = k_B N_A = 8.314$ J/(K mol) is the universal gas constant and $\boldsymbol{u}$ is the velocity vector of the ions' bulk motion. The three terms in the mass conservation equation given by Equation (2.9b) correspond to [129]: (1) ions' diffusion to their

concentration gradient, (2) ions' migration due to electrostatic force, and (3) advection in the electrolyte due to the bulk motion of ion species, respectively. Note that the Poisson-Nernst-Planck model [Equation 2.9] reduces to the Gouy-Chapman model in steady state and when advection is negligible [162].

The PNP model neglects the finite size of ions and treat ions as point-charges [163, 164]. This assumption breaks down when either the electrolyte concentration or the electric potential is large [164]. Therefore, the PNP model is not valid for practical electric double layer capacitors with typical electrolyte concentration larger than 1 mol/L and potential window larger than 1 V.

2.2.2 Modified Poisson-Nernst-Planck Models

Recent efforts have been made to account for the effect of finite ion size in modeling ion transport in concentrated electrolyte solutions and/or under large electric potential [165-169]. For example, Kilic *et al*. [160] derived a modified Poisson-Nernst-Planck (MPNP) model valid for binary and symmetric electrolytes under large electrolyte concentration and electric potential. The authors added an excess term accounting for the entropic contribution due to finite-size ions in the expression of the Helmholtz free energy. This resulted in an excess term in the expressions of the chemical potentials and mass fluxes [158, 170]. Assuming identical diffusion coefficient $D_1 = D_2 = D_3$ and negligible advection effect, the MPNP model is expressed as [170],

$$\nabla \cdot (\varepsilon_0 \varepsilon_r \nabla \psi) = -eN_A z(c_1 - c_2) \tag{2.10a}$$

$$\frac{\partial c_i}{\partial t} = \nabla \cdot \left(D_i \nabla c_i + \frac{z_i D_i}{R_u T} F c_i \nabla \psi - \frac{D N_A a^3 c_i \nabla (c_1 + c_2)}{1 - N_A a^3 (c_1 + c_2)} \right) \tag{2.10b}$$

This MPNP model reduces to the PNP model [Equation (2.9] for vanishing ion diameter, i.e., for $a = 0$. Moreover, the MPNP model reduces to the MPB model [Equation (2.6)] in steady state. Note that this MPNP model does not apply to asymmetric electrolytes or to multiple ion species [163].

Alternatively, several authors [171, 172] incorporated the finite ion size in ion mass fluxes using the activity coefficient to account for the deviation from ideal electrolyte solutions. However, these studies [172, 173] were limited to binary and symmetric electrolytes. Note that the MPNP model developed by Kilic *et al.* [160] [Equation (2.10)] can be also formulated in a form equivalent to that based on the activity coefficient [158].

Davidson and Goulbourne [173] extended the MPNP model to multiple ion species but with symmetric ion diameter and valency. Eisenberg and co-workers [167] developed a MPNP model for binary asymmetric electrolytes based on the variation of principle. Horng *et al.* [169] later extended this model for asymmetric electrolytes with multiple ion species. However, these MPNP models were expressed as integral-differential equations, thus making the numerical solution procedure highly involved particularly for three-dimensional geometries.

2.3 Conclusion

The present chapter first summarized the definitions of integral and differential capacitances as well as their calculation formula in different experimental techniques. Then, it presented an overview of the existing models in the literature for equilibrium and transient simulations of supercapacitors. Limitations associated with these models were also discussed. Simulations of supercapacitors will be performed based on new numerical tools capable of capturing important electrochemical and transport phenomena in supercapacitors and will also be validated with experimental data. Scaling laws governing the performances of EDLCs will also be presented by performing dimensional analysis of the physics-based continuum modeling. Note that more detailed background and current state of knowledge on specific topics will be introduced in the subsequent chapters.

Chapter 3

EFFECT OF ELECTRODE SIZE AND SURFACE MORPHOLOGY ON ELECTRODE POLARIZATION IN PHYSIOLOGICAL BUFFERS

EP is inevitable in high conductivity buffers at low AC frequencies due to the accumulation of free charges at the electrode/electrolyte interface. Electrode miniaturization increases EP effect on impedance measurements. In this chapter, six gold planar (GP) electrodes having different diameters ($100\mu m \leq \phi \leq 4000\mu m$) were used to investigate the size effect on EP with parallel plate electrode geometry. GP electrode surface was electrochemically deposited with gold nanostructures (GNs) to minimize the EP effect. An equivalent circuit model was used to attain electrode/electrolyte interfacial impedance. The constant phase element (CPE) model was used to analyze the effect of the size and morphology of electrodes on EP. The surface morphology of gold nanostructured electrodes was examined using scanning electron microscopy (SEM), and the influence of different applied potential on the growth of GNs was elucidated with Nernst equilibrium condition. Surface roughness and wettability characteristics were examined by performing surface roughness and contact angle measurements, respectively. The improvement of GNs deposited electrode performance was investigated by analytically generated Jurkat cell suspension spectra. The results show that the error in estimating in subcellular properties can be drastically reduced by using GNs deposited electrodes.

3.1. Materials and Methods

3.1.1. Microfabrication, Impedance Measurement and Surface Characterization

Photolithography supplies (photoresists, developers, and remover) were purchased from Microchem Corp. (Westborough, MA, USA). All other chemicals used were of analytical grade and obtained from Sigma-Aldrich (St Louis, MO, USA). Glass slides $2.5\ cm \times 3.75\ cm$ (Gold Seal) were used as the substrate. They were sequentially cleaned in deionized (DI) water, 1 M KOH, acetone, and isopropyl alcohol (IPA) for 10 min in a 25 ℃ ultrasonic bath (FB11201, Fisher Scientific) at 37 kHz, and finally, they were rinsed with DI water. The glass slides were dried with Nitrogen gas following the cleaning steps. They were then put inside a 150 ℃ conventional oven to fully vaporize the water residue. The positive photoresist (S1813) was spin coated on the substrate using a two-step process with the following rotation speeds: 1000 rpm for 10 s and 4000 rpm for 30 s, with 300 rpm/s acceleration/deceleration stages. The substrate was soft baked at 115 °C for 1 min on a hot plate. In the next step, the substrate was exposed to Ultra Violet (UV) light using a negative mask for 10 s at 100 mJ/cm^2 using a mask aligner (Karl Suss, MJB3). The substrate was then immersed into the developer for 17 s (MF-26A). After the substrate was gently washed using DI water and dried with Nitrogen, the substrates were sequentially coated with chromium (Cr) (120 mA—60 s) gold (Au) (80 mA—120 s) layers using a sputter coater (EMS300TD, Emitech). Sputtering generated thin layers of metals on the order of tens of nanometers thick. Finally, disk shape gold electrodes with varying diameters were obtained to investigate the electrode effect on impedance spectra. The

process flow of gold disk electrode fabrication and the microscopy images are shown in Figure 3.1a and 3.1b. Copper tape (3M) was used as terminal ports and was adhered to the gold electrodes using silver conductive epoxy (Silver Epoxy, MG Chemicals). Following this step, the gold electrode surface was modified using an electrochemical deposition technique. A three-electrode configuration, potentiostat system was used for electrochemical deposition (EZstatPro, Nuvant). Gold sputtered electrodes were electrochemically coated with GNs in 1 mg/ml Sodium Tetrachloroaurate (III) ($AuCl_4Na\ 2H_2O$) (Sigma Aldrich) solution using the deposition setup in the potentiostatic mode. Depositions were conducted at varying durations (5-60 min) and electric potentials ranging from -0.3V to -0.9V for 4mm diameter electrode to optimize the deposition condition. 4mm diameter electrodes were chosen for the sake of easy fabrication and alignment. Only the circular part of the gold electrodes was immersed in the solution in order to have a fixed area of deposition by covering the connection pad with a dielectric material (Double Sided Tape). Details of the electrochemical deposition were presented in our previous study [46]. The microfluidic channel was fabricated using double sided tape cut with 70 μm channel height using a craft cutter (Silver Bullet) and it was sandwiched between the two glass slides. Inlet and outlet ports were drilled with a diamond drill bit on glass substrates. Alignment markers on the electrode centerline were used to align the two electrodes on top of each other in the middle region of the microfluidic channel using a mask aligner. Figure 3.1c shows a schematic of the assembled microfluidic device and its connection to an impedance analyzer.

A high precision impedance analyzer (4194A, Agilent) was used to measure the impedance spectrum of a 1.5 S/m conductive phosphate buffer saline (PBS) solution in the 100 Hz-10

MHz frequency range. Microfluidic device was connected to the low and high terminals of the impedance analyzer using a test fixture (HP 16047A) in a 4 terminal configuration [13]. Equivalent circuit analysis was used to extract interfacial impedance [174, 175]. Empirically, the electrode/electrolyte interfacial impedance can be represented in the form of CPE [61, 176-179]. The CPE model is given as $Z_{CPE} = 1/K(i\omega)^{\alpha}$, where K is the CPE parameter ($\Omega^{-1}\, s^{\alpha}$), α is the CPE exponent, ω is the angular frequency, and $i = \sqrt{-1}$. The parameter α changes from zero to one ($0 \leq \alpha \leq 1$), where $\alpha = 0$ and $\alpha = 1$ correspond to purely resistive and purely capacitive impedance, respectively. The exponent α is a function of the temperature, electrode surface characteristics, and the electrolyte type in contact with the electrode. The CPE parameter K and exponent α increase and decrease respectively with the increased surface area. As a result, CPE model enables prediction of surface area changes with examining the K and α values. The details of extracting the CPE parameter and exponent was explained in our previous paper [46].

The equivalent circuit model for extraction of the electrical components of the microfluidic chip is shown in Figure 3.1d. The equivalent circuit model consists of serial combination of Z_{CPE} and Z_{sus} which model the interfacial and cell suspension impedances, respectively. These equivalent circuit elements are in series with electrode lead resistance (R_{lead}) and inductance (L_{lead}). Finally, a parallel capacitance (C_f) is added to account for stray effects. The impedance measurements were conducted with 20 mV AC signal in 100 Hz-10 MHz frequency range. Faradic effects were neglected considering the operation conditions and electrode materials [180].

After electrochemical deposition, surface morphology of GNs electrodes were characterized using SEM (Leo-Zeiss 1450VPSE- resolution~1 nm). Energy dispersive X-

ray spectroscopy (EDS, EDAX Genesis System) was used for elemental analysis and chemical characterization. Non-contact laser profilometer (PS50, Nanovea) was used to measure the surface roughness. Static water contact angles were measured with a high-resolution CCD camera (QImaging, Retiga 4000R) with Navita 12 objective lenses. Digital images were acquired using QCapture pro software (QImaging). The CA was measured from a sessile drop formed from a 6 µl water droplet via a syringe. Determination of CA was performed using the ImageJ software package with DropSnake plugin. CA measurements were performed on at least five different locations on the sample surface and then averaged for statistics.

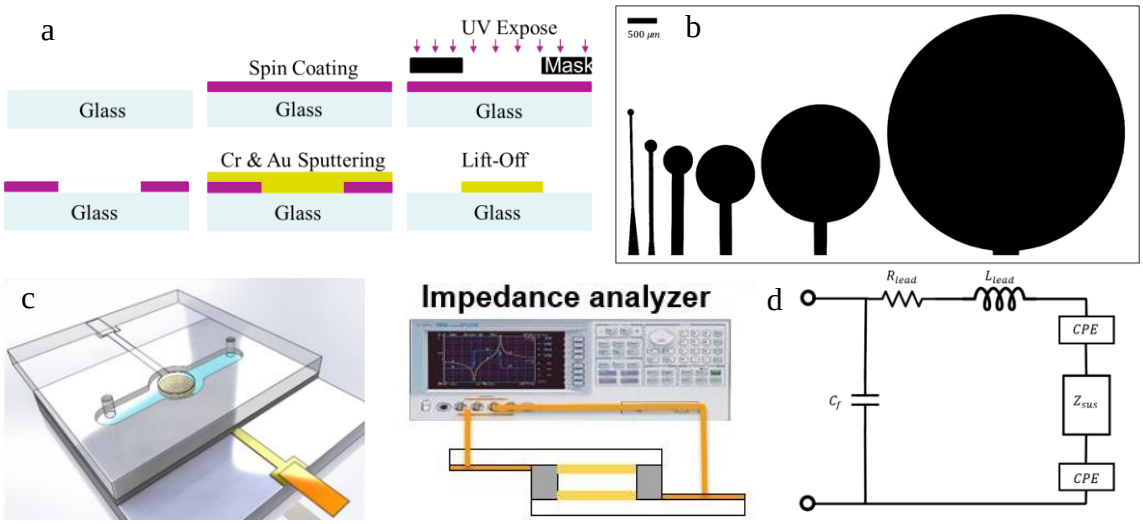

Figure 3.1 a) Process flow of electrode fabrication using photolithography method and b) Microscopy images of different diameter of disc electrodes varying from 100µm to 4000µm. c) A schematic of the microfluidic device connected to an impedance analyzer d) Equivalent circuit model used to analyze the impedance spectrum.

3.2 Results and Discussion

3.2.1. Optimization of Electrode Surface Modification

Electrochemical deposition potential has great influence on the formation of GNs because it is a major parameter in the kinetics of the deposition process. Increasing the electric potential accelerates the kinetics of electrodeposition, which promotes irregular growth of nanostructures. The effect of applied potential on the GNs growth was investigated by Zhang *et. al*, and it was reported that density of GNs coated on the planer surface and the surface roughness increased by increasing the applied potential at constant electrolyte concentration [181]. In this part, their optimum condition for generating dense GNs (-0.3 V-1800s) was used as an initial condition to increase the effective surface area. The surface of 4 mm diameter gold planar (GP) electrode was modified at different conditions with GNs to find the optimum electrochemical deposition condition for the purpose of maximizing the effective surface area. Varying deposition time (600 s, 900 s, 1200 s, 1800 s, 2100 s, 2700 s and 3600 s) and voltages (−0.3 V, −0.7 V, and -0.9 V) were tested to generate GNs electrodes. The SEM images of GNs at different applied potentials are shown in Figure 3.2. At the lowest applied potential and the highest deposition time (-0.3V-3600s), synthesized GNs consists of a large quantity of well-dispersed nanostructures. The morphology of the GNs is revealed as stem type tectorum nanostructures (Figure 3.2a) [67]. Increasing the applied voltage to –0.7V, a layer of fern leaf type dendritic GNs is obtained with high density (Figure 3.2b) [79]. At -0.9 V, the GNs become rounded structure nanoparticles (Figure 3.2c) and the density of nanostructures decreases, as previously reported [79]. The chemical composition of the electrode deposited at -0.7 V

for 3600s is shown in Figure 3.3 as a representation. For electrodes with GNs, the chemical content of gold obtained was about 97%. The remaining 3% of the composition was silicon, which is the main element for the glass substrate. The reason could be the thickness of gold layer which is much smaller than the thickness of glass substrate. The X-ray can partially penetrate to the glass surface and therefore, silicon material can be seen in the energy spectra.

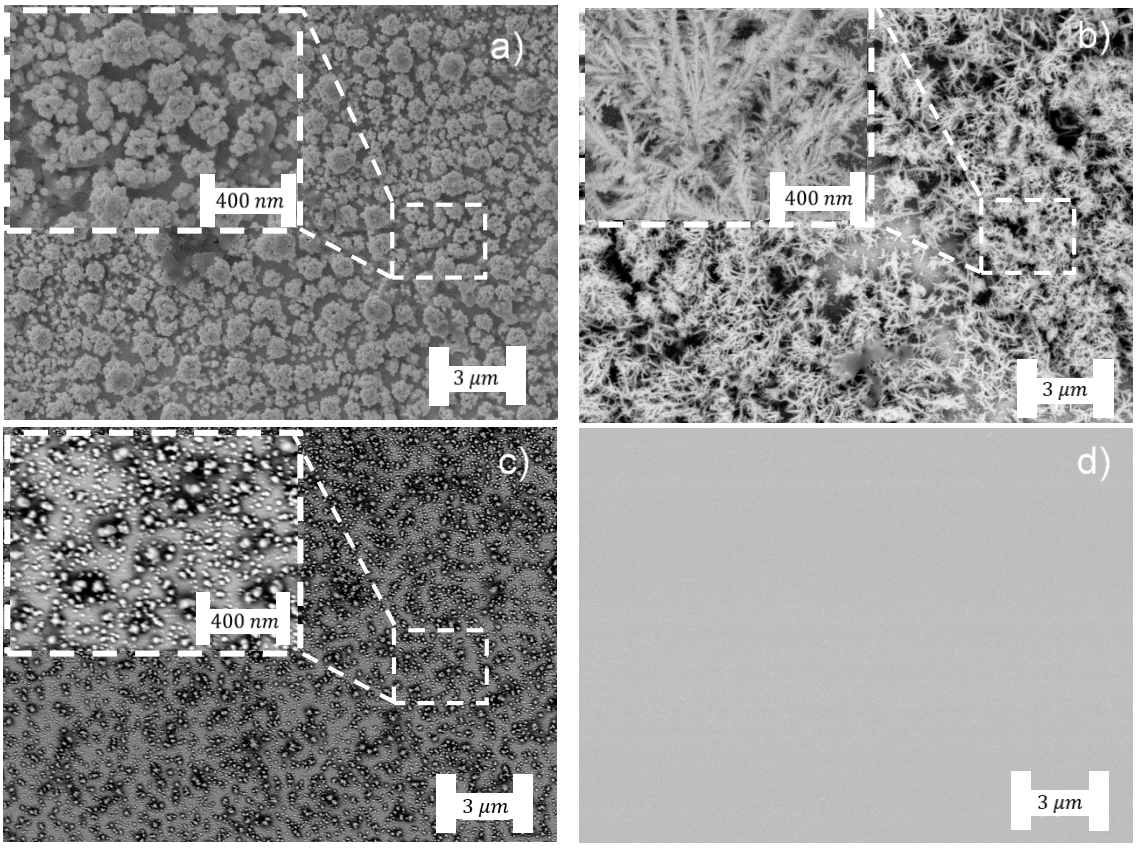

Figure. 3.2. SEM images of GNs electrodeposited on 4 mm diameter gold electrodes for 3,600 s and at potentials of a) -0.3 V, b) -0.7 V, and c) -0.9 V. d) The surface of the GP electrode. The SEM images were taken at 25 kV and a 10,000 magnification factor. The imaging conditions for inset figures are 25 kV and a 30,000 magnification factor.

The variation of nanostructure density and shape can be explained using Nernst equilibrium theory [182]. According to the Nernst equilibrium condition, when the growth potential is close to the Nernst equilibrium potential, GNs dissolves easily due to the negative shift in the reversible potential of the electrode covered by rounded shape gold nanoparticles [183]. Thus, as the growth potential approaches the Nernst equilibrium potential, the particle density on the GP electrode surface decreases (Figure 3.2c).

On the other hand, when the growth potential is well below the Nernst equilibrium potential, many GNs can exist without dissolving into the electrolyte during deposition and therefore, nanostructures density increases on the electrode surface (Figure. 3.2a and 3.2b). Furthermore, GNs can only grow at the lattice plane with the lowest energy site of GNs when the applied potential is small enough. It leads to the formation of spiky dendritic type GNs (Figure 3.2b).

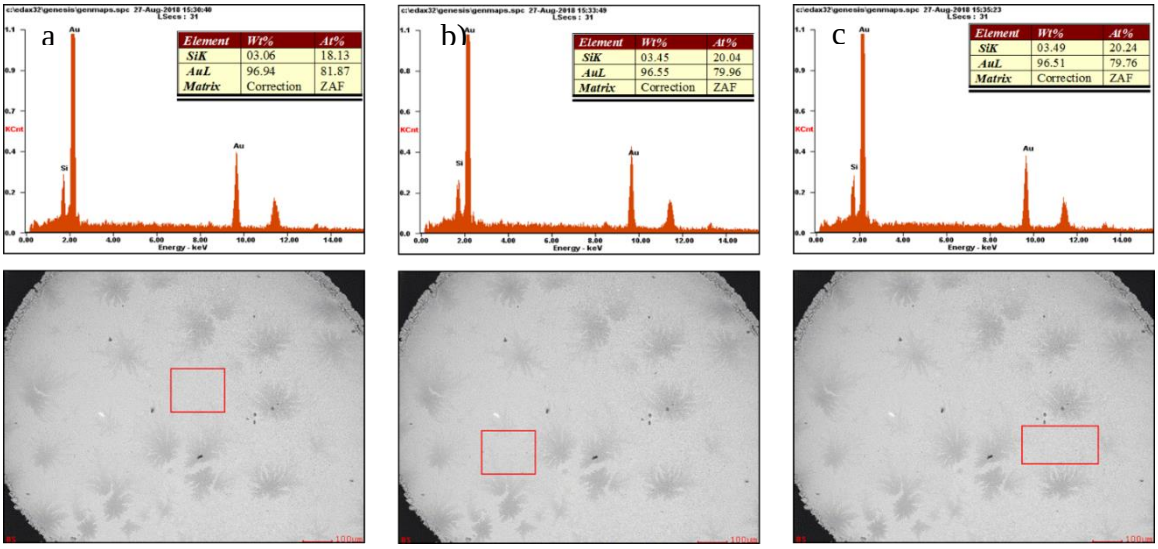

Figure. 3.3. EDS analysis results for GNs deposited electrodes at three different locations.

However, if the growth potential is large enough, the reaction would have enough energy for gold atoms to overcome the energy difference between the lattice planes. Thus, the GNs can grow uniformly in all directions, consequently forming spherical-like gold particles (Figure 3.2c).

3.2.2. Surface Roughness Measurements

Even though SEM images can provide detailed topographical information about the surface, they cannot provide any quantitative information about the surface roughness. For the purpose of measuring the surface roughness, a non-contact laser profilometer was used to measure the surface roughness. The profilometer used has a vertical resolution of 6 nm. The surface roughness was expressed in terms of average surface roughness (R_a) that is defined as the arithmetic mean of height deviations of valleys and peaks with reference to the mean line. In Table 3.1, average surface roughness of different electrodes is tabulated. Results indicate that average roughness increases with applied potential up to -0.7V but it decreases at -0.9V. The results are qualitatively supported by SEM images given in Figure 3.2.

Table 3.1. Surface roughness of GNs electrodes deposited for 60 min in terms of average surface roughness Ra.

Applied Potential (V)	Ra (μm)
-0.3	1.05
-0.7	1.51
-0.9	0.42

3.2.3. Growth Mechanism of Dendrite Gold Nanostructures

Since the surface roughness and complexity of structures were the highest with dendritic GNs at -0.7 V, 3,600s, its EP reduction performance was expected to be the best among other configurations based on the CPE model [184] and surface roughness results. Hence, growth of dendritic GNs were examined at different time lapses to investigate dendritic GNs progression. Figure 3.4 shows the SEM images captured at 25 kV and a 40,000 magnification factor of dendritic GNs at -0.7 V for different coating durations. The images were taken in the vicinity of gold disc electrode center. This figure illustrates the dendritic GNs growth after 30 (a), 45 (b), and 60 (c) minutes, respectively. When charge transfer takes place at the electrode/electrolyte interface, gold ions in the electrolyte move to the electrode surface and start to grow on the active sites of the electrode. At the initial stages of nuclei growth, growth is independent between different active sites.

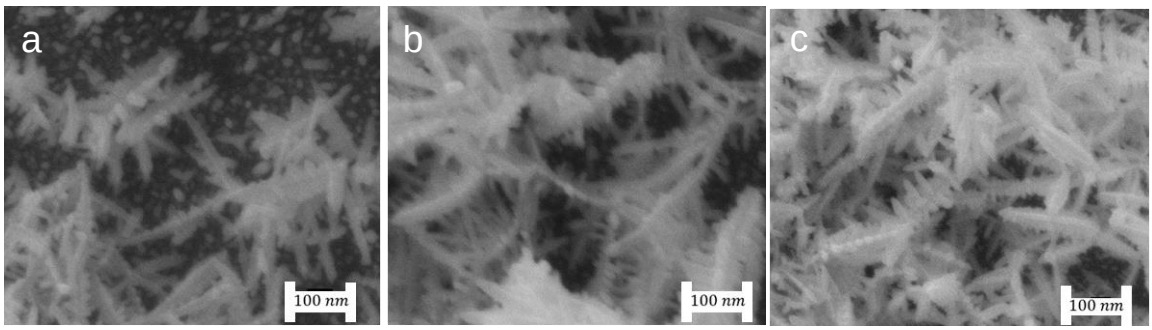

Figure. 3.4. SEM images of GNs electrodes deposited at -0.7 V nucleation potential for duration times of a) 30 min, b) 45 min, and c) 60 min. The SEM images were captured at 25 kV and a 40,000 magnification factor with the back scattering mode.

On the other hand, nuclei do not expand freely in all directions; after a certain time they impinge on each other. Growth stops at the point of contact, resulting in a limitation in size

of the nanostructures. This leads to coalescence which causes two touching gold nanostructured clusters to propagate together. The distance among the GNs clusters was large for 30 min deposition (Figure 3.4a) but it was reduced after 15 min extra deposition (Figure 3.4b). The GNs randomly filled the gap and grew by coalescing with other clusters at 60 min (Figure 3.4c).

3.2.4. Elucidation of Impedance Measurements Based on CPE Parameters

In order to investigate the reduction of EP by increasing the effective surface area, the microfluidic channels with 70 µm channel height were filled with PBS for all GNs electrodes and impedance measurements were performed in the 100 Hz-10 MHz frequency range. Impedance data obtained for each electrode was fitted to the equivalent circuit model. The complex dielectric spectrum of solution and CPE model parameters were extracted. CPE parameters (K and α) were calculated for each electrode using the fitting procedure explained in our previous study [46]. K and α of the GNs deposited 4mm diameter disc electrodes were normalized using K and α of 4mm diameter GP electrode ($K_{control}$ and $\alpha_{control}$). The changes in normalized K and α with deposition time and applied potential are shown in Figure 3.5. At least 5 impedance measurements were performed for a single device and the standard deviation on the calculated K and α values are also shown in Figure 3.5. It can be seen that the value of K significantly increased by GNs deposition. This behavior is an indication of higher effective electrode/electrolyte surface area which is inversely proportional to the impedance [185]. It explains the large decrease of impedance magnitude in the low frequency region. The power factor α for GNs

coated electrodes was decreased, in agreement with the fact that smaller values indicate a rough electrode surface. The extracted values for the planar electrodes were also consistent with the reported values for gold electrodes [186]. The results indicate reduction in α and increase in K at constant potential by both increasing the deposition time and the applied potential.

However, increase in K and decrease in α with respect to the values for GP electrode were reduced above the critical applied potential (-0.7V). A monotonic decrease in the interfacial impedance was observed by increasing time but the deposition time over an hour is not feasible due to practical considerations. Therefore, the constant potential of -0.7 V and deposition time of 60 min were the optimum parameters for decreasing the EP effect, which was expected from the SEM and surface roughness results.

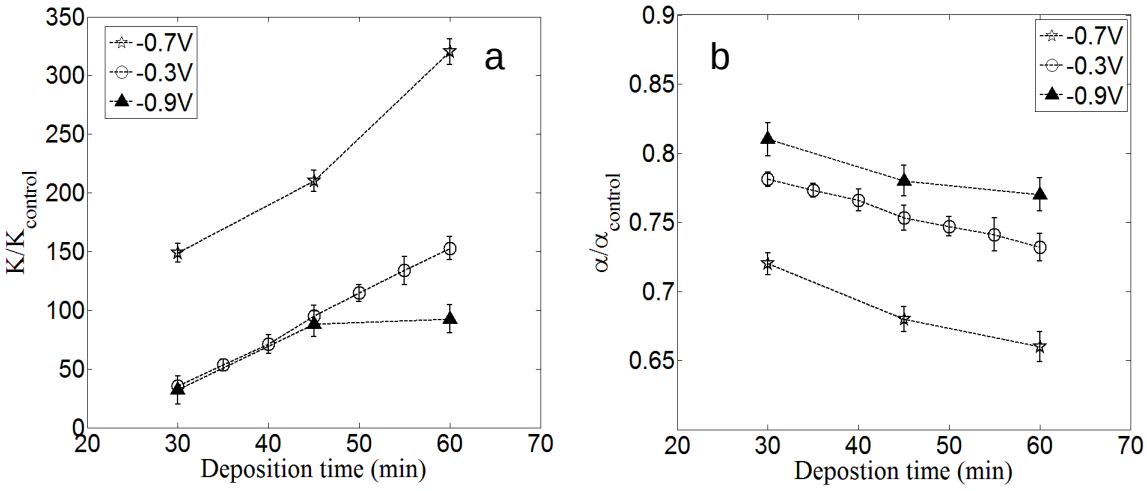

Figure. 3.5. a) Variation of normalized CPE parameter, $K/K_{control}$, and b) normalized CPE exponent, $\alpha/\alpha_{control}$ of GNs electrodes with deposition time. Measurements were taken in a chamber where channel height is 70μm and the electrode diameter was 4 mm. The chamber was filled with PBS (1.5 S/m), and measurements were taken at 100 Hz-10 MHz range. K and α were normalized using control values obtained for planar electrode, where $K_{control} = 4.62 \times 10^{-6} \pm 0.12 \times 10^{-6}$ (Ω^{-1}s) and $\alpha_{control} = 0.83 \pm 0.006$.

3.2.5. The Effect of Wettability on Impedance Measurements

Wettability characteristics of electrodes can also play a critical role for reduction of interfacial impedance. Surface roughness affects the wettability due to the increase in the hydrophilicity or hydrophobicity, which can enhance or weaken the electrochemical ion transport in the vicinity of electrode surface.

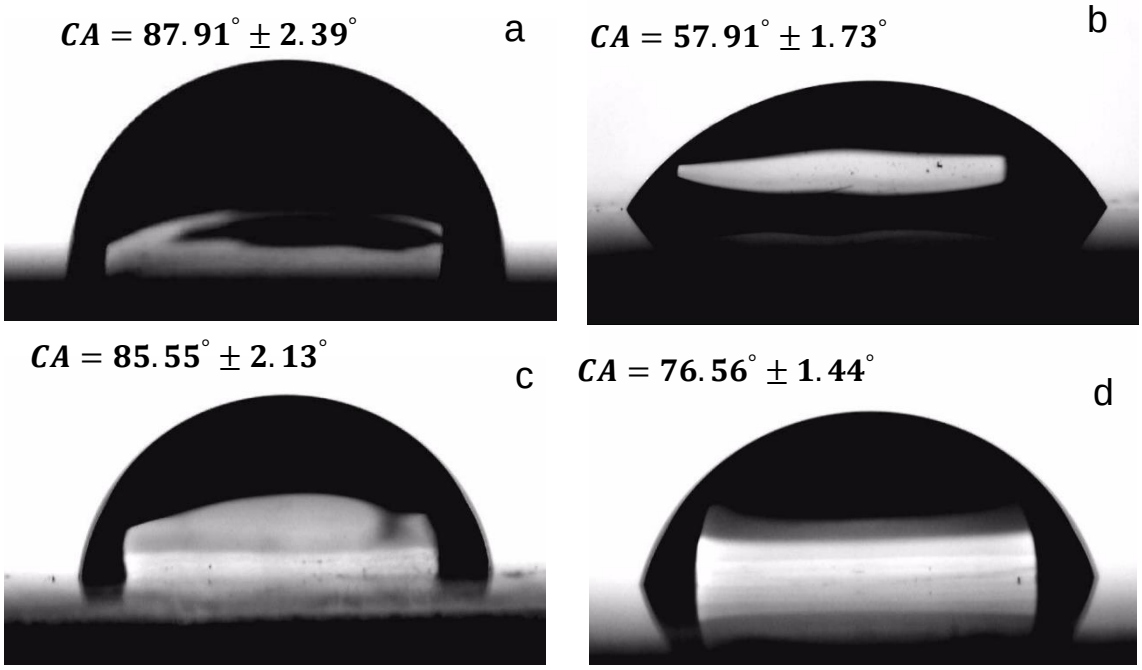

Figure. 3.6. Pictures of 6 μl water droplet on gold 4mm diameter electrodes deposited at a) -0.3V, b) -0.7 V, c) -0.9 V for an hour, and d) planar. (CA stands for contact angle.)

Rough electrode surfaces generally tend to be highly hydrophobic, leading to poor reaction kinetics between the electrolyte and the redox ion couples. Bubble pockets can shield the electrode surface, which causes a high impedance value. Therefore, the contact angle results were performed and demonstrated in Figure 3.6. The contact angle of tectorum shape GNs deposited at -0.3V for 60 mins shows quasi-hydrophilic ($CA < 90°$) behavior

with CA $87.91^{\circ} \pm 2.39^{\circ}$ (Figure 3.6a). On the other hand, fern-leaf like GNs (-0.7V, 60 mins) became relatively more hydrophilic and its contact angle was measured $57.91^{\circ} \pm 1.73^{\circ}$ (Figure 3.6b). Rounded shape GNs exhibit more hydrophobic feature ($CA = 85.55^{\circ} \pm 2.13^{\circ}$) (Figure 3.6c) compared to the planar gold electrode. The baseline planar gold surface shows a water CA of $76.56^{\circ} \pm 1.44^{\circ}$ (Figure 3.6d). Based on the CA measurement results, the most hydrophilic electrode surface is obtained with the electrode deposited with fern leaf like dendritic GNs, and therefore, interfacial impedance was obtained lower than the other electrodes deposited at different conditions.

3.2.6. The Effect of Electrode Size on Impedance Spectra

Six different electrode diameters, which are 100 μm, 200 μm, 500 μm, 1000 μm, 2000 μm, and 4000 μm, and their deposited versions deposited at -0.7 V for 60 min were tested to investigate the influence of electrode size and surface morphology on the EP effect. First, impedance measurements were performed from 100 Hz to 10 MHz at 70 µm channel height with PBS. All impedance measurements were repeated at least three times and the averaged impedance and phase angle spectra were reported. The normalized standard deviation in all cases is less than 1%. Figure 3.7a and 3.7b show the impedance magnitude and phase angle spectra of the GP electrodes.

They exhibit the systematic overall increase in impedance with decreasing the electrode size. This can be explained by the fact that both the electrolyte resistance and the interfacial impedance are inversely proportional to the surface area of the electrode.

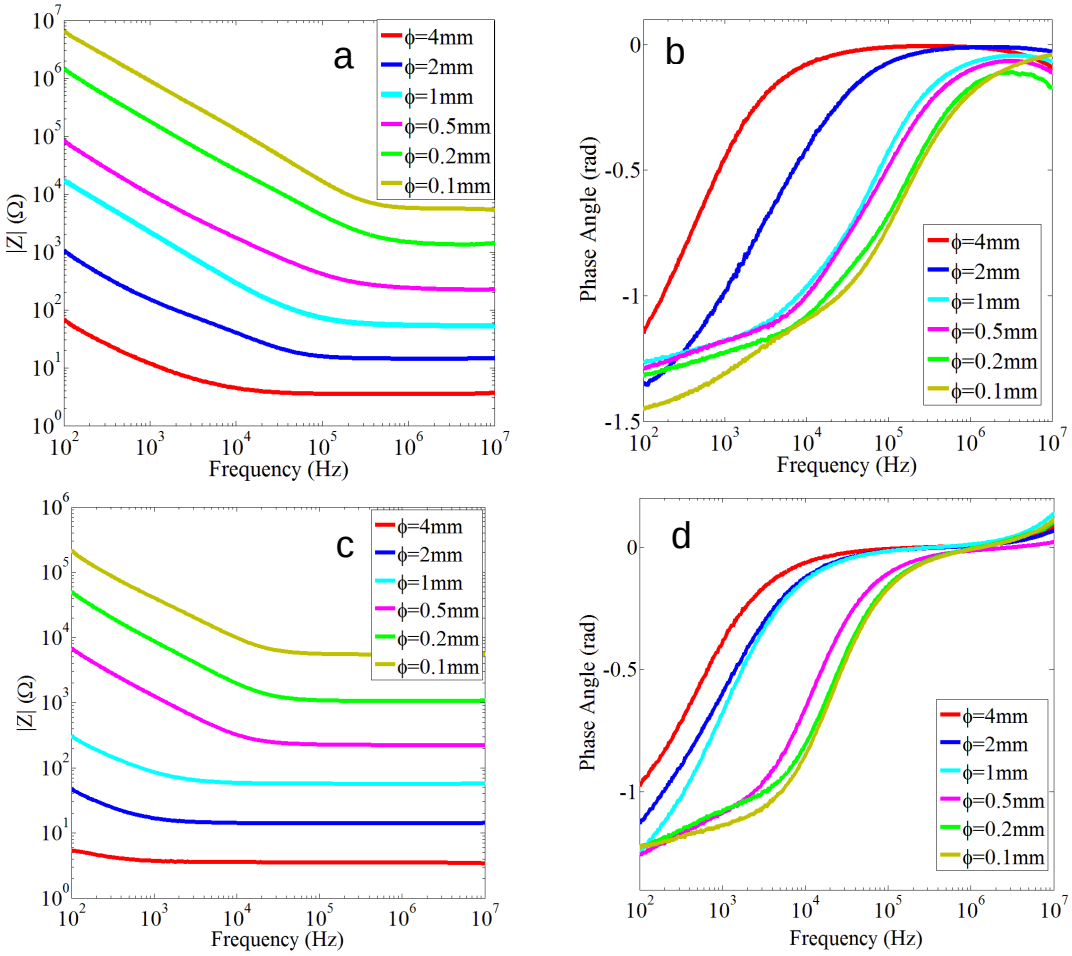

Figure 3.7. Impedance magnitude and phase angle spectrum of GP (a, b) and GNs (c, d) electrodes with diameters varying from 0.1mm to 4mm.

EP overshadowed the impedance data in the low frequency spectrum and this behavior shifted towards higher frequencies with decreasing the electrode size, limiting the useful frequency range for small electrodes [52, 187]. The impedance was dominated by R_{sol} at higher frequencies. For parallel plate electrodes, the magnitude of solution resistance can be analytically calculated with, $R_{sol} = \frac{L}{\sigma_b A}$, where L is the channel height, σ_b is the solution bulk conductivity, and A is the geometric area of the electrode. R_{sol} was not altered after

GNs deposition, since the electrolyte solution resistance is expected to be dependent on the geometrical electrode area and not on the effective surface area. Therefore, identical sized electrodes converged to almost the same impedance value at the high frequency spectrum. The highest error between the experimental and analytical values was $\sim 7\%$ for $100\mu m$ diameter electrode. This small discrepancy can be related to the outgrowth of nanostructures in the peripheral direction which changes the diameter of the electrode. The results show that electrodes coated with GNs minimized the effect of EP and expanded the usable frequency bandwidth (Figure. 3.7c). This can be easily distinguished using Figure. 3.7d, where a clear shift of the phase angle towards less negative values was observed after deposition of GNs. A wide and flat phase angle region with values approaching zero is attained with electrodes coated with GNs. The inductance effect became more important at high frequency region for coated electrode, and hence, phase angle yielded positive values.

The normalized $K\ and\ \alpha$ values (K^* and α^*) for different diameter GP and GNs electrodes are shown in Figure 3.8. The mean and standard deviation on K and α parameters were calculated with consecutive measurements and uncertainty analysis was explained in our previous study [46]. The K and α values are normalized with the $K_{100\mu m} = (2.24 \pm 0.04) \times 10^{-8}$ and $\alpha_{100\mu m} = 0.862 \pm 0.006$ of the 100µm diameter electrode. According to the results, the magnitude of K^* increases with increasing the electrode geometric area and α^* decreases, which is consistent with the CPE theory. After the surface of electrode is enlarged with GNs, the K^* value drastically increases as compared to their planar value. The α^* values decreases, and hence, the characteristic of interfacial impedance becomes more resistive. The increase in K^* and the decrease in α^* for modified

electrodes are found to be greater for the largest GNs modified electrodes. The reason for this difference can be explained with the increased volume of GNs on the planar electrode. Both electrode size and number of GNs clusters on the surface increases with increased electrode diameter, and hence, the amount of increase in K and decrease in α are greater for the GNs coated 4mm diameter electrode.

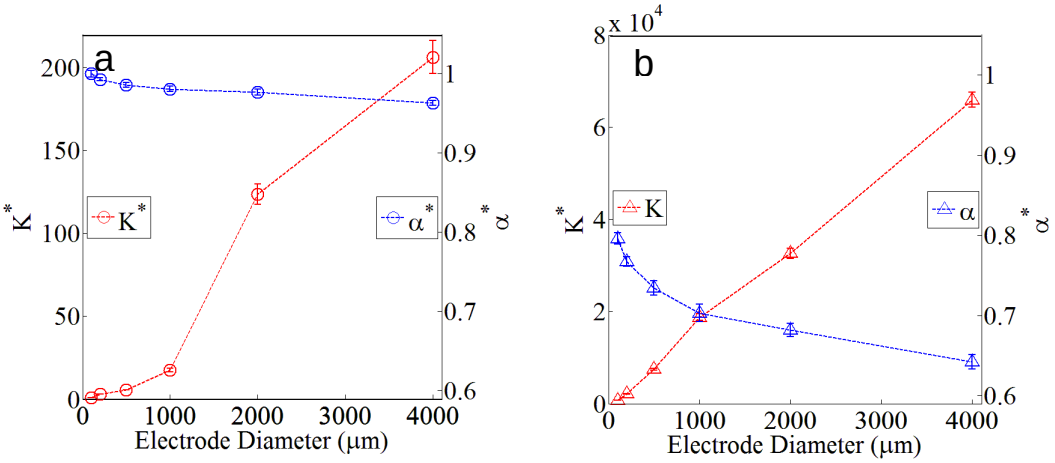

Figure 3.8. Normalized CPE parameters (K^* and α^*) of a) GP and b) GNs electrodes with different diameters. The CPE parameters are normalized with $K_{100\mu m} = 2.24 \pm 0.05 \times 10^{-8}$ and $\alpha_{100\mu m} = 0.862 \pm 0.006$ obtained for 100μm diameter electrode.

3.2.7. Device Performance Test using Dielectric Spectroscopy

In order to assess the dielectric spectroscopy response, the impedance spectra of Jurkat cells are analytically generated for planar and rough surfaces using previously published cell data [13, 188]. The Jurkat cells are modeled using the double shell model, which depicts the cells as perfectly spherical particles surrounded by cell membrane that contain the cytoplasm and a spherical nucleus separated by a nuclear envelope.

Total impedance (Z) is a linear combination of the EP impedance (Z_{ep}) and the cell suspension impedance (Z_{sus}),

$$Z = Z_{sus} + Z_{ep} \tag{3.1}$$

Z_{ep} is modelled as CPE,

$$Z_{ep} = \frac{1}{K(i\omega)^{\alpha}} \tag{3.2}$$

where K and α are the CPE coefficient and exponent, respectively.

The Maxwell-Wagner mixture model for spherical particles is expressed as follows:

$$\varepsilon^*_{sus} = \varepsilon^*_{med}\frac{1 + 2\varphi f_{CM}}{1 - \varphi f_{CM}} \tag{3.3}$$

where med and sus stands for medium and suspension, respectively, φ is cell volume fraction, and f_{CM} is the Clausius-Mossotti (CM) factor given by the following relation:

$$f_{CM} = \frac{\varepsilon^*_{cell} - \varepsilon^*_{med}}{\varepsilon^*_{cell} + 2\varepsilon^*_{med}} \tag{3.4}$$

The complex permittivity of cell (ε^*_{cell}) is calculated using double shell model expressed as:

$$\varepsilon^*_{cell} = \varepsilon^*_{mem}\frac{2(1-\gamma_1) + (1+2\gamma_1)E_1}{(2+\gamma_1) + (1-\gamma_1)E_1} \tag{3.5}$$

In the above equation mem stands for the cell membrane, and the factor γ_1 is given as, $\gamma_1 = (1 - d_{mem}/r)^3$, where d_{mem} is the cell membrane thickness. The parameter E_1 is given as:

$$E_1 = \frac{\varepsilon^*_{cyt}}{\varepsilon^*_{mem}}\frac{2(1-\gamma_2) + (1+2\gamma_2)E_2}{(2+\gamma_2) + (1-\gamma_2)E_2} \tag{3.6}$$

where cyt is for cytoplasm, $\gamma_2 = (r_i/(r - d_{mem}))^3$, and E_2 is given by

$$E_2 = \frac{\varepsilon_{ne}^*}{\varepsilon_{cyt}^*} \frac{2(1-\gamma_3)+(1+2\gamma_3)E_3}{(2+\gamma_3)+(1-\gamma_3)E_3} \tag{3.7}$$

where ne stands for nuclear envelope, $\gamma_3 = (1 - d_{ne}/r_i)^3$, $E_3 = \varepsilon_{np}^*/\varepsilon_{ne}^*$, and d_{ne} is the nuclear envelope thickness. In the equation for E_3, np stand for nucleoplasm.

Finally, the cell suspension admittance is calculated as,

$$Y_{sus} = \frac{1}{Z_{sus}} = i\omega\varepsilon_{sus}^* c_0 \tag{3.8}$$

where c_0 is the cell constant of the dielectric chamber that is calculated using the following relationship,

$$C_0 = \varepsilon_0 \frac{A}{h} \tag{3.9}$$

where A and h denote the electrode surface area and the gap distance between the electrodes, respectively. The values of parameters are given in Table 3.2 and Table 3.3.

Table 3.2. Cell and medium dielectric properties used for impedance spectrum generation [13, 188]

σ_{med}(S/m)	σ_m(S/m)	σ_{cyt}(S/m)	σ_{ne}(S/m)	σ_{np}(S/m)	ε_{med}	ε_m	ε_{cyt}	ε_{ne}	ε_{np}
1.5	3.14×10^5	0.32	0.0018	0.82	80	8.3	60	52	120

During the impedance measurement, cells exhibit a dielectric dispersion at sub-MHz frequencies, known as the β dispersion, which takes place because of the disparity between electrical properties of the cells and the extracellular medium. Figure 3.9 shows the generated impedance value and phase angle spectrum of 10% Jurkat cell suspension for 1 mm electrode diameter for both planar and rough surfaces. Based on this figure, GP electrodes that measure the impedance of Jurkat cells suspended in PBS are overwhelmed

by interfacial impedance, dominating the crucial β dispersion frequency range. On the other hand, the β dispersion can be distinguished by using GNs electrodes and hence cell parameter estimation is more accurate.

Table 3.3 Cell, electrode, and channel geometric parameters

Cell diameter (µm)	Cell membrane thickness (nm)	Nucleoplasm diameter (µm)	Nucleus envelope thickness (nm)	Electrode diameter (mm)	Channel height (µm)
5.3	7	4.24	40	1	70

An inverse model based on Maxwell-Wagner and double shell model was used to extract sub-cellular properties for both cases. The computational flow chart used for the inverse model was given in our previous study [188]. For both cases, medium, cytoplasm, and nucleoplasm permittivity values were fixed at 80, 60, and 120, respectively and medium conductivity was fixed at 1.5 S/m. A non-linear least square fitting algorithm employed in MATLAB was used to extract the membrane and nuclear envelope permittivity (ε_m and ε_{ne}), and membrane, cytoplasm, nuclear envelope, and nucleoplasm conductivity (σ_m , σ_{cyt}, σ_{ne}, σ_{np}), and CPE parameters (K and α). A random function was used to generate the initial guess for the fitting algorithm and the algorithm was repeated for 10 different initial parameters. All the data used here are the average values of the calculated cell parameters for different initial guesses.

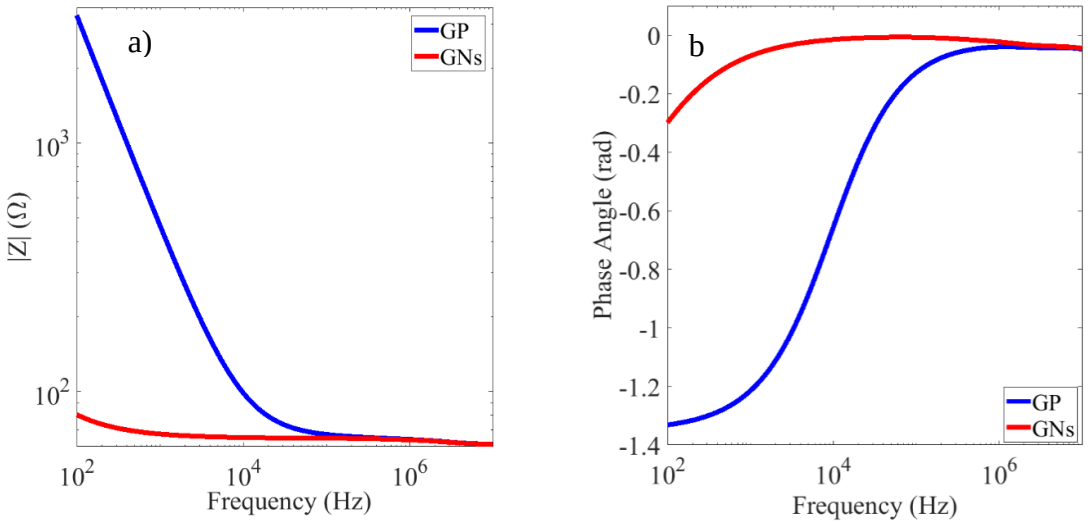

Figure 3.9. a) Impedance magnitude and b) phase angle spectrum of 10% volume fraction Jurkat cells suspended in PBS measured with 1mm diameter electrode.

The percentile error in calculating dielectric property 'a' of the cell part 'b' is defined as below:

$$E_{a_b} = \frac{\left|(a_b)_{fitted} - (a_b)_{exact}\right|}{(a_b)_{exact}} \times 100 \tag{3.10}$$

Table 3.4. shows the evaluated percentile error values in electrical properties for both cases. Based on this table, the rough electrode yielded much smaller errors in calculating the sub-cellular properties. However large errors were observed for the planar electrode.

Table 3.4. Percentile error in predicting the sub-cellular properties for 1 mm diameter flat and rough electrodes.

Electrode type	E_{σ_m}	$E_{\sigma_{cyt}}$	$E_{\sigma_{ne}}$	$E_{\sigma_{np}}$	E_{ε_m}	$E_{\varepsilon_{ne}}$	K	α
GP	1117.149	10.258	28.286	310.327	9.553	0.964	0.603	0.080
GNs	0.024	14.493	20.109	9.671	0.004	8.545	0.002	0.000

The following error metric (root mean square) is introduced to find out the overall error in the cell's properties

$$E_{rms} = \sqrt{\frac{E_{\sigma_m}^2 + E_{\sigma_{cyt}}^2 + E_{\sigma_{ne}}^2 + E_{\sigma_{np}}^2 + E_{\varepsilon_m}^2 + E_{\varepsilon_{ne}}^2 + E_K^2 + E_\alpha^2}{8}} \quad (3.11)$$

Calculations show that the root mean square error for plain surface is 410% while this value is 9.88% for the rough surface electrodes. This clearly shows that the accuracy in extracting sub-cellular properties can be dramatically increased by using rough electrodes for dielectric spectroscopy.

3.3. Conclusions

In this Chapter, the dependence of electrode/electrolyte interfacial impedance on the electrode size and surface morphology is investigated. Different morphological GNs coated electrodes were developed to minimize the interfacial impedance at the electrode/electrolyte interface using electrochemical deposition technique. The effect of deposition potential on shape of GNs was investigated at a constant deposition time. Well dispersed, uniform, tectorum shape GNs morphology was obtained at the lowest potential (-0.3V). Fern leaf type self-similar dendritic structures were obtained with high density at relatively higher applied potential (-0.7V). Density of GNs formed on the planar surface decreased above the threshold potential and the shape of GNs became rounded (-0.9V). The reason for change in the density and shape of GNs were elucidated using Nernst equilibrium theory. The exponent (α) and parameter (K) of the CPE for GNs electrodes were calculated using equivalent circuit analysis for each of the modified electrodes. The

optimum deposition potential and time were found -0.7 V and 3,600 s for decreasing the EP effect. The results were verified with surface roughness measurements and SEM analysis. The EP effect decreases with increased electrode area. Modified gold electrodes decreased the EP effect and expanded the usable frequency bandwidth. The performance of electrodes with deposited GNs compared to the GP electrodes was dramatically increased while estimating subcellular properties. In the future, we plan to investigate the methods to fabricate dendritic GNs in a more controlled way to fully understand the physics underlying the interfacial impedance for porous surfaces. We believe that this information will lead to more accurate impedance sensor designs in the future.

Chapter 4

SELF-SIMILAR INTERFACIAL IMPEDANCE OF ELECTRODES IN HIGH CONDUCTIVITY MEDIA

The occurrence of EP due to accumulation of ions at the electrode/electrolyte interface, is an inevitable phenomenon while measuring impedance spectrum in high conductivity buffers and at low frequency spectrum. Well-characterized time scales elucidating the EP effect are important for the rational design of microfluidic devices and impedance sensors. In this Chapter, interfacial impedance at the electrode/electrolyte interface is investigated considering channel height and Debye length effects on characteristic the time scaleof the EP effect in a binary electrolyte solution using parallel plate electrode configuration. Experimental results reveal self-similarity of normalized electrical impedance as a function of the normalized frequency. The experimental results also match with numerical solutions obtained by finite element simulation of the unsteady fully coupled Poisson-Nernst-Planck (PNP) equations. Furthermore, dendritic shaped gold nanostructured electrodes are examined, and it has been proven that EDL formed on porous electrode surfaces acts as a thick EDL and modifications to the characteristic time scale is necessary for porous electrodes. Finally, a CPE model is proposed to account for the self-similar impedance spectrum, which can be used for different channel heights and solution conductivities.

4.1. Materials and Methods

4.1.1. Microfabrication, Characterization and Impedance Measurement

Glass slides were cut into $2.5\ cm \times 2.5\ cm$ pieces using a diamond cutter. The glass pieces were cleaned in a 25 ℃ ultrasonic bath (FB11201, Fisher Scientific) at 37 kHz sequentially in deionized (DI) water, 1 M KOH, acetone, and isopropyl alcohol (IPA) for 10 min, followed by a rinse with DI water. Following the cleaning steps, the substrates were dried using Nitrogen gas flow. The glass slides were then placed inside an oven at 150 ℃ to fully evaporate any water residues. Fig. 1a-h show a schematic of microfluidic chip fabrication.

Firstly, a masking tape was used to generate the electrode patterns (Figure 4.1a). The masking tape was cut using a craft cutter (Silver Bullet) to obtain circular electrode patterns. After the masking tape was adhered to the glass substrate, the slides were sequentially coated with 20 nm thick chromium "seeding" layer, succeeded by a 60 nm thick gold layer using a sputter coater (EMS300TD, Emitech) (Figure 4.1b). Following the sputtering process, the masking tape was removed and electrodes were rinsed in DI water (Figure 4.1c). Copper conductive tapes (3M) were used for terminal leads. The tapes were bonded using conductive silver epoxy (MG Chemicals). In order to fabricate porous electrodes, the gold planar (GP) electrodes were immersed in a 1 mg/mL sodium tetrachloroaurate (III) ($AuCl_4Na2H_2O$; sigma Aldrich) electrolyte for electrodeposition of gold nanostructures (GNs). A three-electrode potentiostat/ galvanostat system was used for electrochemical deposition (EZstatPro, Nuvant) in potentiostatic mode (-0.7V) [46]. In this setup, electric current flows between a platinum counter electrode (MW-4130, BASI) and the working electrodes (Cu/Au sputtered electrodes), where the potential at the working electrode is controlled in reference to the Ag/AgCl electrode (MF-2052, BASI). Electrochemical deposition of gold resulted in formation of dendritic fern leaf type gold nanostructured electrodes.

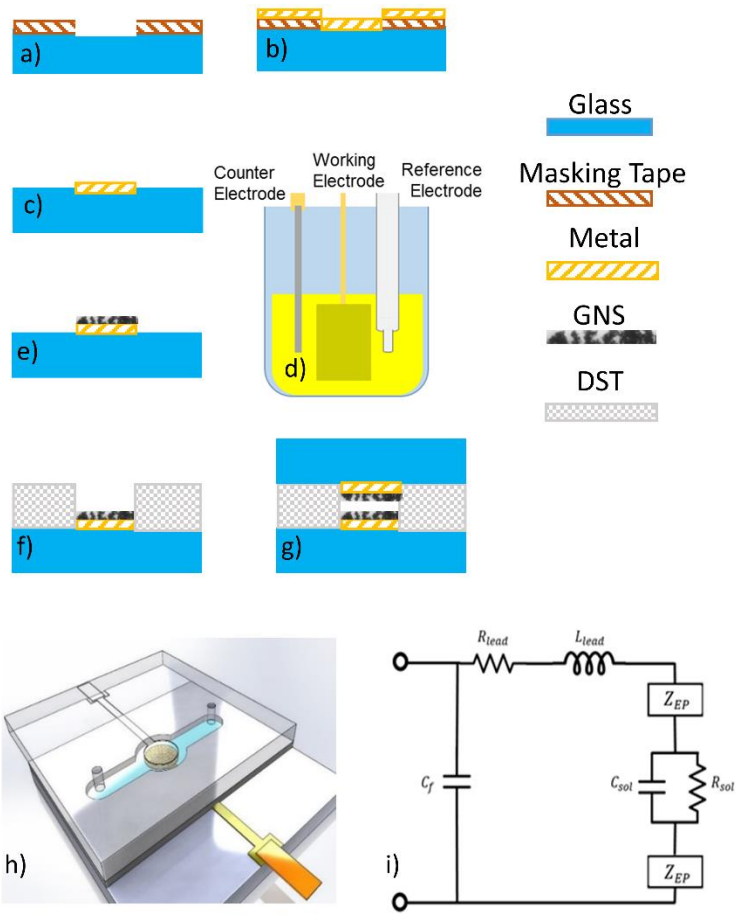

Figure 4.1. Microfluidic chip fabrication process: a) generating electrode patterns using masking tape, b) metal sputtering, c) removing masking tape, d) three electrode system configuration for electrochemical deposition, e) formation of gold nanostructures, f) microchannel fabrication using double sided tape (DST), g) aligning and assembly, h) a schematic of the assembled microfluidic device used for impedance measurements, and i) equivalent circuit model used to extract lead resistance and inductance.

The substrate was then heat treated in a convection oven at 200 ^{0}C for 30 min to increase the bonding strength of nanostructures on plain gold surfaces (Figure 4.1d-e). The microfluidic channel was fabricated using double sided tape (DST) cut with a craft cutter (Silver Bullet) and sandwiched between the two glass slides (Figure 4.1f). Inlets and outlets were drilled with a diamond drill bit on glass substrates. Two electrodes were aligned on

top of each other in the middle region of the microfluidic channel using KarlSuss MJB-3 mask aligner (Figure. 4.1g). Fig. 1h illustrates a schematic of the assembled microfluidic device.

KCl solutions with different conductivities were used in the microchannel for impedance measurements. The conductivity of the prepared solutions was measured using a conductivity meter (Con11, Oakton). For GNs electrodes, the surface morphology of electrodes was characterized with scanning electron microscopy (SEM Leo-Zeiss 1450VPSE- resolution~1 nm) operated at 25kV and varying magnification factors (12-40k). Non-contact laser profilometer (PS50, Nanovea) was used to measure the thickness of GNS electrode.

A high precision impedance analyzer (4194A, Agilent) was used to measure the impedance of different concentration of potassium chloride (KCl) solutions in 1 kHz-40 MHz frequency range. For all of the measurements, the voltage signal of the impedance analyzer was fixed at 20 mV which ensures the absence of the faradic reactions. Electrical ports of the microfluidic device were connected to the high and low terminals of the impedance analyzer through a test fixture (HP 16047A) in 4 terminal configuration. The impedance measurement was performed using an auto-balancing bridge method explained in[189]. The binary electrolyte used in this study was KCl purchased from Sigma Aldrich with varying conductivities ranging from 0.25 S/m to 1 S/m. The impedance of the device filled with the KCl solution was modeled using serial combination of Z_{EP} to model EP effect and parallel combination of (R_{sol}) and (C_{sol}) to model the electrolyte impedance. These are in series with resistance (R_{lead}) and inductance (L_{lead}) of the electrode leads. These elements are connected in parallel to a stray capacitance (C_f). The equivalent circuit model proposed

in Figure. 4.1i was used to extract the leads resistance and inductance. More information on lead resistance and inductance extraction can be found in our previously study [46]. Faradaic effects were neglected considering the magnitude of the applied voltage (0.2 V), frequency range (1kHz-40MHz), and electrode materials [180, 190, 191].

In the normal electrode-electrolyte system, impedance in 1-10MHz frequency range is purely due to solution resistance. Beyond the EP regime (Typically $f > 1\ MHz$ for high conductivity media), the impedance response would be a horizontal line. For parallel plate electrodes, the value of resistance, commonly referred to as the spreading resistance, is determined by the following equation:

$$R_{sol} = \frac{L}{\sigma_b A} \tag{4.1}$$

where L is the electrode separation distance or the bulk length scale (channel height), σ_b is the solution bulk conductivity, and A is the geometric area of the electrode. The relaxation time for charging of the double layers is known to depend on the electrode separation distance via bulk resistance, and double layer thickness. The harmonic mean of the Debye and bulk time scales ($\tau_c = \lambda L/D$) is the primary time scale for diffusive-charge dynamics, where λ is the Debye length, and D is the diffusion coefficient. For planar surface electrodes, the dimensionless frequency is expressed as $f^* = f \times \tau_c$, where f is the frequency.

4.1.2. Numerical Procedure

The computational domain is one-dimensional and contains a dilute, completely dissociated electrolyte between two parallel electrodes located at $x = 0$ and $x = L$. The

concentrations of ions inside the electrolyte (K^+ and Cl^-) are described by the Nernst-Planck equation

$$\frac{\partial c_i}{\partial t} + \boldsymbol{\nabla} \cdot \boldsymbol{J}_i = 0 \tag{4.2}$$

where c_i and $\boldsymbol{J}_i$ are the ionic concentration, and flux term of species i. The flux term consists of diffusive and electro-migration terms and is defined as

$$\boldsymbol{J_i} = -D_i \boldsymbol{\nabla} c_i - z_i u_{m,i} F c_i \boldsymbol{\nabla} \psi \tag{4.3}$$

where D_i and z_i are the diffusion coefficient and valence of i^{th} ionic component. ψ is the electric potential and $u_{m,i}$ is the mobility of species i, defined by the Nernst-Einstein relation as follows

$$u_{m,i} = \frac{D_i}{RT} \tag{4.4}$$

where R and T denote the universal gas constant and absolute temperature, respectively.

Electric field induced by electric potential and charge density distribution in the media is governed by Poisson equation

$$\boldsymbol{\nabla} \cdot \varepsilon \boldsymbol{E} = \rho_E \tag{4.5}$$

In this equation, $\boldsymbol{E}$ is the electric field ($\boldsymbol{E} = -\boldsymbol{\nabla}\psi$), ε is dielectric permittivity and ρ_E is the space charge density defined as

$$\rho_E = F \sum_i z_i c_i \tag{4.6}$$

where F is the Faraday's constant ($F = 96485\ C/mol$).

The simulation parameters and the boundary conditions for the binary electrolyte case are as follows. The operating temperature is $300\ K$ and diffusivities of K^+ and Cl^- ions are fixed at $1.7 \times 10^{-9}\ m^2/s$. The relative permittivity of medium is considered 80. The boundary at $x = L$ is grounded and the boundary at $x = 0$ is subjected to a sinusoidal electric potential

$$\psi = \psi^{AC} \sin(\omega t) \tag{4.7}$$

ψ^{AC} is the amplitude of AC electric potential ($0.02\ V$), and ω is the angular frequency ($\omega = 2\pi f$, where f is the frequency). Both boundaries at $x = 0$ and L are considered as ideally polarizable without Faradic processes, so the ionic fluxes vanish at these boundaries ($\boldsymbol{n}.\boldsymbol{J}_i = 0$).

The coupled PNP equations are solved numerically in 1D using Finite Element (FE) package, COMSOL Multiphysics 5.2. A finer mesh is introduced near the electrode boundaries to resolve transport in the thin EDL near the surface. In all cases, the initial cation and anion concentrations are set to bulk concentrations and initial potential is set to zero, such that the system is at rest when $t = 0$. From $t = 0$ onward, we use a time stepping routine in combination with direct solving method (**MU**ltifrontal **M**assively **P**arallel sparse direct **S**olver (**MUMPS**)) to compute the time dependent behavior of the system. Current density (A/m^2) at each time step is calculated using the following equation at electrodes

$$\boldsymbol{j} = F \sum_i z_i \boldsymbol{J}_i \tag{4.8}$$

Current density is then represented as a sinusoidal function with the same frequency as the AC voltage but with a phase shift which can be written as

$$\boldsymbol{j} = j\sin(\omega t - \varphi) \tag{4.9}$$

where j is the current density amplitude and φ is the phase angle. The specific impedance (Ωm^2) of the system at each frequency is then calculated by complex ratio of the voltage to the current density

$$Z = \frac{\psi}{j} = \left|\frac{\psi^{AC}}{j}\right| \angle\varphi = |Z|\angle\varphi \tag{4.10}$$

where $|Z|$ is the impedance value.

4.2.Results and Discussion

Three different KCl solutions with 114, 57, and 24 mM were prepared in order to investigate the effect of Debye length on characteristic time scale. The measured conductivity values were found as 1.0, 0.5, and 0.25 S/m, respectively. The microfluidic device with 70 μm channel height, was filled with aforementioned solutions starting with the lowest conductivity and impedance measurements were performed in 1 kHz-40 MHz frequency range. All the impedance measurements were repeated at least three times and the averaged impedance and phase angle spectra are reported. Figure. 4.2a and 2b shows the normalized standard deviation of the impedance magnitude and the phase angle for 1, 0.5, and 0.25 S/m KCl solutions in a 70 μm height channel. The normalized standard deviation in all cases is less than 1%.

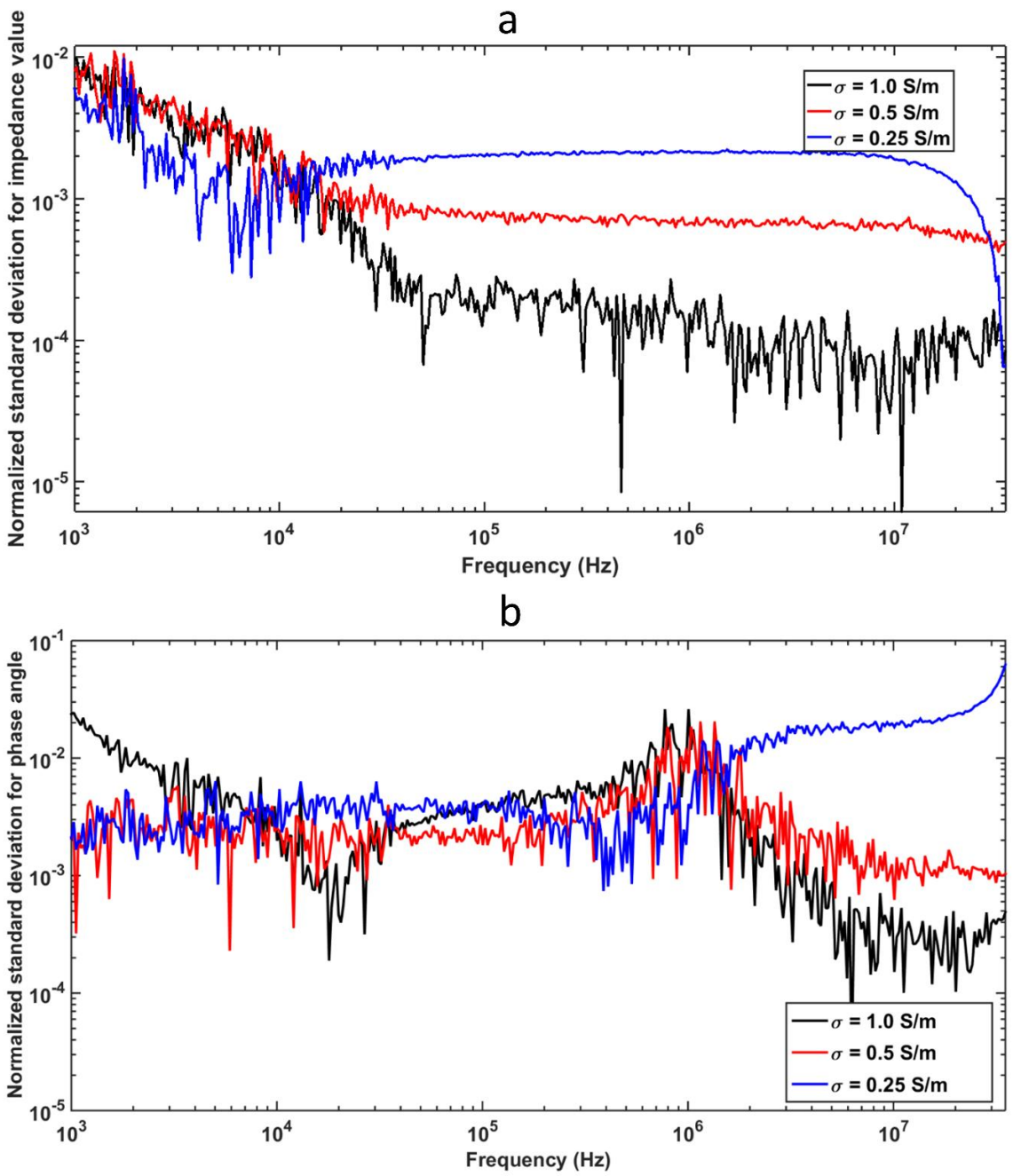

Figure 4.2. Normalized standard deviation of a) impedance magnitude, and b) phase angle for different conductivity of KCl solutions.

Figure. 4.3a and 3b show the impedance value and phase angle spectrum of the GP electrode. Frequency independent impedance response of the electrode is attributed to the solution resistance (R_{sol}) which was experimentally found around 1 MHz. The highest error between experimental and analytical value (Equation 4.1) was ~5% for the lowest conductivity medium.

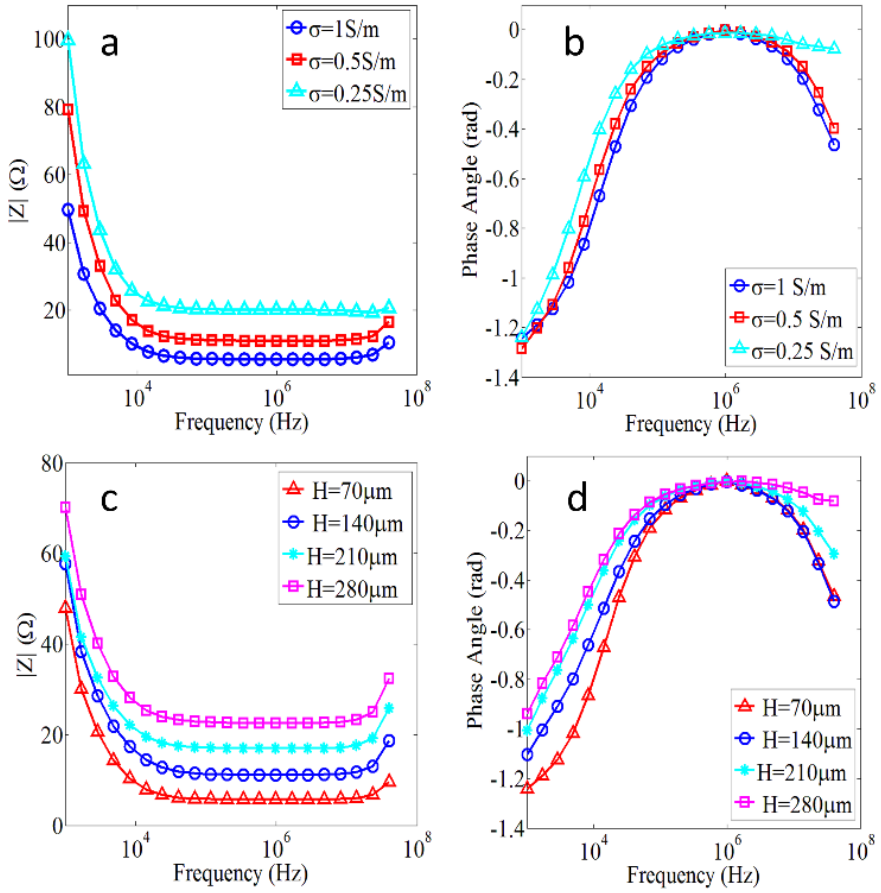

Figure 4.3 a) Experimental impedance value and b) phase angle spectrum of KCl solution having 1, 0.5, and 0.25 S/m conductivity in a 70 μm channel height. c) Experimental impedance value and d) phase angle spectrum of 1 S/m KCl solution in micro-channels having 70, 140, 210, and 280 μm height.

This small discrepancy is related to the inductive part of solution impedance, which plays a minor role at low conductivities [192]. Additionally, the phase angle at 1 MHz is near zero, which means the system is completely resistive. Therefore, the impedance value measured at 1MHz was taken as the solution resistance. Figure. 4.3a shows the systematic decrease in impedance with increasing conductivity at the high frequency range where R_{sol} dominates the impedance spectrum. This is explained by the fact that electrolyte resistance is inversely proportional to the conductivity of solution.

On the other hand, EP overshadowed the impedance data in the low frequency spectrum and this behavior shifted towards higher frequencies for increasing solution conductivity. Electrode diameter ($\phi = 4mm$) and solution concentration used for impedance measurement ($114\ mM, \sigma = 1\ S/m$) were kept constant and impedance measurements were performed at different channel heights varying from $70\ \mu m$ to $280\ \mu m$. The impedance value and phase angle spectra are shown in Figure. 4.3c and 3d. The impedance value increased in proportional to the channel height and phase angle shifted to higher values, which is consistent with theory. Impedance value increased after a certain frequency for different conductivities (Figure 4.3a) and channel heights (Figure 4.3c). This was caused by the parasitic effect of a stray capacitance in the high frequency spectrum. This effect is clearly noticed from the corresponding phase angle figures (Figure 4.3b and Figure 4.3d)[52].

Impedance values given in Figure. 4.3 were normalized with R_{sol} in order to better visualize how EP is affected by conductivity of solution and channel height at low frequency range. The charging time, τ_c, was used to make the frequency domain

dimensionless and the results are shown in Figure. 4.4a and 4.4b. Debye length (λ) was calculated using the following equation

$$\lambda = \sqrt{\frac{\varepsilon \mathrm{RT}}{\sum_{i=1}^{N} \mathrm{z_i}^2 \mathrm{F}^2 \mathrm{c_{i0}}}} \tag{4.11}$$

The Debye lengths were calculated 0.96 (λ_1), 1.27 (λ_2), and 1.97 (λ_3) nm for 114, 57, and 24 mM KCl solutions, respectively. A rescaling of Figure 4.3 as a function of dimensionless frequency (f^*) reveals a universal impedance behavior for the current measurement system. The impedance value and phase angle of each measured data were collapsed to a single line, revealing the self-similarity of normalized impedance spectra.

Time dependent numerical simulations of fully coupled PNP equations were performed in 1 kHz-1 MHz frequency range for 10 time periods and each time period was divided to 40 equal time steps. First, the numerical simulations were performed by fixing the channel height (70 μm) and changing initial ionic concentrations (114, 57, and 24 mM) representing 1, 0.5, and 0.25 S/m KCl solutions, respectively. Then the initial concentration of positive (K^+) and negative (Cl^-) ions were fixed at 114 mM which corresponds to 1 S/m KCl solution and the channel height was changed from 70 μm to 280 μm. The impedance value at each frequency was normalized with constant high frequency impedance value and the same scaling (τ_c) was used to obtain dimensionless form of the impedance results for different KCl solution conductivities and channel heights. Figure 4.4c and 4.4d show the normalized numerical impedance values and phase angles versus the dimensionless frequency (f^*) for the same conditions with the experiments. Figure 4.4c and 4.4d illustrate that all impedance and phase angle curves obtained at different channel heights and

conductivities complied with the same time scale (τ_c), and their behaviors are consistent with the experimental results.

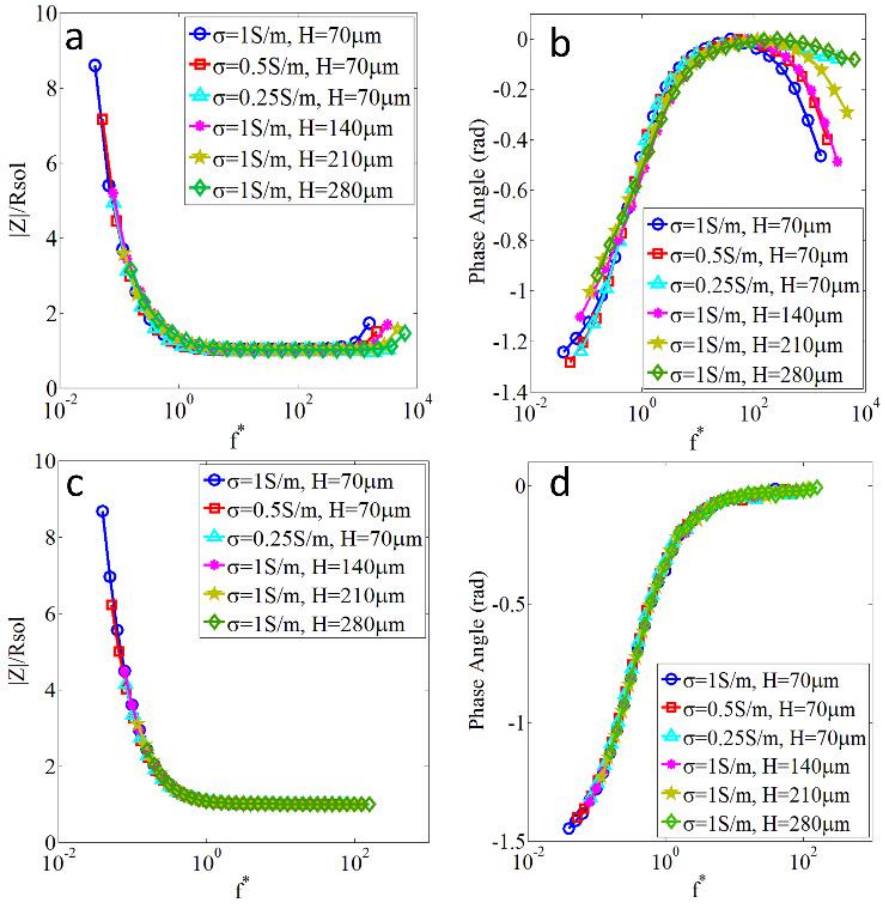

Figure 4.4. a) Normalized experimental impedance and b) phase angle spectrum as a function of the normalized frequency. c) Normalized numerical impedance and d) phase angle spectrum as a function of the normalized frequency.

Furthermore, comparing experimental and numerical results show that unsteady, 1D, fully coupled PNP equations without Faradic reactions successfully predict the electrical impedance behavior of micro-electrodes at different channel heights and solution conductivities. It also shows the power of this numerical tool for further investigation of

other aspects of micro-electrodes such as surface roughness by extending it to two or three dimensional geometries.

SEM image of GNs surface is given in Figure 4.5a. After electrochemical deposition, fern leaf type dendritic gold nanostructures were obtained with high density. Figure 4.6 represents the root mean square height of GNs electrode which is equal to 2.55 μm. Impedance measurements were repeated with GNs electrodes in a 70 μm channel height for 1, 0.5, and 0.25 S/m KCl solutions. Based on the normalized impedance spectra (Figure. 4.5b), the results show that electrodes coated with GNs decreased the EP effect and expanded the usable frequency bandwidth. Moreover, R_{sol} remains constant after GNs deposition since the electrolyte solution resistance is dependent on the geometrical electrode area not the effective surface area. Normalized Impedance spectra for different conductivities of KCl solution are given in the Figures 4.7a, 4.8a, and 4.9a. It is observed that the universal impedance behavior was altered for GNs electrode for all conductivities. Hence, transport properties must be modified to account for the effective length scales for porous electrode surface. Empirical formulations were developed by Newman to find the effective diffusion coefficient for porous electrodes [122]. However, there is no well-defined theory to predict ion transport for porous electrode surfaces. We scaled the charging time, τ_c with a constant to maintain the universal impedance behavior for different conductivity impedance measurements, and defined a new time constant τ_n for GNs electrodes as

$$\tau_n = C\tau_c \tag{4.12}$$

where C is a dimensionless coefficient, which might be a function of porosity, thickness of nanostructures, tortuosity, or combination of these parameters.

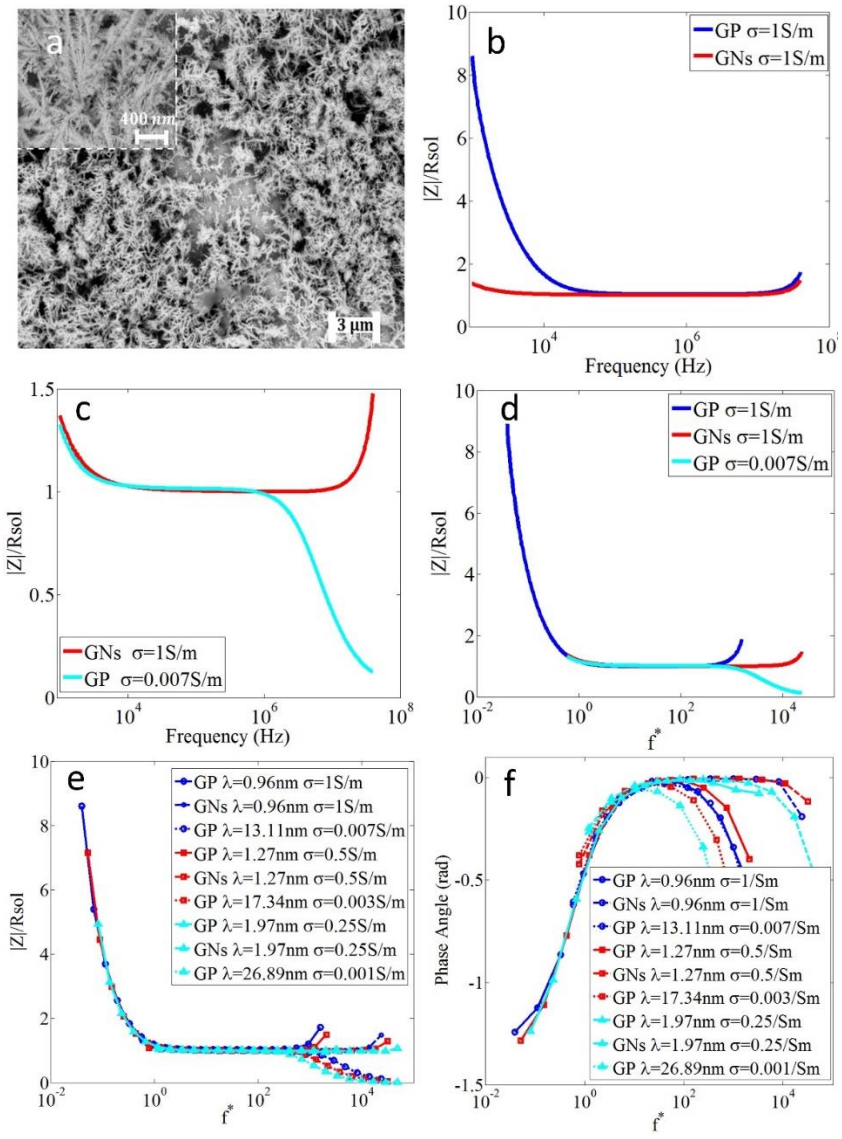

Figure 4.5. a) SEM images of GNs electrodes surface. b) Normalized impedance spectra obtained with GP and GNs electrodes with 1 S/m KCl solution. c) Normalized impedance spectra obtained with GP and GNs electrodes with 0.007 S/m and 1 S/m KCl solutions, respectively. d) The combination of Fig. 4b and Fig. 4c using normalized frequency, f^* considering thickening of double layer. e) Normalized impedance value and f) phase angle of all KCl solutions with respect to f^*.

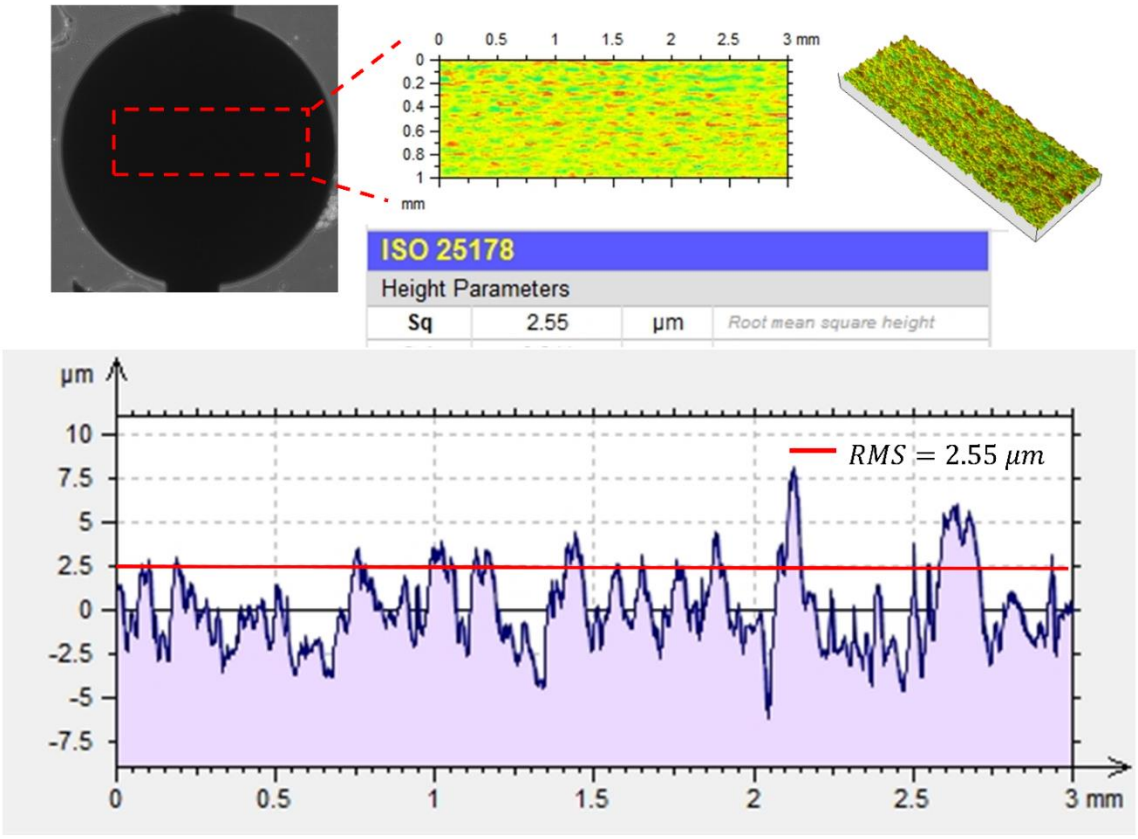

Figure 4.6. Root mean square height measurement of electrochemically deposited electrode using non-contact optical profilometry.

The new time constant τ_n can be written as a function of an effective EDL thickness λ_{eff} and effective diffusivity D_{eff}, and given as

$$\frac{\lambda_{eff} L}{D_{eff}} = C \frac{\lambda L}{D} \tag{4.13}$$

Since the channel height was kept constant for GP and GNs electrodes, equation (4.13) can be simplified and an effective Debye length can be obtained as,

$$\lambda_{eff} = C \frac{D_{eff}}{D} \lambda \tag{4.14}$$

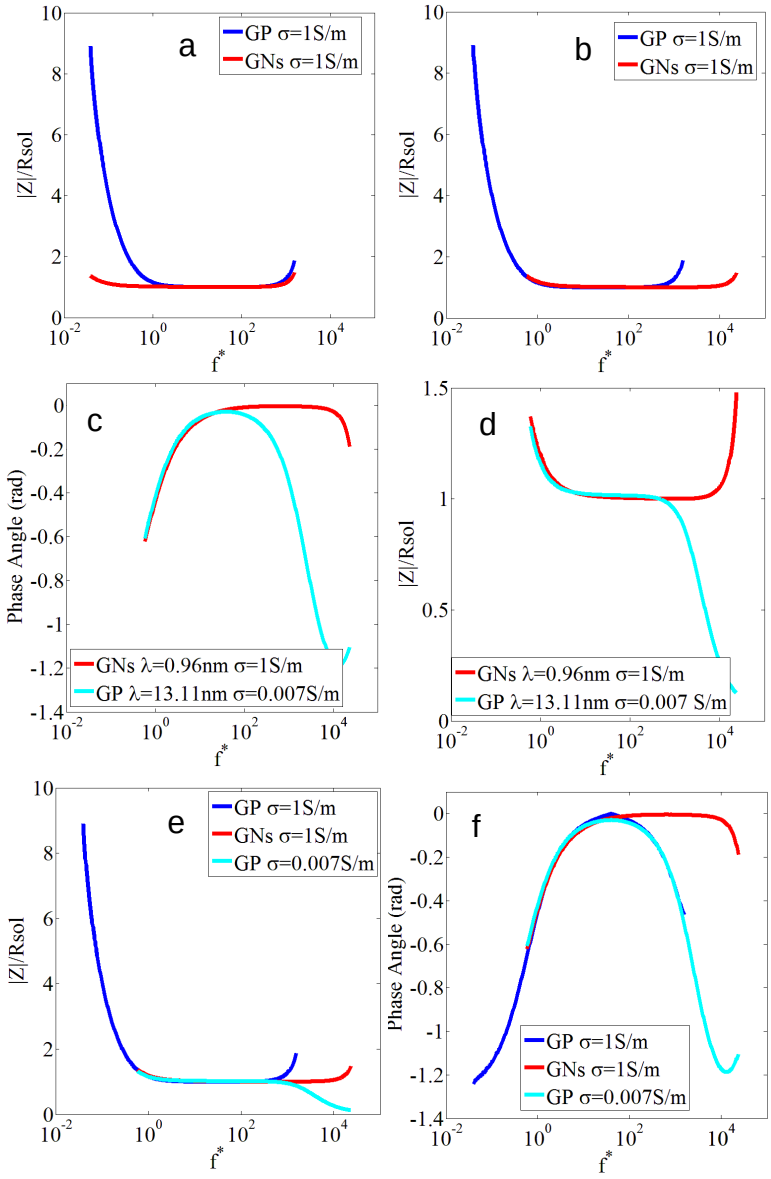

Figure. 4.7. a) Normalized impedance spectra obtained with GP and GNs electrodes with 1 S/m KCl solution. b) Normalized impedance spectra obtained with GNs scaled with coefficient C. c) Normalized impedance spectra obtained with GP and GNs electrodes with 0.007 S/m and 1 S/m KCl solutions, respectively. d) The combination of Figure b and c using normalized frequency, f^* considering thickening of double layer. e) Normalized impedance value and f) phase angle of all KCl solutions with respect to f^*.

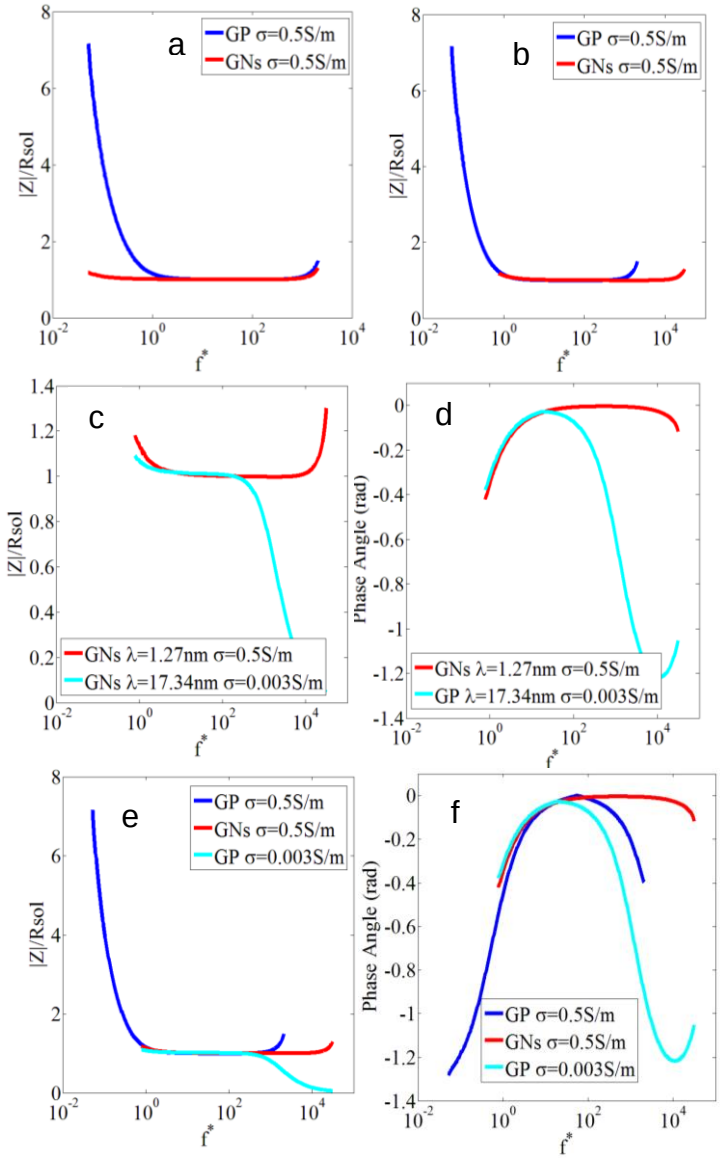

Figure. 4.8 a) Normalized impedance spectra obtained with GP and GNs electrodes with 0.5 S/m KCl solution. b) Normalized impedance spectra obtained with GNs scaled with coefficient C. c) Normalized impedance spectra obtained with GP and GNs electrodes with 0.0035 S/m and 0.5 S/m KCl solutions, respectively. d) The combination of Figure b and c using normalized frequency, f^* considering thickening of double layer. e) Normalized impedance value and f) phase angle of all KCl solutions with respect to f^*.

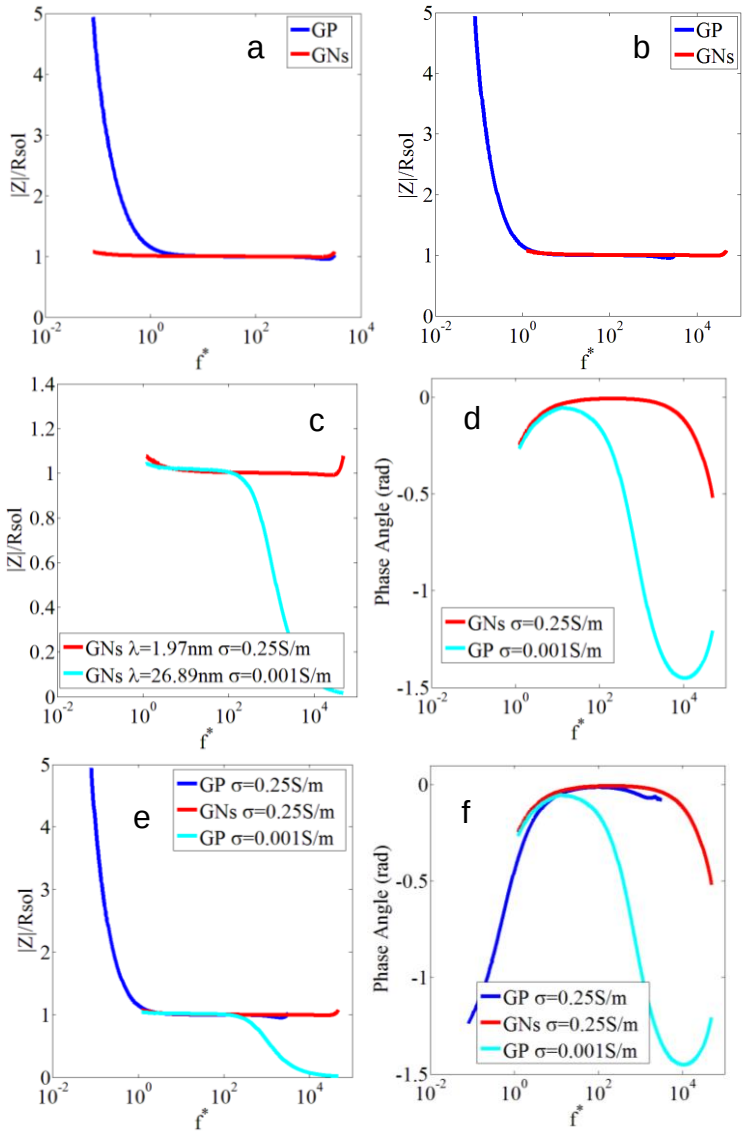

Figure. 4.9. a) Normalized impedance spectra obtained with GP and GNs electrodes with 0.25 S/m KCl solution. c) Normalized impedance spectra obtained with GP and GNs electrodes with 0.001 S/m and 0.25 S/m KCl solutions, respectively. d) The combination of Figure b and c using normalized frequency, f^* considering thickening of double layer. e) Normalized impedance value and f) phase angle of all KCl solutions with respect to f^*.

According to Bruggeman's empirical relation, $\frac{D_{eff}}{D} = \epsilon^{0.5}$, where ϵ is the porosity; and this relation is widely used in porous electrode models [121, 193]. Therefore, λ_{eff} can be rewritten as:

$$\lambda_{eff} = C\epsilon^{0.5}\lambda, \tag{4.15}$$

which shows alteration of the Debye length for GNs electrodes.

Impedance spectra obtained with GNs electrode were scaled for all conductivities with a single coefficient C to maintain the universal impedance behavior. All the curves were collapsed to the universal line by multiplying f^* by 15 ($C = 15$) (Figure 4.7b, 4.8b, and 4.9b). Image analysis was performed to find the porosity of GNs electrode using ImageJ [194] software. The procedure for image analysis was extensively explained in our previous study [195]. The porosity is found to be 0.81 based on the SEM images given in Figure 4.5a. The effective Debye lengths for GNs electrode obtained for 114, 57, and 24 mM KCl solutions were calculated from equation (4.15) and they were found to be 13.11 (λ_{eff1}), 17.34 (λ_{eff2}) and 26.89 (λ_{eff3}) nm, respectively.

Using these effective Debye lengths, concentrations of corresponding KCl solutions were calculated from equation (4.11) in order to prove the thickening of double layer on porous electrodes. The concentrations of solutions for 13.11 (λ_{eff1}), 17.34. 05 (λ_{eff2}) and 26.89 (λ_{eff3}) nm are found to be $c_1 = 0.5\,mM$ $\left(\sigma_1 = 0.007\,\frac{S}{m}\right)$, $c_2 = 0.3\,mM$ ($\sigma_2 = 0.003\,S/m$), and $c_3 = 0.1\,mM$ ($\sigma_3 = 0.001\,S/m$), respectively. Based on these concentrations, KCl solutions were prepared to perform impedance measurements with GP electrodes. Figure 4.5c shows normalized impedance spectra obtained with 114 mM KCl solution for GNs and 0.5 mM KCl solution for GP electrode. Normalized

impedance spectra and phase angles for other KCl solutions are given in the Figure 4.7c – 4.7d, Figure 4.8c-4.8d, and Figure 4.9c-4.9d. The results showed similar behavior between GP and GNs electrodes and the highest error in the dimensionless impedance values were 3.20% , 7.6%, and 3.25% for $1, 0.5,$ and $0.25\ S/m$ in 1 kHz-1 MHz frequency range, respectively. Figure 4.5d shows the normalized impedance value with respect to normalized frequency for GP and GNs electrodes considering the thickening of double layer for porous electrodes based on equation (15). Figure 4.5e and 4.5f represents the impedance spectra of all KCl solutions. The figures for each specific conductivity are shown in Figure 4.7e-4.7f, 4.8e-4.8f, and 4.9e-4.9f. These figures show all dimensionless impedance and phase angle spectrum acquired with GP and GNs electrodes, which collapsed in to a single line. According to the results, the double layer formed on porous electrode surface acts as a thick double layer, and the universal impedance behavior was achieved after scaling the dimensionless frequency with a constant C that is specific to the GNs electrode properties.

A CPE model in series with solution resistance was used to model this self-similar behavior at low RF spectrum [196]. The normalized total impedance of electrode/electrolyte interface and solution resistance is given as

$$Z^* = 1 + Z^*_{CPE} = 1 + \frac{1}{K(i\omega^*)^\alpha} \tag{4.16}$$

where K and α are CPE coefficient and exponent, respectively, ω^* is the normalized angular frequency ($2\pi f^*$), and i is $\sqrt{-1}$. The parameter α changes from zero to one ($0 \leq \alpha \leq 1$), corresponding to purely resistive ($\alpha = 0$) and purely capacitive ($\alpha = 1$) EDL in the two limits [197]. For the fitting procedure, non-linear least square algorithm was

employed in MATLAB to find the best K and α that yields the least difference between the real and imaginary parts of the model and experimental data[42].

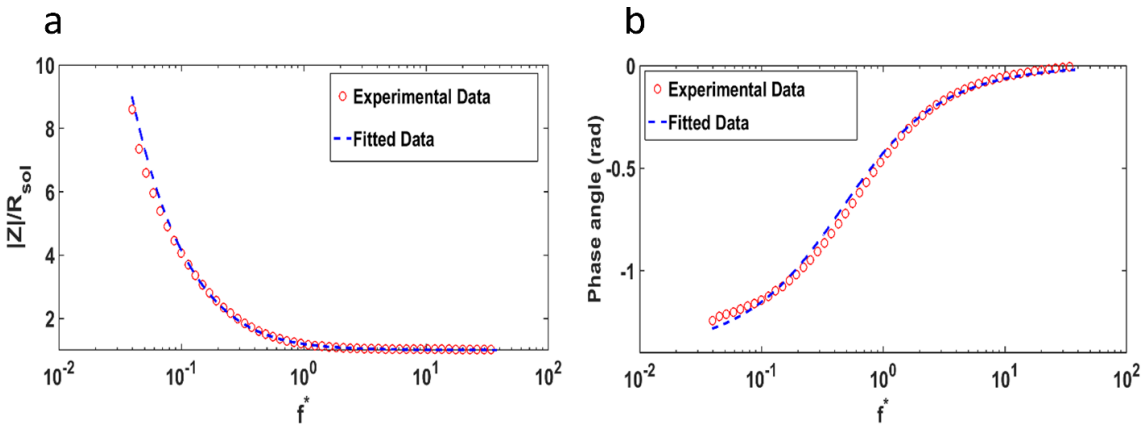

Figure 4.10. normalized impedance value (a) and phase angle (b) versus normalized frequency for the model and experimental data.

Since all the impedance spectra collapse to the same line, the highest conductivity spectrum was selected as the self-similar experimental result. For presentation purposes, only one experimental data point out of ten discrete frequency values is shown in the Figure 4.10, while the fitting is performed using all measured frequency values. Based on the fitting results, the following equation can be used for all channel heights and solution conductivities in the case of planar and porous electrodes by having the information of electrode geometry and double layer thickness.

$$Z^* = 1 + \frac{2.551}{(i\omega^*)^{0.886}} \tag{17}$$

Figure 4.10 shows the normalized impedance value and phase angle versus nondimensionalized frequency for the model and experimental data. This figure clearly

illustrates that the proposed model follows both normalized impedance value and phase angle variations in the nondimensionalized frequency spectrum.

4.3.Conclusions

In this Chapter, characteristic time scales of EP effect for planar and porous electrodes are explained. In order to measure the electrical impedance at the electrode/electrolyte interface, a microfluidic device with 4 mm circular parallel plate electrodes was used. Impendence spectra for different solution conductivities and micro-channel heights were experimentally measured and it was shown that the charging time constant (harmonic mean of the Debye and bulk time scales) is the primary time scale of EP behavior. Furthermore, unsteady one-dimensional finite element simulation of Poisson-Nernst-Planck (PNP) equations were performed and same behavior as the experimental results was shown. Electrochemical deposition technique was used to deposit gold nanostructures on planar electrodes. The results revealed that GNs electrodes decreased the EP effect and expanded the usable frequency bandwidth. Normalizing impedance results of porous electrodes proved that characteristic time scale is increased by the same factor for all solution conductivities. We hypothesized that this increase is basically due to the thickening of the double layer. Further impedance measurements with GP electrodes using solutions with the same effective Debye length as the porous electrodes showed the similar universal behavior confirming our double layer thickening hypothesis. According to the results of this study, the self-similar impedance and phase angle spectra can be made dimensional to interpret the electrode behavior at various electrode separations and medium

conductivities. Therefore, one can identify the limitations of design and predict the system behavior for both planar and porous surface electrodes prior to fabrication and experimentation. A well characterized, fully understood interfacial impedance will lead to the design of optimized electrode systems. In the future, we plan to fabricate well-ordered nanostructures with different size and porosity to identify the dimensionless coefficient (C) used in equation 12. We will also focus on developing analytical and numerical methods to verify the double layer thickening hypothesis.

Chapter 5

UNIVERSAL RESPONSE OF ELECTRODE POLARIZATION IN PARALLEL PLATE CAPACITOR SYSTEMS

Classical electrochemistry problem of polarization of an electrode immersed in a symmetric binary electrolyte and subjected to a small external AC voltage is revisited. The Nernst–Planck equations are simplified to the Debye-Falkenhagen (DF) equation, which is solved together with the Poisson equation, leading to analytical formulas for the space charge density and impedance of the system for two parallel plate electrodes. We then define a limit of a thin electrical double layer and illustrate the emergence of the characteristic time scale, $\tau_c = \lambda_D L/D$, a function of the Debye length, λ_D, the electrode separation distance, L, and the ionic diffusion coefficient D. Normalizing the impedance magnitude with the solution resistance, and making the frequency dimensionless with the τ_c, we show that all analytical, numerical, and experimental data for different solution conductivities and electrode separation distances collapse onto a universal curve. To account for the Stern layer effects, we conducted numerical simulations based on the modified Poisson-Nernst-Planck model and showed that the results agree with our analytical solution for a range of concentrations, with small discrepancies observed only above 0.1 M. Based on the proposed model, experimental impedance spectroscopy results at AC potentials can be used to obtain detailed knowledge of the corresponding surface (and space) charge densities on the electrodes.

5.1. Materials and Methods

5.1.1. Setup

For the analytical model, we focus on blocking electrodes because it complies with a common experimental realization of electrodes. We consider a parallel plate capacitor containing a dilute, completely dissociated 1:1 electrolyte at constant temperature. In this configuration, two parallel flat electrodes are located at $x = 0$ and $x = L$ as shown in Figure 5.1a. The electrodes are assumed to extend to infinity to facilitate a description in which physical quantities depend only on the coordinate x, perpendicular to the electrode surface. The electrolyte is treated as a homogenous dielectric material of constant permittivity thus ignoring the possibly complex dependence on local ionic concentration near surfaces or when subjected to external fields [198]. If the charge content is high in the electrolyte, the effect of the finite size of ions has to be taken into account. This is usually accomplished by introducing the Stern layer [163]. Since our consideration is restricted to small applied voltages and relatively low concentration of solution, the Stern layer is not included in our analytical solution. However, the validity of this assumption was tested by numerically solving the Modified PNP (MPNP) equations.

Microfluidic device fabrication and experimental procedure for measuring the impedance spectra of electrolyte between parallel disk electrodes were explained in Chapter 3 and 4 [199]. Briefly, 4mm diameter disk shape gold electrodes were fabricated using standard photolithography technique. The microfluidic channel was fabricated using double sided tape and sandwiched between the two glass slides where the gold electrodes are sputtered. Inlets and outlets were drilled very close to the disk electrodes which were aligned on top

of each other (Figure 5.1b) and this meets the 1D analytical condition. Potassium chloride (KCl) solutions with varying conductivities and different microchannel heights were used for impedance measurements. Then, the microfluidic device is connected to the impedance analyzer (HP Agilent 4194A) to record the impedance spectrum. Each impedance measurement proceeds for 401 discrete logarithmically spaced frequencies from 1kHz to 40 MHz.

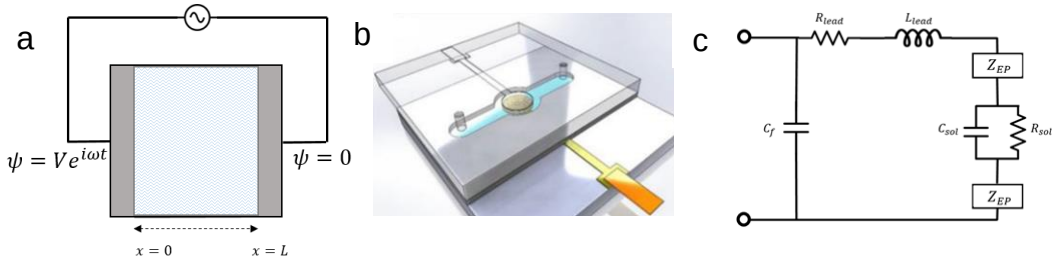

Figure 5.1. a) Sketch of the parallel plate capacitor. AC potential is applied to two parallel plate blocking electrodes, separated by distance L, and between the electrodes is filled with dilute, totally dissociated 1:1 electrolyte. b) Schematic of the microfluidic device used for impedance measurements. c) Equivalent circuit model.

The equivalent circuit model is often used to extract the electrical characteristics of microfluidic chip (Figure 1c). The equivalent circuit model consists of serial combination of interfacial ($Z_{EP} = R_{EP} + 1/i\omega C_{EP}$) and solution impedances ($C_{sol}\ and\ R_{sol}$), respectively. These elements are in series with electrode lead resistance (R_{lead}) and inductance (L_{lead}). Finally, a parallel capacitance is added to account for stray (parasitic) (C_f) effects. For highly a conductive medium, the resistance (R_{EP}) and capacitance (C_{sol}) parts of the interfacial and solution impedance can be neglected, respectively. Therefore, the microfluidic domain was modeled by EDL capacitance (C_{EP}) and solution resistance

(R_{sol}). The extraction of stray capacitance, resistance and inductance of the lead using equivalent circuit analysis was explained in our previous article [46]. After eliminating those components, the impedance data can be represented by an RC circuit. While the parameters of the RC circuit are often estimated based on the experimental data, we take a different approach here by developing a detailed mathematical model of the physical processes taking place at the electrode-electrolyte interface and in the liquid electrolyte and then use that model to calculate the impedance without the need for any adjustable parameters.

5.2. Theory

5.2.1. Solution of PNP Equations in Linear Regime

In the absence of species generation and ionic drift velocities, ionic transport is described by the Nernst-Planck equation given by

$$\frac{\partial c_i}{\partial t} + \boldsymbol{\nabla} \cdot \boldsymbol{J_i} = 0 \tag{5.1}$$

where c_i and $\boldsymbol{J_i}$ are the ionic concentration and ionic flux, respectively, for ionic species i. The flux can be expressed as

$$\boldsymbol{J_i} = -D_i \boldsymbol{\nabla} c_i - \frac{z_i D_i F c_i}{RT} \boldsymbol{\nabla} \psi \tag{5.2}$$

where D_i and z_i are the diffusion coefficient and valence of i^{th} ionic component. ψ is the electric potential and F is Faraday's constant ($F = 96485\ C/mol$). R and T denote the universal gas constant and absolute temperature, respectively. Electric field induced by the

applied electric potential and charge density distribution in the media is governed by the *Poisson* equation,

$$\boldsymbol{\nabla} \cdot \varepsilon \boldsymbol{E} = \rho_E \tag{5.3}$$

In this equation, $\boldsymbol{E}$ is the electric field ($\boldsymbol{E} = -\boldsymbol{\nabla}\psi$), ε is dielectric permittivity and ρ_E is the space charge density defined as

$$\rho_E = F \sum_i z_i c_i \tag{5.4}$$

We consider a symmetric electrolyte with two types of ions, e.g. K^+ and Cl^- ($z_+ = -z_- = z$) and having the same diffusion coefficients ($D_+ = D_- = D$). We also assume D to be independent of the local ionic concentrations. The system is assumed to be homogenous in the beginning, and hence, the initial ion concentration does not depend on the spatial coordinate.

We investigate a completely dissociated electrolyte placed between infinite flat electrodes. Therefore, the system is described by a simple one-dimensional (1D) geometry. In the linear regime, the Nernst-Planck equations transform to a 1D Debye-Falkenhagen (DF) equation, which governs the diffuse double layer (with relatively weak electric field region compared to compact layer) dynamics,

$$\frac{\partial \rho_E}{\partial t} = D\left(\frac{\partial^2 \rho_E}{\partial x^2} - \kappa^2 \rho_E\right) \tag{5.5}$$

Here κ is the inverse of the Debye length (λ_D) defined by

$$\kappa = \frac{1}{\lambda_D} = \sqrt{\frac{2z^2 e^2 N_A c}{\varepsilon RT}} \tag{5.6}$$

where e is the electron charge and N_A is the Avogadro number. A significant role is played by the boundary conditions. The electrode located at $x = 0$ is stimulated with $\psi = Ve^{i\omega t}$ and the one located at $x = L$ is grounded ($\psi(L) = 0$). The ionic flux, $J_i = -D\frac{\partial \rho_E}{\partial x} - \kappa^2 D\varepsilon\frac{\partial \psi}{\partial x}$, is assumed zero on the electrodes' surfaces ($J_i = 0\ at\ x = 0\ and\ x = L$).

Given the linear nature of the equations and the sinusoidal time forcing through applied voltage, the space charge density and electrical potential are expressed as $\rho_E = \hat{\rho}_E e^{i\omega t}$ and $\psi = \hat{\psi}e^{i\omega t}$. As a result, the DF equation and the Poisson equation are modified to the following formulas,

$$\frac{d^2\hat{\rho}_E}{dx^2} = \left(\kappa^2 + \frac{i\omega}{D}\right)\hat{\rho}_E \tag{5.7a}$$

$$-\varepsilon\frac{d^2\hat{\psi}}{dx^2} = \hat{\rho}_E \tag{5.7b}$$

where is ω angular frequency ($\omega = 2\pi f$). It is convenient to introduce nondimensional variables

$$\bar{x} = \frac{x}{\lambda_D}, \qquad \bar{L} = \frac{L}{\lambda_D}, \qquad \bar{\psi} = \frac{\hat{\psi}}{V}, \quad \bar{\rho} = \frac{\hat{\rho}_E}{\rho_{DC}} \tag{5.8}$$

Here the charge density is scaled by its value found for the DC response,

$$\rho_{DC} = -\frac{1}{2}\varepsilon V\frac{1}{\lambda_D^2} \tag{5.9}$$

The governing equations then take the form

$$\frac{d^2\bar{\rho}}{dx^2} = (1 + 2i\Omega)\bar{\rho} \tag{5.10a}$$

$$\frac{d^2\bar{\psi}}{d\bar{x}^2} = \frac{1}{2}\bar{\rho} \tag{5.10b}$$

where $\Omega = \omega{\lambda_D}^2/2D$. These equations are solved with the prescribed values of the scaled potential and zero ionic flux at the two electrodes, leading to four boundary conditions. The solution procedure and resulting formulas for the space charge density and electric potential are discussed in detail in Appendix A. Let us focus on two key quantities here, the charge density amplitude ($\bar{\rho}_0$) near the electrode surface ($x = 0$) and the electrical impedance (Z). Based on the results from Appendix A, these quantities are given in dimensionless forms by

$$\bar{\rho}_0 = \frac{1 + 2i\Omega}{1 + i\Omega\bar{L}(\alpha + i\beta)\coth\left[(\alpha + i\beta)\frac{\bar{L}}{2}\right]} \tag{5.11}$$

$$Z = \frac{1 - \frac{i}{\Omega\bar{L}}(\alpha + i\beta)^{-1}\tanh\left[(\alpha + i\beta)\frac{\bar{L}}{2}\right]}{1 + 2i\Omega} \tag{5.12}$$

Considering the limit of small Ω ($\Omega \ll 1$), the expression for charge density simplifies to

$$\bar{\rho}_0 = 1 + i\Omega\left(2 - \bar{L}\coth\frac{\bar{L}}{2}\right) \tag{5.13}$$

which is consistent with the well-known formula of Bazant et al [110]. In the vast majority of experimental studies, the Debye length is much smaller than the key length scales in the geometry of the problem, so we consider the limit of large $\bar{L}$ ($\bar{L} \gg 1$) to further simplify the results to

$$\bar{\rho}_0 = 1 - i\Omega\bar{L}, \qquad Z = 1 - \frac{i}{\Omega\bar{L}} \tag{5.14}$$

The remarkably simple formula for the impedance from Eq. (5.14) is found to be in excellent agreement with the experimental data, as discussed in more detail below. However, it is important to note that in contrast to our general expressions (5.11)-(5.12), the formulas (5.13)-(5.14) are limited by the assumption of small Ω and thus may not be applicable at high frequencies. For example, suppose the Debye length of a certain electrolyte is near 3 nm, while the diffusion constant is near $10^{-9}\ m^2 s^{-1}$. Then, for AC frequencies of 100 MHz, realized in a number of experiments, the value of Ω is near 0.5, making the predictions of the approximate formulas questionable. To further illustrate this point, we plot the results for the magnitude of the impedance in Figure 5.2 as predicted by different models. The approximate model, shown by the blue line, only matches the general expressions given by (5.14) when Ω is below 0.05. For larger values, we propose a different approximate model, based on the assumption of large $\bar{L}$ but not necessarily small Ω, resulting in

$$Z = \frac{1}{1 + 2i\Omega} \tag{5.15}$$

The result in the Figure 5.2 shows that the approximate formula matches the full expression over a range of frequencies. However, it breaks down when the frequency is small enough so that the term $\Omega\bar{L}$ can no longer be assumed large.

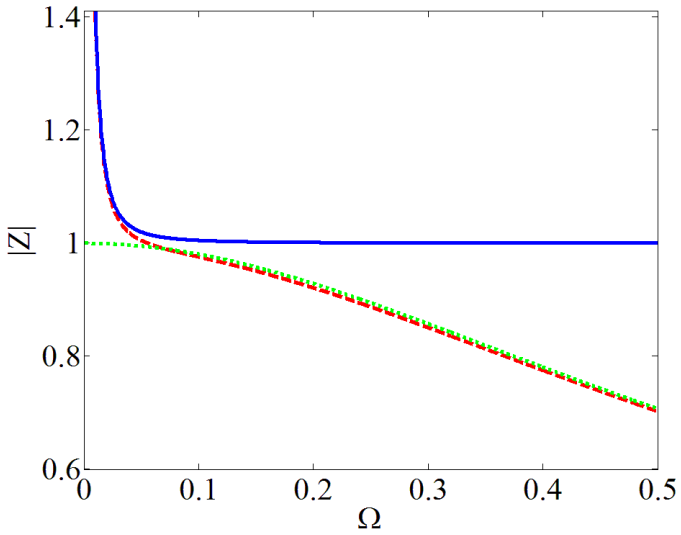

Figure 5.2. The magnitude of the impedance for $\bar{L} = 100$ found based on our general formula, Eq. 5.12, red dashed line, the approximate result of Eq. (5.14), blue solid line, and the thin double layer approximation, Eq. (5.15), green dotted line.

Let us now discuss the approximate formulas given by (5.14) in more detail. It is convenient to express them in dimensional terms,

$$\widehat{\rho_E} = -\frac{1}{2}\varepsilon V \frac{1}{\lambda_D^2}[1 + i\omega(\frac{L\lambda_D}{2D}\coth\left(\frac{L}{2\lambda_D}\right)]^{-1} \tag{5.16a}$$

$$\hat{Z} = \frac{\lambda_D^2 L}{\varepsilon D}\left(1 - \frac{2iD}{\omega L\lambda_D}\right) \tag{5.16b}$$

The scaling of frequency in our formulation is based on the inverse Debye time scale ($\tau_D = \frac{\lambda_D^2}{D}$), but the results clearly show emergence of another, intermediate time scale ($\tau_c = \frac{\lambda_D L}{D}$), through the term $\Omega\bar{L} = \omega\lambda_D L/(2D)$. We refer to this scale as intermediate since it is typically larger than diffusion time scale but it is still smaller than the bulk time scale ($\tau_B = L^2/D$) in the bulk electrolyte. The Debye time scale describes the initial evolution of the

system but it is very small, and consequently, it does not affect the charge accumulation characteristics. In the intermediate time scale regime, space charge density formula describes how the system achieves its stationary behavior.

5.2.2. Numerical Procedure

Numerical procedure was described in the previous study of Koklu et al.[199]. Briefly, the coupled PNP equations are solved in 1D using the Finite Element (FE) package, COMSOL Multiphysics 5.4. A finer mesh is introduced near the electrode boundaries to resolve transport in the thin EDL near the surface. In all cases, the initial cation and anion concentrations are set to bulk concentrations and the initial potential is set to zero, such that the system is at rest when $t = 0$. From $t = 0$ onward, we use a time stepping routine in combination with direct solution method (MUMPS) to compute the time dependent behavior of the system. Current density (A/m^2) at each time step is calculated at the electrodes.

For MPNP, the electrolyte solution consists of three regions corresponding to a combination of *Stern* layers of thickness H and diffuse layers near the electrode surfaces and bulk medium between them. Governing equations and boundary conditions are given in the Appendix B. More detailed information about the MPNP analysis can be found in Wang and Pilon article [163].

5.3. Results and Discussion

In our previous experimental study, the impedance spectra of 4 mm diameter gold electrodes in contact with different concentrations of KCl solution (24-114 mM and corresponding conductivities are 0.25-1 S/m) were measured in the 1 kHz-40 MHz frequency range at different channel heights (70-280 µm) [56].

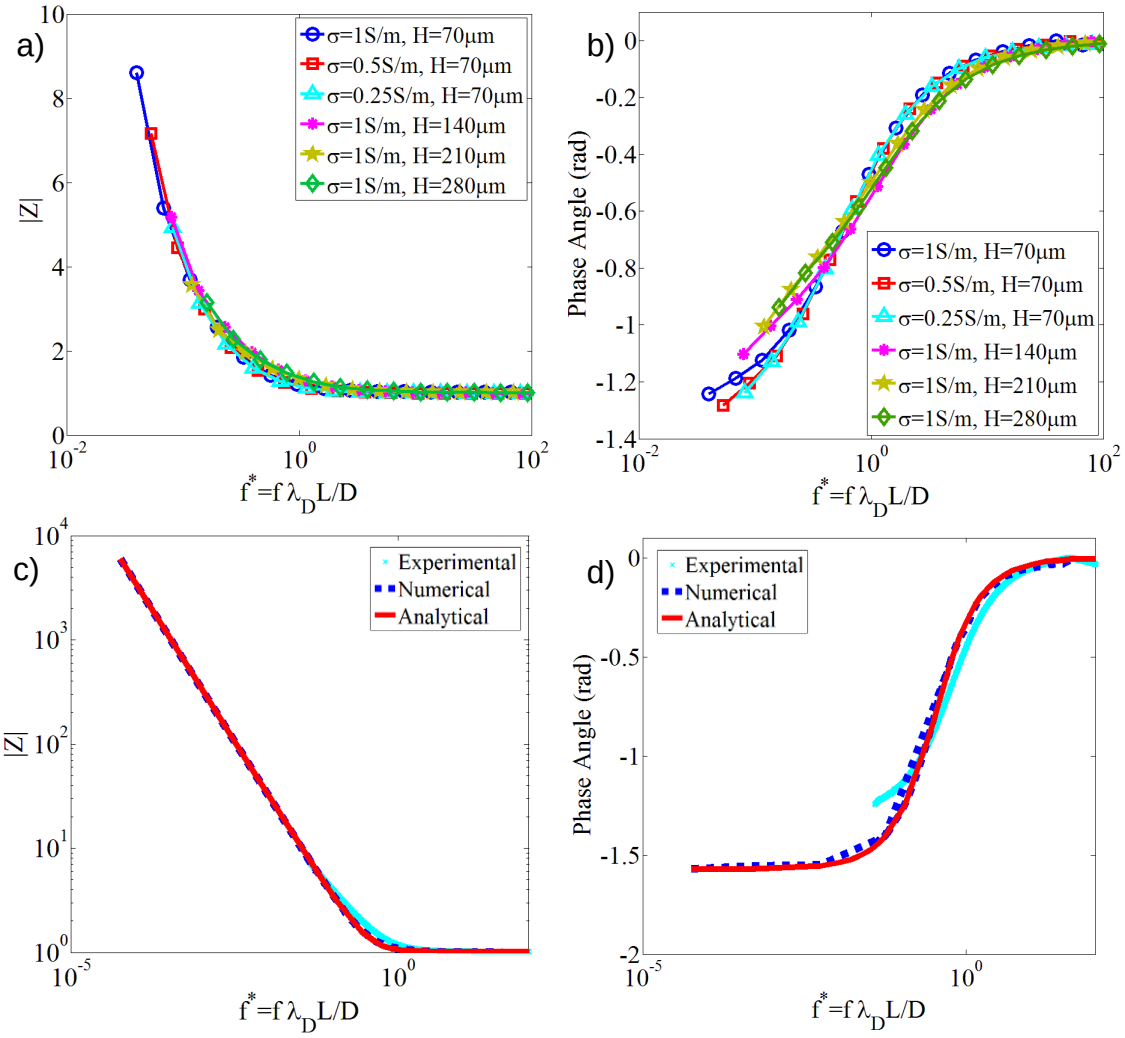

Figure 5.3. Normalized experimental impedance magnitude (a) and phase angle spectrum as a function of the normalized frequency (b) (Figures (a) and (b) are adapted from [47]). Experimentally (dotted light blue line), numerically (dashed dark blue line), and analytically (red solid line) obtained universal impedance magnitude (c) and phase (d) spectra for parallel plate electrode geometry.

Experiments were conducted at 20mV, which is lower than the thermal voltage. This avoids any Faradaic reactions and also satisfies small voltage conditions used in the analytical models. Each measurement was repeated at least three times and the average impedance magnitude and phase angle were reported. A universal scaling of the impedance spectra for all experiments was obtained when the impedance magnitude was normalized by the solution resistance and the frequency domain was nondimensionalized using the intermediate characteristic time ($\tau_c = \lambda_D L/D$) (Figure 5.3a and 5.3b). Details of experimental setup and procedure can be found in Koklu et al.[56]; these detailes are not repeated here. Instead, we focus on comparison with the newly developed analytical model and uncovering the universal scaling suggested by this model. For the parameter values corresponding to the experiment and the frequencies below 10 MHz, $\Omega \ll 1$ and thus the approximate formulas (5.14) are expected to be accurate enough to describe the experimental data (Figure 5.3c and 5.3d). As expected from the analytical equations, impedance magnitude increased with channel height and phase angle shifted to lower negative values. This behavior is consistent with experimentally and numerically obtained results. Below a certain frequency, the impedance magnitude increases with decreasing frequency and the phase angle approaches to $-\pi/2$ radians. These changes are indicative of a transition toward capacitive charging processes at the electrode/electrolyte interface. It is commonly accepted that frequency-independent impedance response of a microelectrode is attributed to the resistance of solution, which can be seen from the analytical results, where the phase angle approaches zero. Nondimensional impedance spectra obtained from equation 5.14 predicts the universal impedance behavior of electrodes at different channel heights and solution conductivities.

As discussed in the Introduction, one of our core objectives is to determine the transient space charge density. Equation 5.16a represents main features of the charge accumulation on the electrode surface. The applied potential drives the ions to move, which is reflected by a change of the ion concentrations near the electrodes.

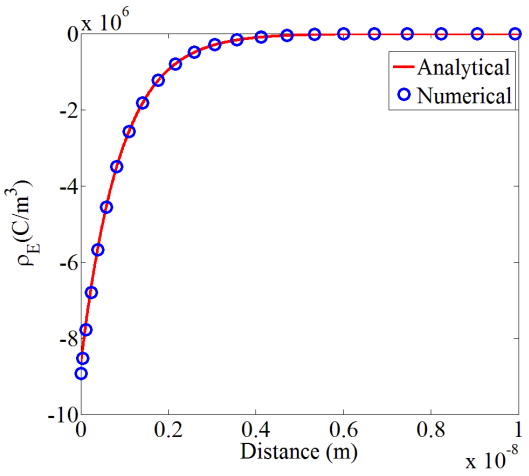

Figure 5.4. The profile of space charge density ($\rho_E(C/m^3)$) near the electrode excited at 1 kHz. The solution concentration is 114mM and channel height is 100nm. Data is shown at the highest applied voltage of 20 mV.

The change of space charge density near the electrode is shown in Figure 5.4 for a typical parallel plate capacitor system characterized by KCl ($D = 1.7\ 10^{-9}\ m^2 s^{-1}$, $\lambda_D = 1nm$, $L = 100nm$, $V = 20mV$ and $f = 1\ kHz$). This figure shows the space charge density distribution within 10 nm from the electrode. Our numerical and analytical results depict the same behavior, which shows the accuracy of the analytical model.

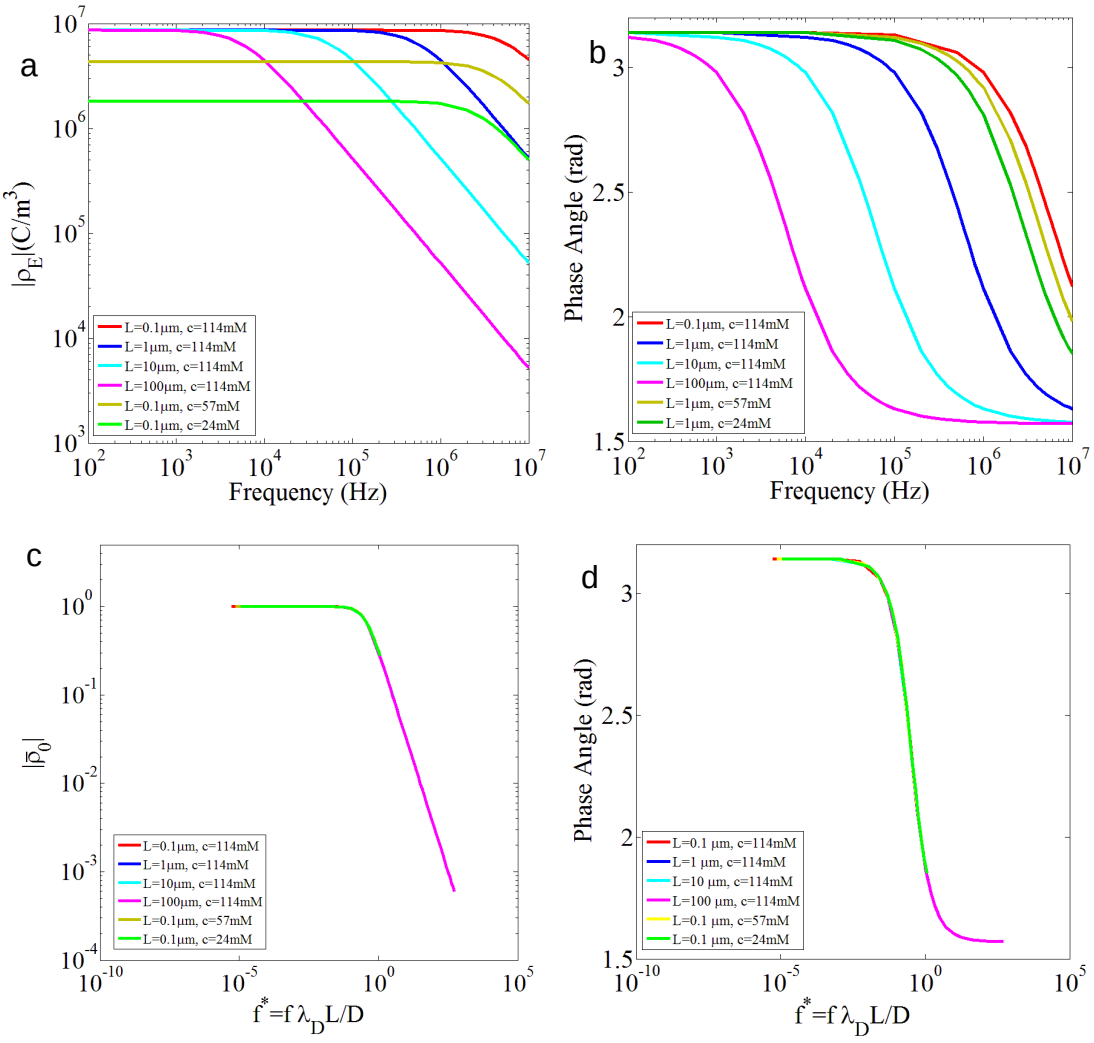

Figure 5.5. The magnitude (a) and phase angle (b) of space charge density on the excited electrode for different channel heights and electrolyte concentrations obtained using equation 5.16a. The magnitude (c) and phase angle (d) of dimensionless space charge density on the electrode ($x = 0$).

Space charge density cannot be directly obtained experimentally using impedance spectroscopy. Since analytically calculated impedance spectra is in well agreement with experimentally obtained one, equation (5.16a) can be used to define the corresponding space charge density. As a result, measurements of the impedance can be used as an indirect

way to quantify the surface charges. Figures 5.5a and 5.6b show the magnitude and phase of space charge density calculated by equation (5.16a) on the sinusoidally excited electrode ($x = 0$) for frequencies ranging from 100 Hz to 10 MHz, and for cases with different channel heights and solution concentrations. It is evident that the space charge density versus frequency curves differ significantly from one case to another. Increasing the value of L by a factor of four was found to have no effect at the low frequency regime ($f < 1\ kHz$) for 114 mM KCl solution, whereas the values of space charge density predicted at large frequencies were found to decrease with increasing L. This can be attributed to the fact that the charge storage or charge relaxation took longer as the domain length L increased under large frequencies. Then, the charge storage at large frequencies were limited as it could not follow the fast variation in the electric potential. Moreover, the space charge density becomes smaller for low concentration of solutions because the DC component of space charge density decreases with increasing the Debye length. Figure 5.5c consolidates all data as those shown in Figure 5.5a but ploted in terms of $\bar{\rho}$ as function of f^*. Similarly, Figure 5.5d is the same data used in Figure 5.5b but the frequency domain is normalized. First, it is remarkable that all curves in Figure 5.5a and 5.5b collapsed on a same curve irrespective of the different values of channel heights and solution concentrations. Second, Figure 5.5c and 5.5d indicate that two regimes can be clearly identified: (i) $f^* \ll 1$ corresponds to the quasi-equilibrium or ion diffusion independent regime and (ii) $f^* \gg 1$ corresponds to the ion diffuison limited regime. Unlike in the diffusion limited regime, ion transports in the diffusion independent regime are fast enough to follow the change of the surface potential.

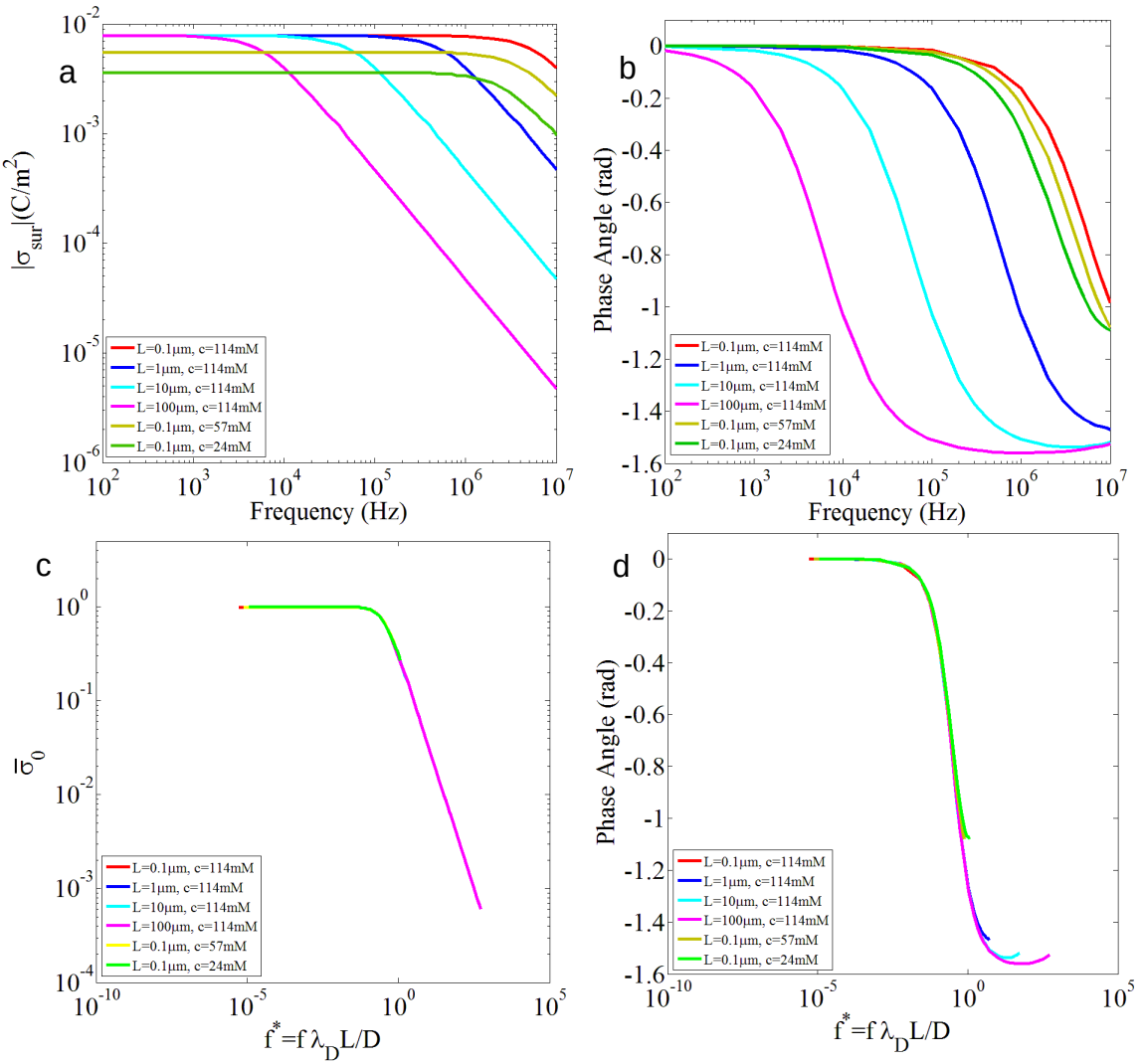

Figure 5.6. The magnitude (a) and phase angle (b) of surface charge density on the excited electrode for different channel heights and electrolyte concentration obtained using equation A12. The magnitude (c) and phase angle (d) of dimensionless surface charge density on the electrode ($x = 0$).

Same procedure was also applied for surface charge density on the excited electrode and its universal behavior for the same electrode separation distances and concentrations used for space charge density is shown in Figure 5.6. As it can be understood from equations A7, the magnitude of surface change density alters with Debye length. It is worth noting

that this analysis is valid in the case of binary and symmetric electrolytes. To the best our knowledge, the present study is the first in identifying self-similar behavior of space and surface charge density with binary symmetric electrolytes.

The validity of the proposed method for different concentration of solutions was investigated by numerically solving the MPNP equitation. So far, we have not considered the finite size of ions and treat ions as point-charges. Numerical simulations were repeated by accounting for the effect of finite ion size in modeling ion transport for concentrated solutions. Kilic et al. derived a MPNP model valid for binary and symmetric electrolytes for large electrolyte concentration [153, 158, 160]. They added an excess term in the expression of the electrochemical potential to account for the finite ion size. They solved the MPNP model numerically for a planar electrode and predicted the profiles of electric potential and ion concentrations in the diffuse layer. Their results demonstrated that under large electrolyte concentration, the predictions of the PNP model deviated significantly from the MPNP model due to the point charge assumption. We analyze numerical solutions of MPNP equations on our model and compare the outcome to that of the standard PNP equations. The length of the overall computational domain was $L = 100\,nm$ for all electrolyte concentrations. At low concentration of solutions, the results obtained with PNP were exactly same with those obtained with MPNP (Figure 5.7). After a critical solution concentration value, MPNP provides higher impedance and therefore, the numerical results start deviating from the analytical solution. The reason can be explained by considering the *Stern* layer. In MPNP, a Stern layer is added to account for finite size of ions and it generates an extra impedance at the electrode electrolyte interface, and hence, overall impedance of the system is increased. The critical concentration is approximately 100 mM

which corresponds to a ~1 S/m conductivity solution. We can conclude that the proposed normalized analytical equations can be used to determine impedance of electrode/electrolyte system, where the electrodes are excited at and below the thermal voltage limit in 100Hz to 10MHz frequency range and the electrolyte concentration is kept below 100mM.

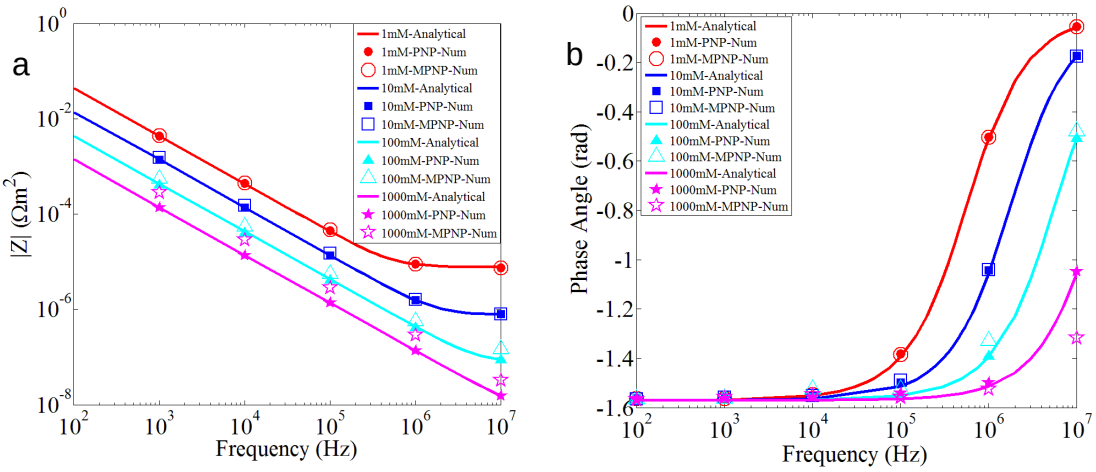

Figure 5.7. Impedance magnitude (a) and phase angle (b) obtained for varying concentration of solutions. Analytical solution (solid lines), and numerical solution of PNP (filled symbols), and MPNP (hollow symbols) results are shown.

5.3. Conclusions

We found the universal response of EP in parallel plate capacitor systems based on experimental, numerical, and analytical results for a number of conditions and electrode separation distances. We derived dimensionless analytical expressions for the impedance of parallel plate capacitor systems and showed that they agree with experimental and numerical results. Space and surface charge density equations were also analytically

derived by solving the PNP equations. The universal space and surface charge density behaviors were obtained after normalizing the magnitudes with their DC components and making the frequency spectrum dimensionless with the intermediate time scale, $\tau_c = \lambda_D L/D$. The validity of proposed analytical model for high concentration of solutions was investigated by numerically solving the MPNP equation which includes the *Stern* layer. The analytical model can successfully predict the impedance behavior when the critical concentration of solution is below 100mM ($\sigma \sim 1\, S/m$) and the electrical potential amplitude is less than the thermal voltage. The current analytical solutions in nondimensional form will enable prediction of the EP effect, space and surface charge density behaviors of parallel plate capacitor systems with different electrode separation and electrolyte concentration. In future work, the analytical solution will be extended for single disk electrodes where experimental and numerical data in reference [200] have shown EDL charging time scale based on electrode diameter, EDL thickness, and the diffusion coefficient.

5.4. Appendix

5.4.1. APPENDIX A: Derivation of Dimensionless Space/Surface Charge Density and Impedance

The solution of the ordinary differential equation for the scaled space charge density, Eq. (10a), is written as

$$\bar{\rho} = Ae^{\gamma_1 \bar{x}} + Be^{\gamma_2 \bar{x}}, \tag{A1}$$

where the complex numbers $\gamma_{1,2}$ ($\gamma_1 = \alpha + i\beta,\ \gamma_2 = \alpha - i\beta$) are the solutions of $\gamma^2 = 1 + 2i\Omega$. By solving the Poisson's equation, Eq. (10b), we obtain

$$\bar{\psi} = \frac{A}{2\gamma_1^2} e^{\gamma_1 \bar{x}} + \frac{B}{2\gamma_2^2} e^{\gamma_2 \bar{x}} + C_1 \bar{x} + C_2 \tag{A2}$$

Application of the four boundary conditions (for the potential and the ionic fluxes) at the endpoints of the interval leads to a system of linear equations for the four unknown coefficients in the solution,

$$1 = \frac{(A+B)}{2(1+2i\Omega)} + C_2 \tag{A3a}$$

$$0 = \frac{Ae^{\gamma_1 \bar{L}}}{2\gamma_1^2} + \frac{Be^{\gamma_2 \bar{L}}}{2\gamma_2^2} + C_1 \bar{L} + C_2 \tag{A3b}$$

$$\frac{A-B}{\alpha + i\beta} + 2C_1 = (\alpha + i\beta)(A-B) \tag{A3c}$$

$$0 = A(e^{\gamma_1 \bar{L}} - 1) - B(e^{\gamma_2 \bar{L}} - 1) \tag{A3d}$$

Solving this system gives the values of the coefficients,

$$\begin{aligned} A &= -Be^{-(\alpha+i\beta)\bar{L}} \\ &= (1 \\ &\quad + 2i\Omega)\left\{1 - e^{(\alpha+i\beta)\bar{L}} - i\Omega\bar{L}(\alpha \right. \\ &\quad \left. + i\beta)\left(1 + e^{(\alpha+i\beta)\bar{L}}\right)\right\}^{-1} \end{aligned} \tag{A4a}$$

$$C_1 = (1 + e^{(\alpha+i\beta)\bar{L}})\frac{i\Omega \mathrm{A}}{\alpha + i\beta} \tag{A4b}$$

$$C_2 = 1 + \frac{e^{(\alpha+i\beta)\bar{L}} - 1}{2(1 + 2i\Omega)}A \tag{A4c}$$

With these values, the solutions for both space charge density and potential as functions of the coordinate are completely determined and can then be used to find all quantities of interest for applications. In particular, using Eq. (A1) at $x = 0$ gives the value of space charge density near the electrode, Eq.(11). To determine the complex impedance, we note that the dimensional displacement current (D_c) is found from

$$D_c = -\varepsilon \frac{\partial \hat{\psi}}{\partial x}\bigg|_{x=0} \tag{A5}$$

while the dimensional impedance is

$$V\left(\frac{\partial D_c}{\partial t}^{-1}\right) \tag{A6}$$

Let us now introduce nondimensional complex impedance Z scaled by the solution resistance $R_{sol} = \frac{\lambda_D^2 L}{\varepsilon D}$. Using (A5 – A6) together with the known solution for the potential, Eq. (A2), we find the result for Z given by Eq. 5.12.

We also note that surface charge density ($x = 0$) can be calculated from the following equations

$$\widehat{\sigma_{sur}} = -\varepsilon \frac{\partial \hat{\psi}}{\partial x}\bigg|_{x=0} \tag{A7a}$$

$$\widehat{\sigma_{sur}} = -\frac{V\varepsilon}{2\lambda_D}\frac{(1+i\Omega\lambda_D)(1+2i\Omega\lambda_D)\,(1-i\Omega L\lambda_D)}{(1+\Omega^2L^2)} \tag{A7b}$$

$$\sigma_{DC} = -\frac{1}{2}\varepsilon V\frac{1}{\lambda_D} \tag{A7c}$$

Dimensionless surface charge density is

$$\bar{\sigma}_0 = \frac{(1+i\Omega)(1+2i\Omega)\,(1-i\Omega\bar{L})}{(1+\Omega^2\bar{L}^2)} \tag{A8}$$

5.4.2. APPENDIX B: Governing Equations and Boundary Conditions for MPNP

The local electric potential $\psi(x,t)$ and ion concentrations $c_i(x,t)$ in the electrolyte solution were computed by solving (i) the Poisson and MPNP 1D model in the diffuse layer for large electrolyte concentration,

$$\frac{\partial}{\partial x}\left(\varepsilon\frac{\partial\psi}{\partial x}\right) = \begin{cases} 0 & for\ \ 0 \le x < H\ and\ for\ \ L-H \le x < L \\ eN_Az(c_1-c_2) & for\ \ H \le x \le L-H \end{cases} \tag{B1a}$$

$$\frac{\partial c_i}{\partial t} = \frac{\partial}{\partial x}\left(D\frac{\partial c_i}{\partial x} + \frac{z_iD}{R_uT}Fc_i\frac{\partial\psi}{\partial x} + \frac{\upsilon Dc_i}{2c_\infty - \upsilon(c_1+c_2)}\frac{\partial(c_1+c_2)}{\partial x}\right) \tag{B1b}$$

The packing parameter is defined as $\upsilon = 2a^3N_Ac_\infty$ where a is the effective ion diameter, taken as $a = 0.66\,nm$ and *H* is the *Stern* layers thickness. It represents the ratio of the total bulk ion concentration to the maximum ion concentration $c_m = 1/N_Aa^3$ assuming a simple cubic ion packing. Therefore, υ should not be larger than unity for the model to be physically acceptable. It is clear that the equations given above reduce to the classical

Poisson-Nernst-Planck model when $\upsilon = 0$. The associated boundary and initial conditions were given by

$$\psi(x = 0, t) = \psi^{AC}\sin(\omega t) \tag{B2a}$$

$$\psi|_{x=H^-} = \psi|_{x=H^+} \quad and \quad \varepsilon_0\varepsilon_r \frac{\partial\psi}{\partial x}\Big|_{x=H^-} = \varepsilon_0\varepsilon_r \frac{\partial\psi}{\partial x}\Big|_{x=H^+}$$

$$\psi|_{x=(L-H)^-} = \psi|_{x=(L-H)^+} \quad and \quad \varepsilon_0\varepsilon_r \frac{\partial\psi}{\partial x}\Big|_{x=(L-H)^-} = \varepsilon_0\varepsilon_r \frac{\partial\psi}{\partial x}\Big|_{x=(L-H)^+} \tag{B2b}$$

$$D\frac{\partial c_i}{\partial x} + \frac{z_i D}{R_u T} F c_i \frac{\partial\psi}{\partial x} + \frac{\upsilon D c_i}{2c_\infty - \upsilon(c_1 + c_2)} \frac{\partial(c_1 + c_2)}{\partial x} = 0, at\ x = H\ and\ x = L - H \tag{B2c}$$

$$\psi(x = L, t) = 0 \tag{B2d}$$

$$\psi(x, t = 0) = 0 \quad and \quad c_i(x, t = 0) = c_\infty \ for\ 0 \le x \le L \tag{B2e}$$

Note that the surface electric potential $\psi(t)$ in equation (B2a) was used for the analytical derivation. Equation (B2b) states that the electric potential and displacement were continuous across the Stern/diffuse layer interface located at $x = H$. Equation (B2c) indicates that the mass fluxes vanish for both ion species at the electrode surface since there are no reactions on the electrode surface. Equations (B2d) and (B2e) are the initial conditions. The electrolyte concentration was varied from 1mM to1M so that the classical PNP model remained valid for low concentration and lost validity for high concentration

cases. In addition, the Stern layer thickness H was approximated as the radius of solvated ions, i.e., $H = a/2 = 0.33\,nm$.

Chapter 6

SELF-SIMILAR INTERFACIAL IMPEDANCE OF ELECTRODES IN HIGH CONDUCTIVITY MEDIA: II. DISK ELECTRODES

EP effects were investigated using impedance spectroscopy measurements for planar and nanorod-structured gold disk electrodes in the100 Hz - 1 MHz frequency range and in 0.25 S/m to 1.5 S/m conductivity KCl solutions. The diameters of the planar electrodes were varied from 50 μm to 2 mm to examine the effect of electrode size on impedance spectra. Normalizing the impedance magnitude with the spreading resistance, and frequency with the characteristic time scale, all experimental data collapsed on to a universal curve, proving self-similarity. Experimental impedance results were compared well with those obtained from the numerical solution of Poisson-Nernst-Planck equations in an axisymmetric domain. The influence of surface morphology was also investigated by generating cylindrical nanorods on a planar electrode. The 500 μm diameter electrode surface was covered with cylindrical nanorods with known height, diameter, and separation distance, which were characterized using scanning electron microscopy. The characteristic time scale for the nanorod-structured electrode increased by the surface enlargement factor obtained by cyclic voltammetry measurements. Self-similar interfacial impedance of electrodes was modeled using a constant phase element model. Current findings describe the coupled effects of electrode diameter, electrolyte conductivity, and electrode surface morphology on the impedance spectra of electrode/electrolye system, when the electric double layer between the nanorods does not overlap.

6.1. Materials and Methods

6.1.1. Planar Electrode Fabrication

Gold electrodes were fabricated using standard photolithography technique as previously described in Chapter 2 [5]. Briefly, glass slides, which are 2.5 cm × 2.5 cm, were cleaned using standard cleaning procedure. After the cleaning, the substrates were dried using Nitrogen gas flow. Then, the disk electrodes at different diameters (50µm, 200µm, 500µm, and 2000µm) were patterned using standard photolithography techniques. After which, the substrates were coated with chromium (120 mA—60s) and gold (80 mA—120 s) layers using a sputter coater (EMS300TD, Emitech), respectively. Finally, copper tape (3M) was used as terminal lead for impedance measurements. The tape were bonded using conductive silver epoxy (MG Chemicals).

6.1.2. Nanorod Patterning of Planar Electrodes

The nanopatterning of the surface of the gold electrodes was performed using the template-assisted electrodeposition method reported in ref [102]. Here, a nanoporous anodic aluminum oxide (AAO) previously transferred to the planar gold electrode surface was used as a template during the electrodeposition of nickel and gold. Segmented composition nickel (105 ± 12 nm) /gold (105 ± 12 nm) nanorods were grown within the pores of the AAO template by electrodeposition using a CHI 660 electrochemical working station in a three-electrode configuration. The initial nickel segment was electrodeposited using a nickel sulfamate solution (Technic Inc.) at a constant potential of -0.935 mV for 15 seconds. The sample was rinsed with deionized (DI) water and dried with Nitrogen gas. The gold segment of the nanorods was electrodeposited using an Orotemp 24 RTU Rack

(Technic Inc.) solution at a constant potential of -0.9 mV for 50 seconds. The coverage of the electrode and the shape of the nanorods were verified by scanning electron microscopy (SEM). The nanorod average diameter (d), height (h), and separation distance (l) were determined using a Microscopy Image Segmentation Tool (MIST) [201]. We have found that the deposition of an initial nickel segment improved the adhesion and coverage of the gold electrode with nanorods as shown in Figure 6.1.

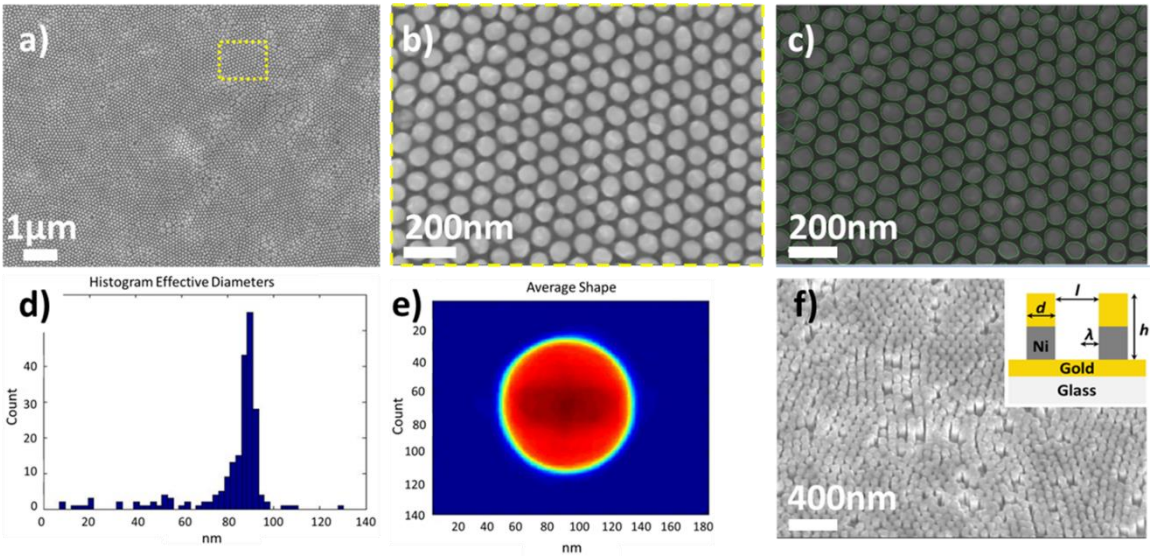

Figure 6.1. SEM analysis of the nanorod patterned electrodes. a) Top view of the array of nickel (Ni) (~105 ± 12 nm)/ gold (Au) (~105 ± 12 nm) nanorods. b) Magnified-in view of the nanorods. c) Statistical analysis of the array of rods performed by MIST. d) The histogram of average nanorod diameter. e) The average shape of the nanorods is shown as a well-defined cylindrical rod. f) Tilted view of the nanorods. Inset shows the dimensions used in the theoretical model. Nanorod dimensions are height (h=210 ± 12), diameter (d=85 ± 8 nm) and separation distance (l=21 ± 8 nm).

To have consistent notation in the following sections, we denote the nanorod electrodes with N and planar with P. Process flow of fabrication of P and N electrodes is shown in Figure 6.2 with the relevant dimensions.

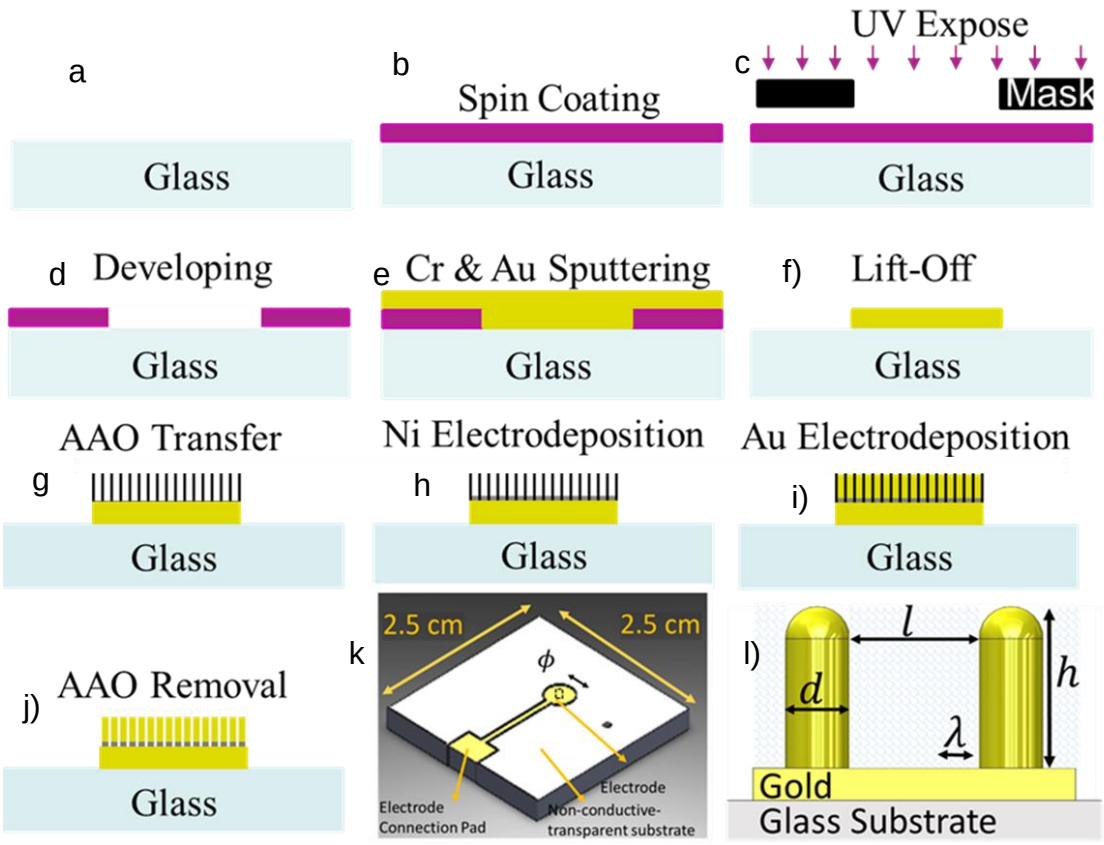

Figure 6.2. Process flow of electrode fabrication (a-j) and schematics of gold disc electrode with relevant dimensions (k). The electrode surface is coated with cylindrical nanorods with known height (h), diameter (d) and separation distance (l) (l). λ is the Debye length.

6.1.3. Impedance Measurements

After the 50 µm, 200 µm, 500 µm, and 2000 µm diameter electrodes were fabricated, their connection pads were encapsulated with a dielectric material (double sided tape) to keep the electrode/electrolyte interfacial area constant. A polycarbonate cylindrical chamber (2 cm diameter, 3 cm height) was attached to the substrate using epoxy and the electrode was centered in the chamber. After cleaning the electrodes with DI water and drying with Nitrogen, impedance measurements were carried out in a two-point electrode configuration

using a platinum wire (MW-4130, BASI) as a counter electrode [52]. The counter electrode was mounted on a vertical shaft through a linear rail guide used to fix the distance between electrodes. The counter electrode was immersed 2 cm above the working electrode for all measurements. Before each measurement, an open-short compensation of the analyzer was performed. The impedance spectra of different concentration KCl solutions were measured using a high precision impedance analyzer (4194A, Agilent) in a frequency range of 100 Hz-1 MHz. The working and counter electrodes were connected to the low and high terminals of the impedance analyzer using a test fixture (HP 16047A) in a 4-terminal configuration. An alternating voltage signal of 20 mV peak to peak amplitude was applied, where Faradaic reactions and electrolysis of water at the electrode/electrolyte interface can be neglected.

6.1.4. Normalization Parameters

In the electrode-electrolyte systems, impedance a the high frequency range (~ 1 MHz) is purely due to solution resistance (R_{sol}). For disk electrode geometry, the value of resistance, commonly referred to as the spreading resistance, is determined by the Newman's relation [50]:

$$R_{sol} = \frac{1}{2\sigma\phi} \tag{6.1}$$

where ϕ is the electrode diameter and σ is the electrolyte conductivity. The relaxation time for charging of the EDL is considered to depend on the electrode diameter, and EDL thickness [196]. Therefore, the primary characteristic time scale for a disk electrode in contact with an electrolyte can be written as:

$$\tau_c = \lambda\phi/D \tag{6.2}$$

λ is calculated using the following equation:

$$\lambda = \sqrt{\frac{\varepsilon \mathrm{RT}}{\sum_{i=1}^{N} \mathrm{z_i}^2 \mathrm{F}^2 c_i}} \tag{6.3}$$

where ε is the dielectric permittivity, z_i and c_i are the valance and ionic concentration of i^{th} ionic component, F is the Faraday's constant (F=96485 C/mol), R and T denote the universal gas constant and absolute temperature, respectively. For planar surface electrodes, we present the impedance spectrum using a dimensionless frequency:

$$f^* = f \times \tau_c \tag{6.4}$$

where f is the applied AC field frequency.

6.1.4. Numerical Simulations

Experimental results are related with theory using numerical simulations. The computational domain is 2D axisymmetric and contains a dilute, completely dissociated electrolyte between a working and a counter electrode. The simulation domain is illustrated in Figure 6.3.

The concentrations of ions inside the electrolyte (K^+ and Cl^-) are described by the Nernst-Planck equation:

$$\frac{\partial c_i}{\partial t} + \boldsymbol{\nabla} \cdot \left(-D_i \boldsymbol{\nabla} c_i - \frac{z_i D_i F c_i}{RT} \boldsymbol{\nabla} \psi \right) = 0 \tag{6.5}$$

where D_i is the diffusion coefficient of species i and ψ is the electric potential. The electric field in the media is governed by Poisson equation:

$$\nabla \cdot (\varepsilon \boldsymbol{E}) = F \sum_i z_i c_i \tag{6.6}$$

where, $\boldsymbol{E}$ is the electric field ($\boldsymbol{E} = -\nabla\psi$).

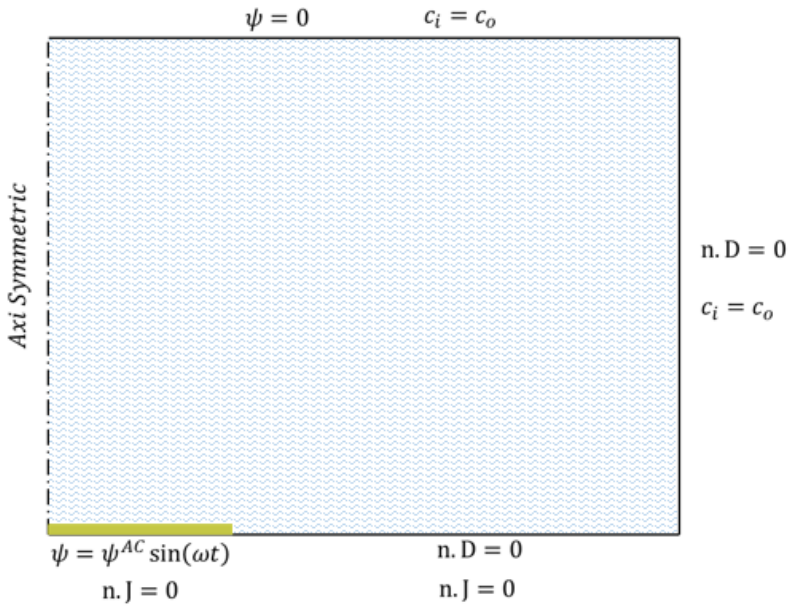

Figure 6.3. Computational domain and the boundary conditions for gold planar electrodes. Yellow region represents the electrode.

The simulation parameters and the boundary conditions are as follows. The operating temperature is 300 K and diffusivities of K^+ and Cl^- ions are fixed at 1.7×10^{-9} m^2/s. The relative permittivity of medium is taken to be 80. The top boundary is grounded, and the electrode boundary is subjected to a sinusoidal electric potential:

$$\psi = \psi^{AC} \sin(\omega t) \tag{6.7}$$

ψ^{AC} is the amplitude of AC electric potential (20 mV), and ω is the angular frequency ($\omega = 2\pi f$). All other boundaries have zero charge except the left boundary, which is

axisymmetric. The bottom boundary is considered ideally polarizable without Faradic processes, so the ionic fluxes vanish at this boundary ($\boldsymbol{n} \cdot \boldsymbol{J}_i = 0$), while all the other boundaries are subjected to bulk ionic concentrations except the line of symmetry in the middle. The initial cation and anion concentrations are set to the bulk concentrations and the initial potential is set to zero. The domain height is large enough so that the current is not changing with further increase of the domain size. COMSOL Multiphysics software was used to solve the coupled PNP equations. Current at each time step was calculated using the following integral equation at any cross section. Then, it was represented as the AC voltage with a phase shift:

$$\boldsymbol{J} = F \int \sum_i z_i \boldsymbol{J}_i = \mathrm{J} \sin(\omega t - \varphi) \tag{6.8}$$

where J is the current amplitude and φ shows the phase angle. Impedance of the system at each frequency is then calculated by complex ratio of the voltage to the current:

$$Z = \frac{\psi}{J} = \left| \frac{\psi^{AC}}{\mathrm{J}} \right| \angle\varphi = |Z| \angle\varphi \tag{6.9}$$

6.1.5. Cyclic Voltammetry (CV)

CV was used to attain the ratio of the effective to geometric surface area, which is relevant for quantifying the surface area enhancement in N electrodes. Ultrapure DI water (EMD Millipore) was used to prepare the electrolyte for CV measurements. The solution concentration was 2 mM potassium ferricyanide ($K_3Fe(CN)_6$) in 0.1M KCl and the scan rate was kept at 10 mV s^{-1}. The CV measurement was performed using a potentiostat

(EZstatPro, Nuvant) in a three-electrode setup where the studied electrode is the working electrode, a platinum wire is the counter electrode and Ag/AgCl electrode (MF-2052, BASI) is the reference electrode. EZstat pro software was used to record the current versus potential spectra during the CV measurements.

6.2. Results and Discussion

Four different gold P disk electrodes with $50\ \mu m, 200\ \mu m, 500\ \mu m,$ and $2000\ \mu m$ diameters were fabricated to investigate the effect of electrode diameter on the τ_c.

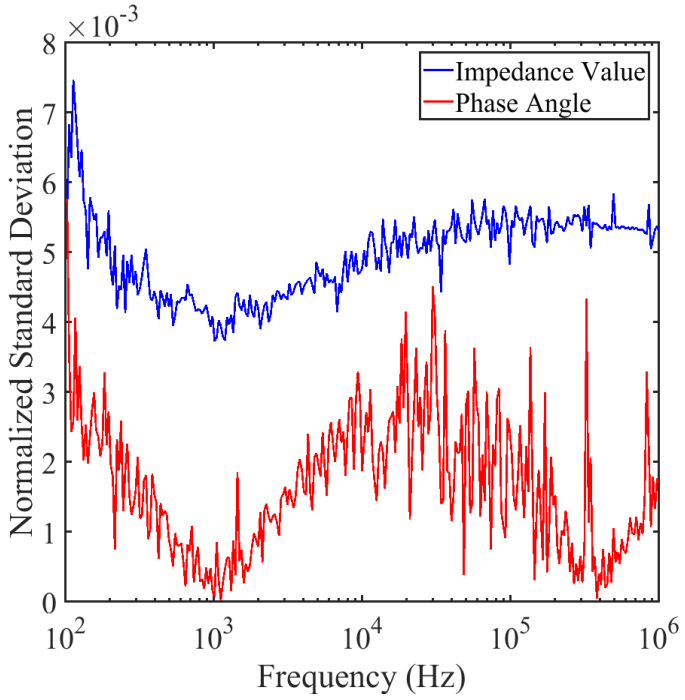

Figure 6.4. Normalized standard deviation of a) impedance magnitude, and b) phase angle for 50 μm planar gold electrode in contact with 1.5 S/m KCl solution.

The chamber was filled with 137 mM KCl solution ($\sigma = 1.5\, S/m$), and impedance measurements were carried out in a frequency range of 100 Hz - 1 MHz. In the next step, electrode diameter was kept constant at $\phi = 50\, \mu m$, and the impedance measurements were conducted using KCl solutions with 137, 100, and 25 mM concentrations. All the impedance measurements were repeated at least three times and the averaged impedance magnitude and phase angle spectra are reported. Figure 6.4 shows the normalized standard deviation of the impedance magnitude and the phase angle for the 50 µm diameter electrode in contact with 1.5 S/m KCl solution which gives the highest standard deviation.

The normalized standard deviation in all cases is less than 1%. Figure 6.5a and 6.5b show the impedance value and phase angle spectrum of the P electrodes. As the electrode size decreases, the magnitude of the impedance increases, which is consistent with the impedance behavior of a capacitor. At frequencies below 100 kHz, the impedance magnitude increased with decreasing frequency and the phase angle value shifted towards $-\pi/2$ radians. These changes are indicative of a transition towards capacitive charging processes at the electrode surface.

It is commonly accepted that frequency-independent impedance response of a microelectrode is attributed to the R_{sol} where the phase angle approaches zero. Impedance magnitudes given in Figure 6.5a were normalized with the analytically calculated R_{sol} for each case, and the characteristic time τ_c was used to make the frequency domain dimensionless.

Debye lengths were calculated using equation (6.3), resulting in 0.82, 0.97, and 1.90 nm for 137, 100, and 25 mM KCl solutions, respectively.

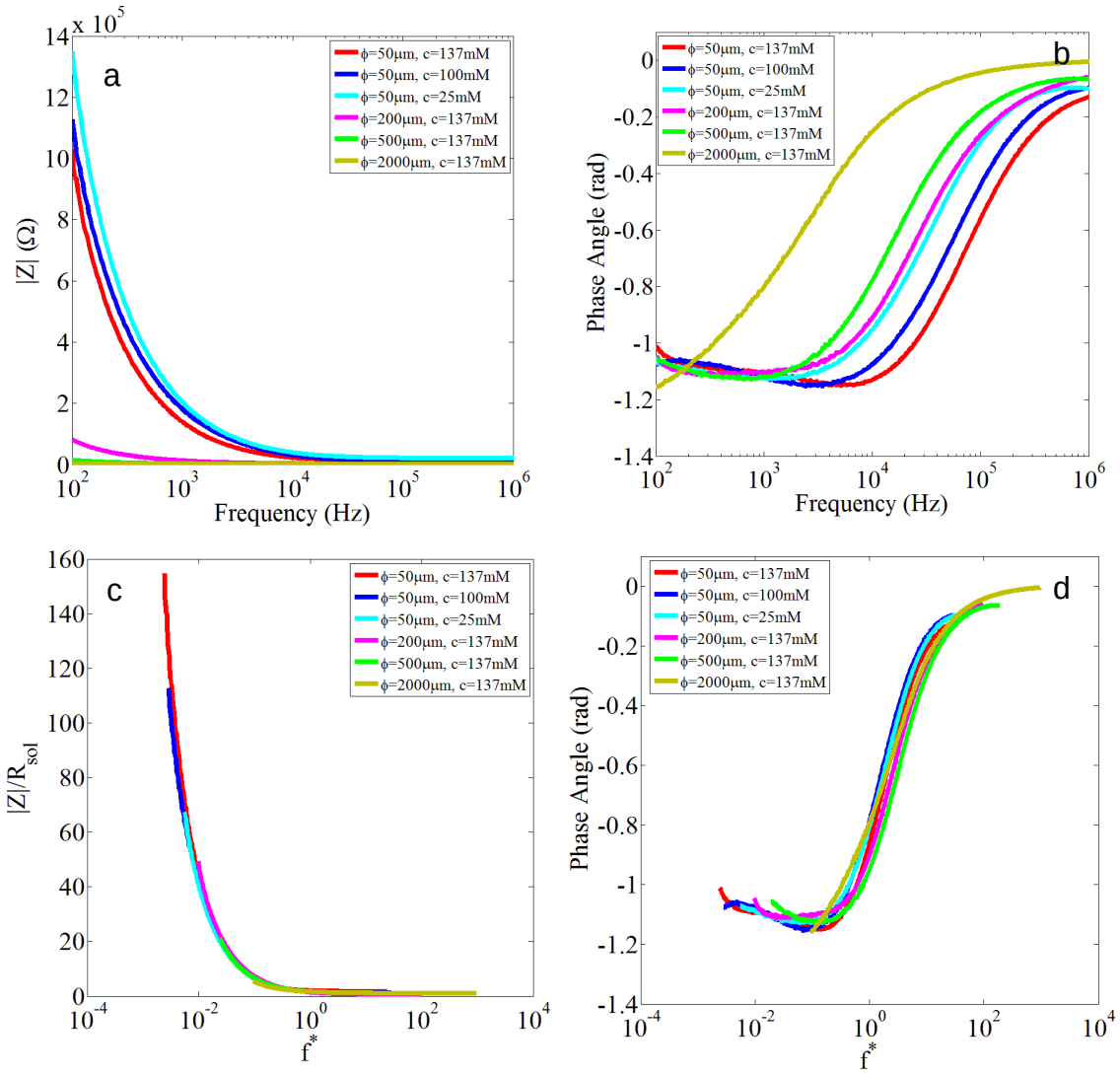

Figure 6.5. (a) Experimental impedance value and (b) phase angle spectrum at various KCl concentrations and different electrode diameters. (c) Normalized experimental impedance magnitude and (d) phase angle spectrum as a function of the dimensionless frequency.

The normalized impedance spectra are shown in Figure 6.5c and 6.5d. A rescaling of Figures 6.5a and 6.5b using the dimensionless frequency (f^*) reveals a universal impedance behavior for the current measurement system. The impedance magnitude and

phase angle of each measured data collapses to a single line, revealing self-similarity of the normalized impedance spectra.

Recently, Hasni et al. investigated the electrode size effect on the impedance spectra of PBS ($\sigma_{PBS} = 1.5\ S/m$) using gold disk electrodes via the two-electrode system described in the impedance measurement section [52].

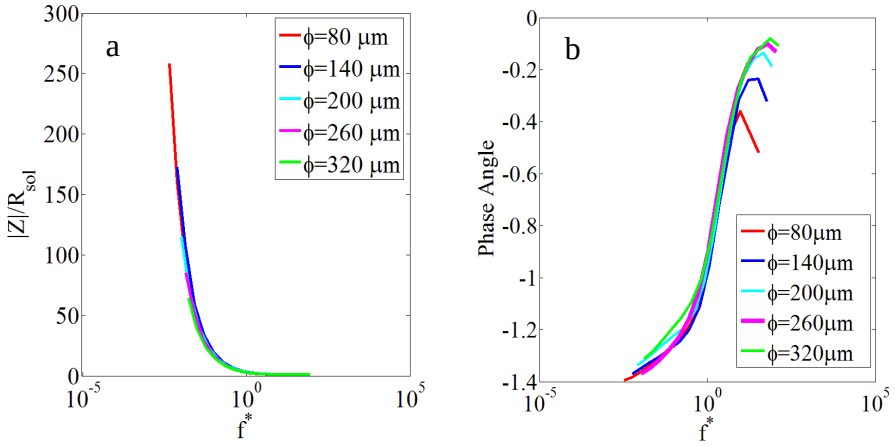

Figure 6.6. Self-similar impedance spectra obtained with disc electrodes in phosphate buffer saline solution (PBS, $\sigma = 1.5\ S/m$) from 100 Hz to 1MHz. Using the experimental data in REF [52].

Their electrode diameters varied from 20 μm to 320 μm with a systematic increase in the impedance by decreasing the electrode size. Their data were extracted using the plot digitizer software [202] and dimensionless impedance spectrum for their experiments is given in the Figure 6.6. The impedance magnitude and phase angle spectra converged to a single line, similar to our observations. The dependence of impedance spectrum on disk microelectrode diameters was also examined by Ahuja et al. in PBS ($\sigma_{PBS} = 1.54\ S/m$).

They fabricated platinum microelectrode arrays of different diameters on a single substrate and impedance measurements were performed over a wide frequency range, from 0.01 Hz to 100 kHz [51]. To maintain the lowest frequency limit consistent with our study, impedance magnitude and phase angle results were extracted from 100 Hz to 100 kHz. Their results also collapsed to a single line after our proposed normalization (Figure 6.7).

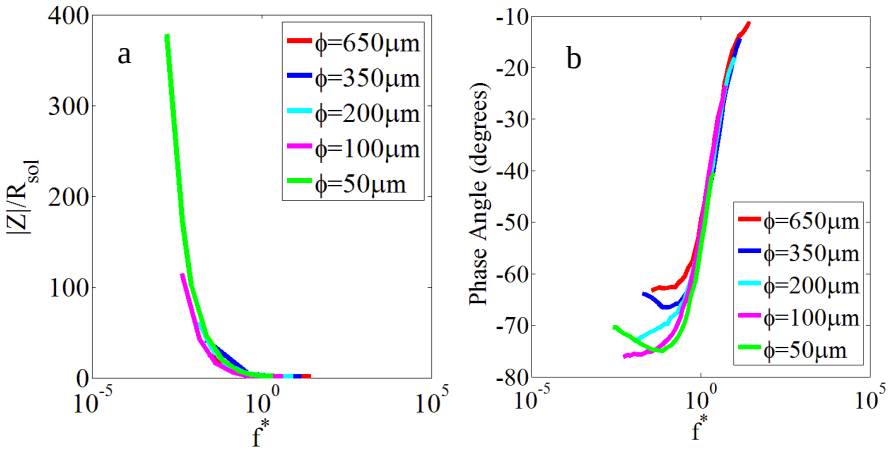

Figure 6.7. Self-similar impedance spectra obtained with disc electrodes in phosphate buffer saline solution (PBS, $\sigma = 1.5\ S/m$) from 100 Hz to 1MHz Using the experimental data in REF [51].

Time dependent numerical simulations of fully coupled PNP equations were performed using a frequency range of 100 Hz to 1 MHz in COMSOL Multiphysics 5.3a. First, numerical simulations were conducted by fixing the concentration of the solution at 137 mM and varying the diameter of the electrodes from 50 μm to 2000 μm, equivalent to the electrode sizes used in the experiments. Then the diameter of the electrode was fixed at 50 μm and the solution concentration was changed from 25 mM to 137 mM. The impedance

magnitude at each frequency was normalized with R_{sol}. Figures 6.8a and 6.8b show the normalized numerical impedance magnitudes and phase angles versus the dimensionless frequency (f^*).

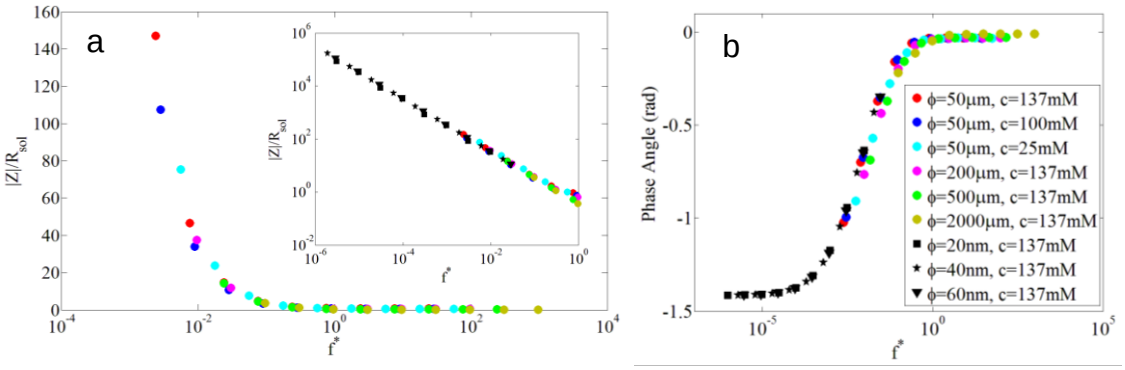

Figure 6.8. (a) Normalized numerical impedance magnitude and (b) phase angle spectrum as a function of the dimensionless characteristic frequency. Dimensionless impedance magnitude is shown in inset figure in logarithmic scale.

Upon proper normalization, all impedance values and phase angles calculated for the various electrode diameters and conductivities reduce to a universal line. The impedance magnitudes attained with the numerical simulation were very close to the experimental results in all frequency spectra, however a discrepancy was observed at low frequency between the numerically and experimentally obtained phase angles. Specifically, a phase angle shift towards zero happens at lower normalized frequencies in the simulations compared to that of the experiments. Numerical simulations were also conducted for 20 nm, 40 nm, and 60 nm diameter electrodes in 137 mM KCl solution to further investigate the validity of self-similar impedance spectra at nano-scales. The impedance spectra of nano size electrodes are shown by the black symbols in Figure 6.8a and 6.8b, and they maintain the universal impedance behavior. Normalized impedance values for the nano-

electrodes are three orders of magnitudes larger than that of the micro-electrodes, and the normalized impedance amplitude drops exponentially for $f^* < 10^{-2}$. Comparing the experimental and numerical results show that unsteady, 2D axisymmetric, fully coupled PNP equations without Faradic reactions can successfully predict the electrical impedance behavior of microelectrodes at different electrode diameters and solution conductivities.

Reduction of the EP effect due to increased surface area was investigated using the N electrode. The surface morphology of 500 µm diameter N electrode was characterized by SEM at 5kV and varying magnification factors. SEM images of N surface are shown in Figure 6.1. After electrochemical deposition, nanorods were obtained with high density and they covered almost 50% of the P electrode surface. The characteristic dimensions of nanorods defined in the inset of Figure 1d, were measured SEM and analyzed by MIST as $d = 85 \pm 8$ nm, $h = 210 \pm 12$ nm, and $l = 21 \pm 8nm$, respectively. The average nanorod height was obtained from SEM images taken at 45 degree inclination at various locations on the electrode. The total height of the nanorod was calculated using trigonometry as shown in Figure 6.9.

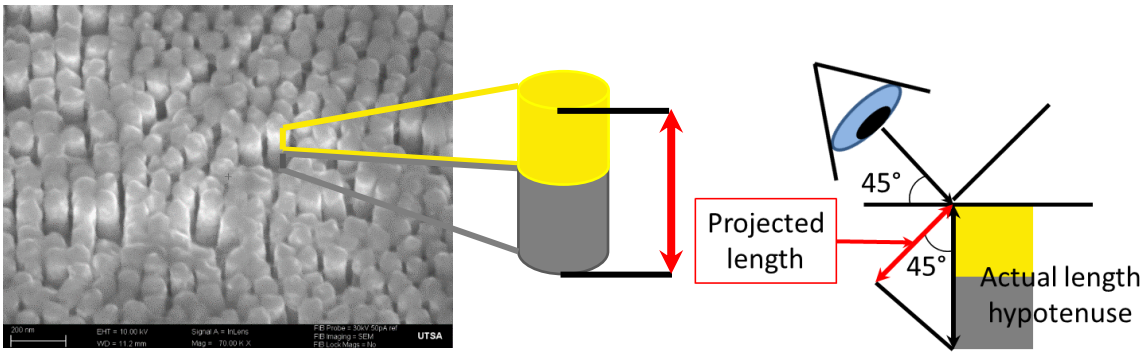

Figure 6.9. SEM image of nanorods taken at a 45° angle with a depiction of nanorod viewing angle for height determination.

To obtain a statistically meaningful value, 46 fully exposed nanorods where the top and bottom could be easily ascertained were measured, resulting in an average total height of 210 ± 12 nm. The error value corresponds to the standard deviation of the measurements. The height of both the Au and Ni segments were calculated in the same manner as above and respectively are 105 ± 12 nm.

Knowledge of these dimensions enables accurate surface area calculations. The surface enlargement factor was calculated using the standard unit cell for a hexagonal array as illustrated in Figure 6.10a. Microscopy Image Segmentation Tool (MIST) software [201] statistically analyzes SEM images to determine the average diameter, center-to-center nanorod distance and unit cell area Figure 6.10b). The average nanorod diameter (d) was 85 ± 8 nm and the average nanorod separation (l) of 21 ± 8 nm was calculated by subtracting the nanorod diameter from the center-to-center distance. The unit cell area (A_{unit}) (indicated with a red parallelogram) obtained by the MIST histogram was 9800± 550 nm^2 Figure 6.10c). The area of the nanorod side ($A_{nanorod}$) 56100 ± 2100 nm^2 was calculated by multiplying the nanorod height by the circumference, which was calculated using the MIST diameter Figure 6.1c. The surface enlargement factor (C) is calculated by:

$$C = \frac{A_{unit} + A_{nanorod}}{A_{unit}} \tag{6.10}$$

$C = 6.71 \pm 0.40$ which is close to the experimentally obtained enlargement factor $C = 6.51$. The error is calculated at ~2.98%.

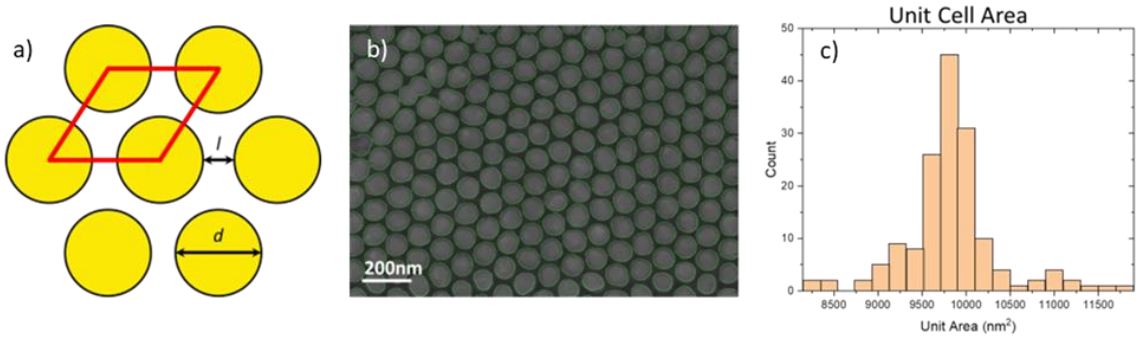

Figure 6.10. a) Unit cell diagram. b) SEM image of selected nanorods for MIST analysis. c) Unit cell area analysis.

Impedance measurements were repeated for N coated electrodes using 137 mM KCl ($\lambda = 0.82\,nm$) solution which induces a thin EDL. The separation distance used and concentration of solution ensure that the EDL does not overlap between the nanorod surfaces. Figure 6.11 shows comparison of the impedance magnitudes (a) and phase angles (b) obtained for P and N electrodes in a 1.5 S/m (137 mM) KCl solution. Based on the normalized impedance spectra, the results show that N electrodes the decreased the EP effect and extended the practical frequency range. Moreover, R_{sol} remains constant for the N electrode since the solution resistance is dependent on the foot-print area, not the effective surface area.

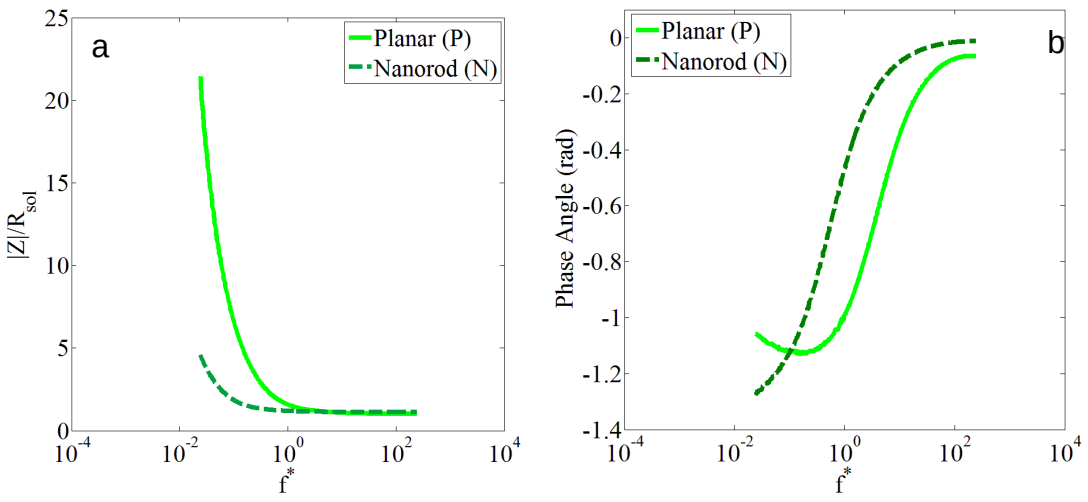

Figure 6.11. Normalized impedance values (a) and phase angles (b) obtained with 500 µm diameter P (solid line) and N (dashed line) electrodes in 137mM KCl solution.

Data shows a nearly 4.65 fold reduction in the interfacial impedance for the N electrode compared with P electrode at the lowest frequency. The universal impedance behavior was altered for the N electrode. We scaled the charging time, τ_c, with a constant to maintain the universal impedance behavior, and defined a new time constant τ_n for N electrode as:

$$\tau_n = C\tau_c \tag{6.11}$$

where C is the ratio of the effective polarizable surface area to the electrode foot-print area (i.e., the surface enlargement factor). This approach is valid for cases where the EDL around the nanorods does not overlap. The C was obtained by CV. Figure 6.12 shows the CV plots corresponding to 500 µm diameter P (solid line) and N (dashed line) electrodes measured in 2mM $K_3[Fe(CN)_6]$ + 0.1M KCl at a scan rate of 10 mV s^{-1}. The potential window of gold is determined typically between 0.15 and 0.7 V [203]. The values of EDL capacitances were derived from CV according to formula $C_{dl} = {}^{\Delta i}/_{2\nu}$ where Δi is the

difference between the cathodic and anodic currents at the open circuit potential, and ν is the scan rate [204]. The P electrode exhibits a double layer capacitance of 24.42 $\mu F\ cm^{-2}$ whereas N electrode shows a double layer capacitance 158.64 $\mu F\ cm^{-2}$.

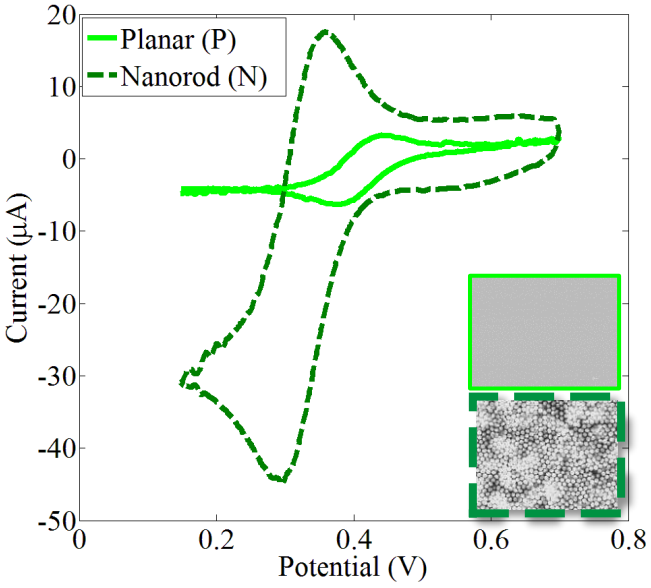

Figure 6.12. Cyclic voltammograms of 500 μm diameter P (solid line) and N deposited (dashed line) electrodes. The solutions are 2mM $K_3[Fe(CN)_6]$ in 0.1 M KCl. Scan rate is 10 mV s^{-1}. Inset figures show the surface morphology of P and N coated electrodes.

Since the capacitance is directly proportional to the surface area, the ratio of EDL capacitances provides C and it is $C = 6.50$. This number is reasonably consistent with the analytically calculated number as the surface enlargement factor ($C = 6.71 \pm 0.40$) . The error is calculated to be 2.98%, which may arise from the non-uniformity of relevant dimensions. In addition, location of the current peaks in Figure 6.11 is shifted to the left for N electrode compared to the P electrode. The reason for this can be the nickel base layer of the N electrode.

Further nondimensionalization of the frequency axis using τ_n for N and τ_c for P electrodes, interfacial impedance spectra collapsed on the same line (Figure 6.12a and 6.12b).

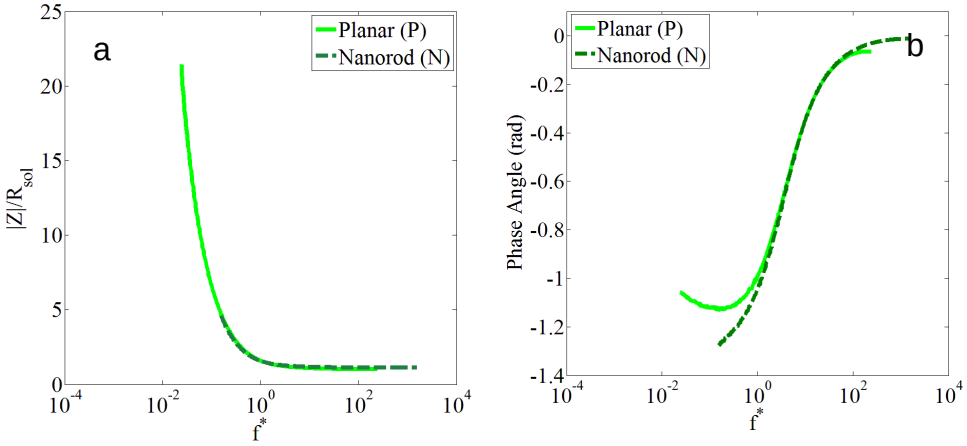

Figure 6.13. Normalized impedance values (a) and phase angles (b) after the dimensionless frequency of N is multiplied with the surface enlargement factor (C=6.5).

A discrepancy was observed in the phase angle spectrum at low frequencies ($< 1\ kHz$). The phase angle of the P electrode shows an inflection point and then it tends to be more resistive at low frequencies. This behavior was observed for all P electrodes except the 2 mm diameter electrode, and hence, it is considered to be an electrode size dependent behavior [51].

The impedance of the 85 nm diameter P and N electrodes in a 137mM KCl solution was simulated to investigate the coupled effect of surface enlargement factor and electrode diameter. Nanorod dimensions were kept the same with those measured using MIST. The boundary conditions and simulation domain are shown in Figure 6.13.

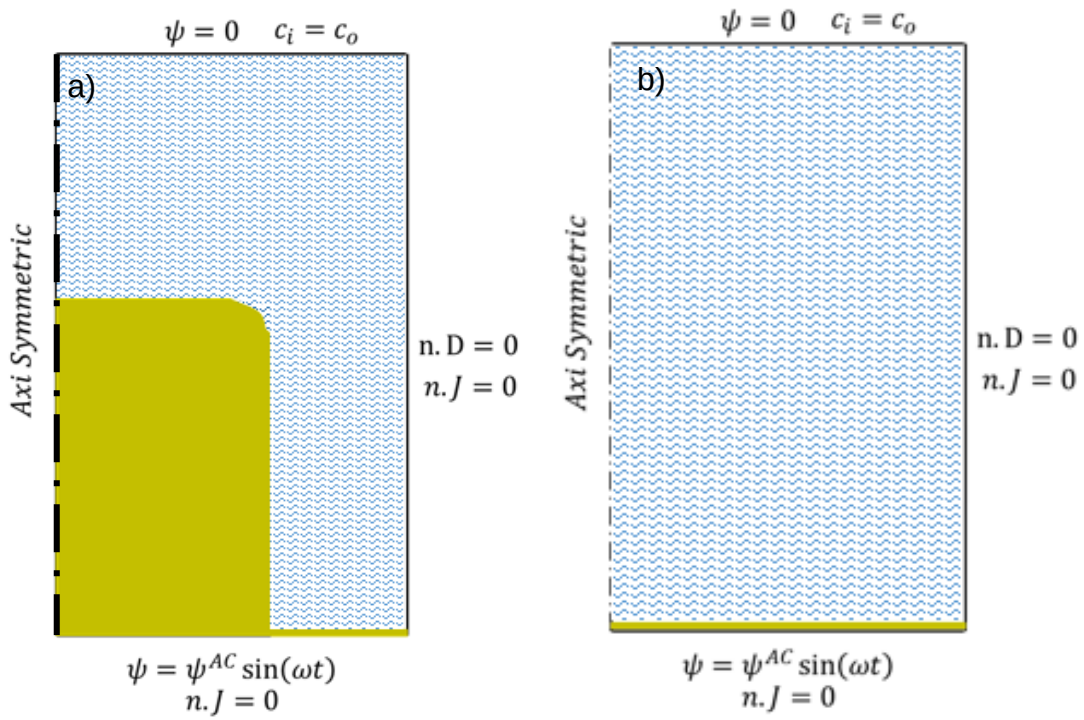

Figure 6.14. Computational domain and boundary conditions for gold nanorod (a) and planar electrodes. (b)Yellow region represent the electrodes in contact with an electrolyte. Figure 6.14 shows the normalized impedance magnitude (a) and phase angle (b) before the characteristic time scale is multiplied with the C.

As expected, the impedance magnitude for the N electrode at low frequency ranges is smaller than the impedance of the smooth P electrode. On the other hand, the obtained phase angle of the N electrode was greater than the phase angle of P electrode. This behavior is consistent with the experimental results. Then, the characteristic time was scaled with the surface enlargement factor for the N electrode, while it was kept as a unity for P electrode. The use of the surface enlargement factor in the scaling is confirmed by the collapse of the impedance spectra at all normalized frequencies (Figure 6.14c and 14d).

The CPE model, in series with solution resistance was used to model this self-similar behavior for disk electrodes [46].

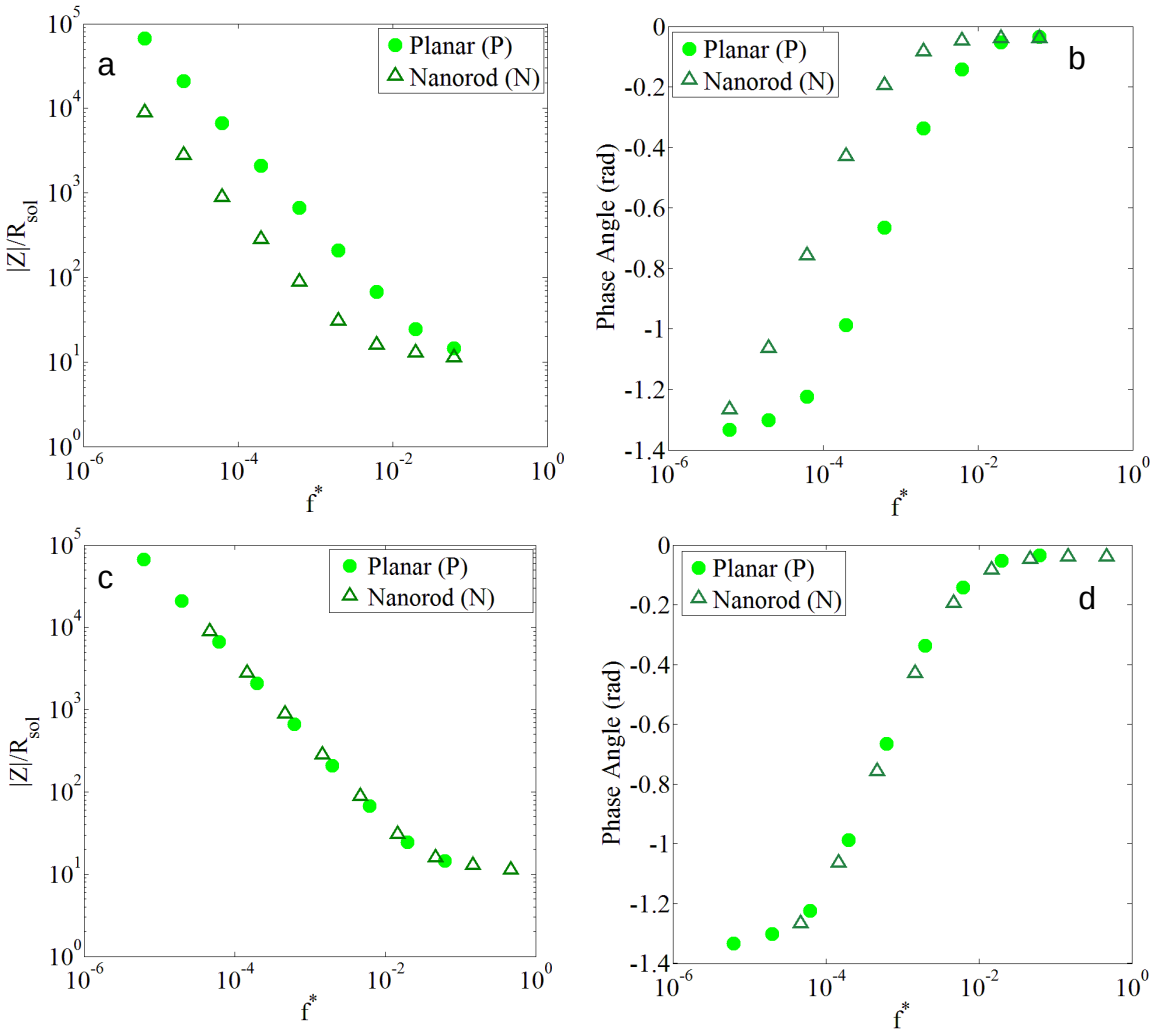

Figure 6.15. Normalized impedance values (a) and phase angles (b) obtained with P (circles) and N (triangles) electrodes at 137mM KCl solution. Normalized impedance values (c) and phase angles (d) after the dimensionless frequency of N is multiplied with the surface enlargement factor (C=6.5).

The normalized total interfacial impedance and solution resistance are given as

$$Z^* = 1 + Z^*_{CPE} = 1 + \frac{1}{K(i\omega^*)^\alpha} \tag{6.12}$$

where K and α are the CPE coefficient and exponent, respectively, ω^* is the normalized angular frequency ($2\pi f^*$), and i is $\sqrt{-1}$. The parameter α changes from zero to one ($0 \leq \alpha \leq 1$), corresponding to purely resistive ($\alpha = 0$) and purely capacitive ($\alpha = 1$) EDL in the two limits [197].

For the fitting procedure, a non-linear least square algorithm was employed in MATLAB to find the best K and α values that yields the least difference between the real and imaginary parts of the model and experimental data [42]. Based on the fitting results, the following equation can be used for all electrode diameters and solution conductivities for both the P and N electrode cases.

$$Z^* = 1 + \frac{5.291}{(i\omega^*)^{0.7645}} \tag{6.13}$$

Figure 6.15 shows the normalized impedance magnitude (a) and phase angle (b) versus dimensionless frequency for the model and experimental data. The proposed CPE model predicts normalized impedance magnitude over the entire frequency spectrum. On the other hand, phase angle shows variations due to the alteration of its characteristic at low frequency spectrum. The highest error in the model happens for the phase angle, and it is 9.33% at the lowest dimensionless frequency.

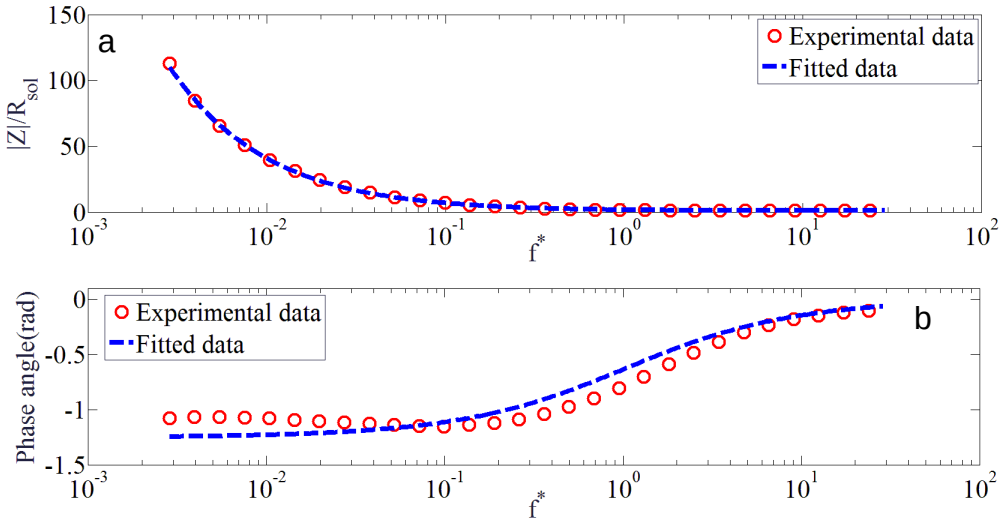

Figure 6.16. Normalized impedance magnitude (a) and phase angle (b) versus dimensionless frequency for CPE model and experimental data.

6.3. Conclusions

Electrical impedance measurements were conducted for P and N disk electrodes to investigate the coupled effects of electrode diameter, electrolyte conductivity, and surface morpholgy on the EDL charging time scale and to assess the EP. The impedance magnitude scales with the spreading resistance that is inversely proportional to the electrode diameter and electrolyte conductivity. All impedance data converges to the spreading resistance values at high frequencies, while the EP induces further increase in impedance at low frequency, which is amplified with increased ionic conductivity and reduced electrode size. The EP is affected by the EDL charging time, which is proportional to the electrode diameter and Debye length, and it is inversely proportional to the ionic diffusivity. Nanorods increases the EDL charging time by the surface enlargement factor, when the

surface morphology does not allow EDL overlap. This study validates the importance of spreading resistance on electrical impedance of electrodes, and introduces a relevant EDL charging time scale. It also presents self-similarity of properly normalized impedance, where all data collapses on to a single curve that can be modelled using a constant phase element model. This universal behavior will enable further theoretical predictions and practical outcomes. For example, limited experiments can be performed using larger electrode size but at high ionic conductivity media to obtain impedance data with EP effect. After creating a dimensionless impedance versus frequency model one can predict the behavior of impedance for any other electrode diameter or ionic conductivity. Future work will include investigation of the nanorod effects under EDL overlap.

Chapter 7

SUMMARY AND FUTURE RESEARCH

This chapter summarizes the main contributions of the presents study and makes recommendations for future work beyond the results reported in the thesis.

7.1 Summary of the current work

EP at the electrode/electrolyte interface is often undesirable for bio-sensing applications, where charge accumulated over an electrode at constant potential causes large potential drop at the interface and low measurement sensitivity. In this dissertation, the electrode polarization effect is deeply investigated experimentally, numerically and analytically by considering electrode shape, size, surface morphology, solution type and channel height. Different diameters of electrodes were used to investigate the size effect on EP with a parallel plate electrode configuration. Surface of electrodes were electrochemically deposited with distinct shape gold nanostructures to reduce the EP effect and the best performance was obtained with using dendritic shape fern leaf like gold nanostructures. Then, impedance spectra of disk electrodes with different electrode configurations were normalized with R_{sol} and the frequency was nondimensionalized with the characteristic charging time scales. The results revealed a universal impedance behavior for both parallel plate capacitor and single electrode configurations. A crucial aspect of this finding was the similarity between the impedance spectra for rough and planar electrodes in high and low conductivity media, respectively. Mainly, the nanostructured electrodes in high

conductivity electrolytes with thin electrical double layer (EDL) behaved similar to planar electrodes in low conductivity medium with thick EDL.

The models and results given here are useful to build the design of microfluidic biosensors and to provide strategies for optimizing the electrode geometry and surface morphology for a selected conductive media. A scaling law can be used to predict the frequency limitation of microfluidic device prior to fabrication and it can be useful for designing various practical electrochemical systems for a wide range of applications.

7.2 Future Research

In the future work, analytical solution will be extended for single disk electrodes. The analytical solution will be extended for high applied voltages and the results will be compared with those obtained solving MPNP. Surface charge density will be measured using the atomic force microscopy method and results will be compared with the derived analytical expression. Furthermore, impedance measurements will be repeated to investigate the EDL overlapped on impedance spectra. These measurements will be conducted using electrodes with different nanorod separation distances and at various ionic concentrations chosen to induce a thin EDL that does *not* overlap on the nano-rod surfaces. This will test the effects of electrode-area increase compared to the planar electrodes; using ionic conductivities that enable the EDL overlap due to the fine nanorod spacing, we will test the “thickened EDL” hypothesis.

References

1. Schmickler, W. and E. Santos, *Interfacial electrochemistry*. 2010: Springer Science & Business Media.
2. Hunter, R.J., *Foundations of colloid science*. 2001: Oxford university press.
3. Jue, T., *Modern Tools of Biophysics*. Vol. 5. 2017: Springer.
4. Karniadakis, G., A. Beskok, and N. Aluru, *Microflows and nanoflows: fundamentals and simulation*. Vol. 29. 2006: Springer Science & Business Media.
5. Koklu, A., A. Mansoorifar, and A. Beskok, *Effects of electrode size and surface morphology on electrode polarization in physiological buffers.* Electrophoresis, 2018.
6. Breitsprecher, K., C. Holm, and S. Kondrat, *Charge Me Slowly, I Am in a Hurry: Optimizing Charge–Discharge Cycles in Nanoporous Supercapacitors.* ACS nano, 2018. **12**(10): p. 9733-9741.
7. Simon, P. and Y. Gogotsi, *Materials for electrochemical capacitors*, in *Nanoscience And Technology: A Collection of Reviews from Nature Journals*. 2010, World Scientific. p. 320-329.
8. Deng, D., et al., *Water purification by shock electrodialysis: Deionization, filtration, separation, and disinfection.* Desalination, 2015. **357**: p. 77-83.
9. Nguyen, C.T. and A. Beskok, *Charged nanoporous graphene membranes for water desalination.* Physical Chemistry Chemical Physics, 2019. **21**(18): p. 9483-9494.
10. Nguyen, C.T. and A. Beskok, *Saltwater transport through pristine and positively charged graphene membranes.* The Journal of chemical physics, 2018. **149**(2): p. 024704.
11. Janssen, M., A. Härtel, and R. Van Roij, *Boosting capacitive blue-energy and desalination devices with waste heat.* Physical review letters, 2014. **113**(26): p. 268501.
12. Härtel, A., et al., *Heat-to-current conversion of low-grade heat from a thermocapacitive cycle by supercapacitors.* Energy & Environmental Science, 2015. **8**(8): p. 2396-2401.
13. Sabuncu, A.C., et al., *Microfluidic impedance spectroscopy as a tool for quantitative biology and biotechnology.* Biomicrofluidics, 2012. **6**(3): p. 034103.
14. Zhang, X., et al., *The influence of the electrode dimension on the detection sensitivity of electric cell–substrate impedance sensing (ECIS) and its mathematical modeling.* Sensors and Actuators B: Chemical, 2017. **247**: p. 780-790.
15. Basuray, S., et al., *Shear and AC field enhanced carbon nanotube impedance assay for rapid, sensitive, and mismatch-discriminating DNA hybridization.* ACS nano, 2009. **3**(7): p. 1823-1830.
16. Buie, C.R., et al., *Water management in proton exchange membrane fuel cells using integrated electroosmotic pumping.* Journal of Power Sources, 2006. **161**(1): p. 191-202.

17. Pilon, L., H. Wang, and A. d'Entremont, *Recent advances in continuum modeling of interfacial and transport phenomena in electric double layer capacitors.* Journal of The Electrochemical Society, 2015. **162**(5): p. A5158-A5178.
18. Biesheuvel, P., et al., *Theory of membrane capacitive deionization including the effect of the electrode pore space.* Journal of colloid and interface science, 2011. **360**(1): p. 239-248.
19. Brogioli, D., *Extracting renewable energy from a salinity difference using a capacitor.* Physical review letters, 2009. **103**(5): p. 058501.
20. Lisdat, F. and D. Schäfer, *The use of electrochemical impedance spectroscopy for biosensing.* Analytical and Bioanalytical Chemistry, 2008. **391**(5): p. 1555.
21. Varshney, M. and Y. Li, *Interdigitated array microelectrodes based impedance biosensors for detection of bacterial cells.* Biosensors and bioelectronics, 2009. **24**(10): p. 2951-2960.
22. Chuang, C.-H., et al., *A rapid and sensitive impedance-based immunosensor utilizing dielectrophoretic manipulations of polyaniline modified nanoprobes.* IEEE Sensors Journal, 2016. **16**(11): p. 4166-4173.
23. Mansoorifar, A., et al., *Dielectrophoresis assisted loading and unloading of microwells for impedance spectroscopy.* Electrophoresis, 2017.
24. Fernandez, R.E., et al., *Flexible bioimpedance sensor for label-free detection of cell viability and biomass.* IEEE transactions on nanobioscience, 2015. **14**(7): p. 700-706.
25. De Ninno, A., et al., *Coplanar electrode microfluidic chip enabling accurate sheathless impedance cytometry.* Lab on a Chip, 2017. **17**(6): p. 1158-1166.
26. Valiūnienė, A., et al., *Fast Fourier transformation electrochemical impedance spectroscopy for the investigation of inactivation of glucose biosensor based on graphite electrode modified by Prussian blue, polypyrrole and glucose oxidase.* Colloids and Surfaces A: Physicochemical and Engineering Aspects, 2017.
27. Rosu-Hamzescu, M., et al. *High Performance Low Cost Impedance Spectrometer for Biosensing*. in *Control Systems and Computer Science (CSCS), 2017 21st International Conference on*. 2017. IEEE.
28. Lu, Y., et al., *Flexible Neural Electrode Array Based-on Porous Graphene for Cortical Microstimulation and Sensing.* Scientific reports, 2016. **6**.
29. Frey, U., et al. *An 11k-electrode 126-channel high-density microelectrode array to interact with electrogenic cells*. in *Solid-State Circuits Conference, 2007. ISSCC 2007. Digest of Technical Papers. IEEE International*. 2007. IEEE.
30. Ogihara, N., et al., *Impedance spectroscopy characterization of porous electrodes under different electrode thickness using a symmetric cell for high-performance lithium-ion batteries.* The Journal of Physical Chemistry C, 2015. **119**(9): p. 4612-4619.
31. Chu, S. and A. Majumdar, *Opportunities and challenges for a sustainable energy future.* nature, 2012. **488**(7411): p. 294.
32. Yazicioglu, R.F., et al., *Low-Power Biomedical Interfaces*, in *Efficient Sensor Interfaces, Advanced Amplifiers and Low Power RF Systems*. 2016, Springer. p. 81-101.

33. Mardanpour, M.M. and S. Yaghmaei, *Characterization of a microfluidic microbial fuel cell as a power generator based on a nickel electrode.* Biosensors and Bioelectronics, 2016. **79**: p. 327-333.
34. Morgan, H., et al., *Single cell dielectric spectroscopy.* Journal of Physics D: Applied Physics, 2006. **40**(1): p. 61.
35. Cheung, K., S. Gawad, and P. Renaud, *Impedance spectroscopy flow cytometry: on-chip label-free cell differentiation.* Cytometry Part A, 2005. **65**(2): p. 124-132.
36. Asami, K., *Characterization of biological cells by dielectric spectroscopy.* Journal of Non-Crystalline Solids, 2002. **305**(1): p. 268-277.
37. Pethig, R., *Dielectric and electrical properties of biological materials.* Journal of Bioelectricity, 1985. **4**(2): p. vii-ix.
38. Tang, W., et al., *Microfluidic Impedance Cytometer with Inertial Focusing and Liquid Electrodes for High-Throughput Cell Counting and Discrimination.* Analytical Chemistry, 2017. **89**(5): p. 3154-3161.
39. Yang, L., *Electrical impedance spectroscopy for detection of bacterial cells in suspensions using interdigitated microelectrodes.* Talanta, 2008. **74**(5): p. 1621-1629.
40. Ruan, C., L. Yang, and Y. Li, *Immunobiosensor chips for detection of Escherichia c oli O157: H7 using electrochemical impedance spectroscopy.* Analytical Chemistry, 2002. **74**(18): p. 4814-4820.
41. Asami, K., T. Hanai, and N. Koizumi, *Dielectric properties of yeast cells.* Journal of Membrane Biology, 1976. **28**(1): p. 169-180.
42. Mansoorifar, A., et al., *Accuracy of the Maxwell-Wagner and the Bruggeman-Hanai Mixture Models for Single Cell Dielectric Spectroscopy.* IET Nanobiotechnology, 2017.
43. Schwan, H., *Linear and nonlinear electrode polarization and biological materials.* Annals of biomedical engineering, 1992. **20**(3): p. 269-288.
44. Schwan, H., *Electrode polarization impedance and measurements in biological materials.* Annals of the New York Academy of Sciences, 1968. **148**(1): p. 191-209.
45. Serghei, A., et al., *Electrode polarization and charge transport at solid interfaces.* Physical Review B, 2009. **80**(18): p. 184301.
46. Koklu, A., A.C. Sabuncu, and A. Beskok, *Rough gold electrodes for decreasing impedance at the electrolyte/electrode interface.* Electrochimica acta, 2016. **205**: p. 215-225.
47. Franks, W., et al., *Impedance characterization and modeling of electrodes for biomedical applications.* IEEE Transactions on Biomedical Engineering, 2005. **52**(7): p. 1295-1302.
48. Rahman, A.R.A., D.T. Price, and S. Bhansali, *Effect of electrode geometry on the impedance evaluation of tissue and cell culture.* Sensors and Actuators B: Chemical, 2007. **127**(1): p. 89-96.
49. Malleo, D., et al., *Note: Characterization of electrode materials for dielectric spectroscopy.* Review of Scientific Instruments, 2010. **81**(1): p. 016104.
50. Newman, J., *Resistance for flow of current to a disk.* 1965.
51. Ahuja, A.K., et al., *The dependence of spectral impedance on disc microelectrode radius.* IEEE Transactions on Biomedical Engineering, 2008. **55**(4): p. 1457-1460.

52. El Hasni, A., et al., *Electrical impedance spectroscopy of single cells in hydrodynamic traps.* Sensors and Actuators B: Chemical, 2017. **248**: p. 419-429.
53. Alexander, C.L., B. Tribollet, and M.E. Orazem, *Contribution of surface distributions to constant-phase-element (CPE) behavior: 1. Influence of roughness.* Electrochimica Acta, 2015. **173**: p. 416-424.
54. Alexander, C.L., B. Tribollet, and M.E. Orazem, *Contribution of surface distributions to constant-phase-element (CPE) behavior: 2. Capacitance.* Electrochimica Acta, 2016. **188**: p. 566-573.
55. Alexander, C.L., B. Tribollet, and M.E. Orazem, *Influence of micrometric-scale electrode heterogeneity on electrochemical impedance spectroscopy.* Electrochimica Acta, 2016. **201**: p. 374-379.
56. Koklu, A., A. Mansoorifar, and A. Beskok, *Self-Similar Interfacial Impedance of Electrodes in High Conductivity Media.* Analytical Chemistry, 2017.
57. Park, H., P. Takmakov, and H. Lee, *Electrochemical evaluations of fractal microelectrodes for energy efficient neurostimulation.* Scientific reports, 2018. **8**(1): p. 4375.
58. Lim, K.-H. and E.I. Franses, *Electrical properties of aqueous dispersions of polymer microspheres.* Journal of colloid and interface science, 1986. **110**(1): p. 201-213.
59. Schwan, H.P. and C.D. Ferris, *Four-electrode null techniques for impedance measurement with high resolution.* Review of scientific instruments, 1968. **39**(4): p. 481-485.
60. Farkhondeh, M., et al., *Method of the Four-Electrode Electrochemical Cell for the Characterization of Concentrated Binary Electrolytes: Theory and Application.* The Journal of Physical Chemistry C, 2017. **121**(8): p. 4112-4129.
61. Feldman, Y., et al., *Fractal-polarization correction in time domain dielectric spectroscopy.* Physical Review E, 1998. **58**(6): p. 7561.
62. Madou, M.J. and R. Cubicciotti, *Scaling issues in chemical and biological sensors.* Proceedings of the IEEE, 2003. **91**(6): p. 830-838.
63. Jäckel, F., A. Kinkhabwala, and W. Moerner, *Gold bowtie nanoantennas for surface-enhanced Raman scattering under controlled electrochemical potential.* Chemical Physics Letters, 2007. **446**(4): p. 339-343.
64. Wu, H.-L., C.-H. Chen, and M.H. Huang, *Seed-mediated synthesis of branched gold nanocrystals derived from the side growth of pentagonal bipyramids and the formation of gold nanostars.* Chemistry of Materials, 2008. **21**(1): p. 110-114.
65. Zhao, N., et al., *Controlled synthesis of gold nanobelts and nanocombs in aqueous mixed surfactant solutions.* Langmuir, 2008. **24**(3): p. 991-998.
66. Fernandez, R.E., et al., *Platinum black electrodeposited thread based electrodes for dielectrophoretic assembly of microparticles.* Biomicrofluidics, 2016. **10**(3): p. 033101.
67. Ye, W., et al., *Template-free and direct electrochemical deposition of hierarchical dendritic gold microstructures: growth and their multiple applications.* The Journal of Physical Chemistry C, 2010. **114**(37): p. 15617-15624.
68. Guo, S., L. Wang, and E. Wang, *Templateless, surfactantless, simple electrochemical route to rapid synthesis of diameter-controlled 3D flowerlike gold*

microstructure with "clean" surface. Chemical Communications, 2007(30): p. 3163-3165.
69. Wang, L., et al., *Facile electrochemical approach to fabricate hierarchical flowerlike gold microstructures: Electrodeposited superhydrophobic surface.* Electrochemistry Communications, 2008. **10**(1): p. 95-99.
70. Xu, X., et al., *A templateless, surfactantless, simple electrochemical route to a dendritic gold nanostructure and its application to oxygen reduction.* Langmuir, 2010. **26**(10): p. 7627-7631.
71. Ye, W., et al., *Electrochemical growth of flowerlike gold nanoparticles on polydopamine modified ITO glass for SERS application.* Electrochimica Acta, 2010. **55**(6): p. 2004-2009.
72. Rahman, M.R., T. Okajima, and T. Ohsaka, *Fabrication of Au (111) nanoparticle-like electrode through a seed-mediated growth.* Chemical Communications, 2010. **46**(28): p. 5172-5174.
73. Othman, S.H., et al., *Novel procedure for the fabrication of gold nanostructures enriched in Au (110) facet orientation.* Electrochemistry Communications, 2009. **11**(6): p. 1273-1276.
74. Oyama, T., T. Okajima, and T. Ohsaka, *Electrodeposition of gold at glassy carbon electrodes in room-temperature ionic liquids.* Journal of the Electrochemical Society, 2007. **154**(6): p. D322-D327.
75. Koklu, A., A.C. Sabuncu, and A. Beskok, *Enhancement of dielectrophoresis using fractal gold nanostructured electrodes.* Electrophoresis, 2017. **38**(11): p. 1458-1465.
76. Xu, L.-P., et al., *Fractal gold modified electrode for ultrasensitive thrombin detection.* Nanoscale, 2012. **4**(12): p. 3786-3790.
77. Zhang, P. and S. Wang, *Designing fractal nanostructured biointerfaces for biomedical applications.* ChemPhysChem, 2014. **15**(8): p. 1550-1561.
78. Manthiram, K., Y. Surendranath, and A.P. Alivisatos, *Dendritic assembly of gold nanoparticles during fuel-forming electrocatalysis.* Journal of the American Chemical Society, 2014. **136**(20): p. 7237-7240.
79. Lin, T.-H., et al., *Potential-controlled electrodeposition of gold dendrites in the presence of cysteine.* Chemical Communications, 2011. **47**(7): p. 2044-2046.
80. Bardhan, R., et al., *Au nanorice assemble electrolytically into mesostars.* Acs Nano, 2009. **3**(2): p. 266-272.
81. Chang, C.-C., et al., *Hydrothermal synthesis of monodispersed octahedral gold nanocrystals with five different size ranges and their self-assembled structures.* Chemistry of Materials, 2008. **20**(24): p. 7570-7574.
82. Ha, T.H., H.-J. Koo, and B.H. Chung, *Shape-controlled syntheses of gold nanoprisms and nanorods influenced by specific adsorption of halide ions.* The Journal of Physical Chemistry C, 2007. **111**(3): p. 1123-1130.
83. Xie, J., J.Y. Lee, and D.I. Wang, *Synthesis of single-crystalline gold nanoplates in aqueous solutions through biomineralization by serum albumin protein.* The Journal of Physical Chemistry C, 2007. **111**(28): p. 10226-10232.
84. Hernández, J., et al., *Characterization of the surface structure of gold nanoparticles and nanorods using structure sensitive reactions.* The Journal of Physical Chemistry B, 2005. **109**(26): p. 12651-12654.

85. Murphy, C.J., et al., *Anisotropic metal nanoparticles: synthesis, assembly, and optical applications*, 2005, ACS Publications.
86. HianáTeo, H., *3D dendritic gold nanostructures: seeded growth of a multi-generation fractal architecture.* Chemical Communications, 2010. **46**(38): p. 7112-7114.
87. Qin, Y., et al., *Ionic liquid-assisted growth of single-crystalline dendritic gold nanostructures with a three-fold symmetry.* Chemistry of Materials, 2008. **20**(12): p. 3965-3972.
88. Lim, B., et al., *Pd-Pt bimetallic nanodendrites with high activity for oxygen reduction.* science, 2009. **324**(5932): p. 1302-1305.
89. Wen, X., et al., *Dendritic nanostructures of silver: facile synthesis, structural characterizations, and sensing applications.* Langmuir, 2006. **22**(10): p. 4836-4842.
90. Qiu, R., et al., *CuNi dendritic material: synthesis, mechanism discussion, and application as glucose sensor.* Chemistry of materials, 2007. **19**(17): p. 4174-4180.
91. Choi, B.G., et al., *3D macroporous graphene frameworks for supercapacitors with high energy and power densities.* ACS nano, 2012. **6**(5): p. 4020-4028.
92. Arico, A.S., et al., *Nanostructured materials for advanced energy conversion and storage devices*, in *Materials For Sustainable Energy: A Collection of Peer-Reviewed Research and Review Articles from Nature Publishing Group*. 2011, World Scientific. p. 148-159.
93. Yasui, K., K. Nishio, and H. Masuda, *Fabrication of nanocomposites by filling nanoholes in highly ordered anodic porous alumina by vacuum deposition of metal.* Japanese journal of applied physics, 2005. **44**(9L): p. L1181.
94. Zhang, L., P. Zhang, and Y. Fang, *Magnetron sputtering of silver nanowires using anodic aluminum oxide template: A new active substrate of surface enhanced Raman scattering and an investigation of its enhanced mechanism.* Analytica chimica acta, 2007. **591**(2): p. 214-218.
95. Choi, J., et al., *Hexagonally arranged monodisperse silver nanowires with adjustable diameter and high aspect ratio.* Chemistry of materials, 2003. **15**(3): p. 776-779.
96. Matsui, S., *Three-dimensional nanostructure fabrication by focused ion beam chemical vapor deposition*, in *Springer Handbook of Nanotechnology*. 2007, Springer. p. 179-196.
97. Noy, A., et al., *Fabrication of luminescent nanostructures and polymer nanowires using dip-pen nanolithography.* Nano letters, 2002. **2**(2): p. 109-112.
98. Krishnamoorthy, T., V. Thavasi, and S. Ramakrishna, *A first report on the fabrication of vertically aligned anatase TiO 2 nanowires by electrospinning: Preferred architecture for nanostructured solar cells.* Energy & Environmental Science, 2011. **4**(8): p. 2807-2812.
99. Lin, Y., et al., *Fabrication and optical properties of TiO2 nanowire arrays made by sol–gel electrophoresis deposition into anodic alumina membranes.* Journal of Physics: Condensed Matter, 2003. **15**(17): p. 2917.
100. Liu, L., M. Hasan, and G. Kumar, *Metallic glass nanostructures: fabrication, properties, and applications.* Nanoscale, 2014. **6**(4): p. 2027-2036.

101. Zaraska, L., G.D. Sulka, and M. Jaskuła, *Porous anodic alumina membranes formed by anodization of AA1050 alloy as templates for fabrication of metallic nanowire arrays.* Surface and coatings technology, 2010. **205**(7): p. 2432-2437.
102. Guiliani, J., J. Cadena, and C. Monton, *Template-assisted electrodeposition of Ni and Ni/Au nanowires on planar and curved substrates.* Nanotechnology, 2018. **29**(7): p. 075301.
103. Janssen, M. and M. Bier, *Transient dynamics of electric double-layer capacitors: Exact expressions within the Debye-Falkenhagen approximation.* Physical Review E, 2018. **97**(5): p. 052616.
104. Golovnev, A. and S. Trimper, *Analytical solution of the PNP equations at AC applied voltage.* Physics Letters A, 2012. **376**(16): p. 1391-1395.
105. Golovnev, A. and S. Trimper, *Exact solution of the Poisson–Nernst–Planck equations in the linear regime.* The Journal of chemical physics, 2009. **131**(11): p. 114903.
106. Golovnev, A. and S. Trimper, *Analytical solution of the Poisson–Nernst–Planck equations in the linear regime at an applied dc-voltage.* The Journal of chemical physics, 2011. **134**(15): p. 154902.
107. Gouy, M., *Sur la constitution de la charge électrique à la surface d'un électrolyte.* J. Phys. Theor. Appl., 1910. **9**(1): p. 457-468.
108. Chapman, D.L., *LI. A contribution to the theory of electrocapillarity.* The London, Edinburgh, and Dublin philosophical magazine and journal of science, 1913. **25**(148): p. 475-481.
109. Helmholtz, H.V., *Studien über electrische Grenzschichten.* Annalen der Physik, 1879. **243**(7): p. 337-382.
110. Bazant, M.Z., K. Thornton, and A. Ajdari, *Diffuse-charge dynamics in electrochemical systems.* Physical review E, 2004. **70**(2): p. 021506.
111. Zhang, C., et al., *An analysis of electric double layers near comb electrodes using the linearized Poisson-Nernst-Planck theory.* Journal of Applied Physics, 2017. **121**(4): p. 044502.
112. Singh, M.B. and R. Kant, *Debye–Falkenhagen dynamics of electric double layer in presence of electrode heterogeneities.* Journal of Electroanalytical Chemistry, 2013. **704**: p. 197-207.
113. Barbero, G., et al., *Role of the adsorption phenomenon on the ionic equilibrium distribution and on the transient effects in electrolytic cells.* The Journal of Physical Chemistry B, 2006. **110**(36): p. 17889-17897.
114. Van Soestbergen, M., P. Biesheuvel, and M. Bazant, *Diffuse-charge effects on the transient response of electrochemical cells.* Physical Review E, 2010. **81**(2): p. 021503.
115. Bichat, M., E. Raymundo-Piñero, and F. Béguin, *High voltage supercapacitor built with seaweed carbons in neutral aqueous electrolyte.* Carbon, 2010. **48**(15): p. 4351-4361.
116. Anil, K., et al., *Fractal gold-based microelectrode arrays for in vitro recording and stimulation from neuronal networks.* Nanotechnology, 2019.
117. Mansoorifar, A., et al., *Electrical Impedance Measurements of Biological Cells in Response to External Stimuli.* Analytical chemistry, 2018. **90**(7): p. 4320-4327.

118. Mansoorifar, A., A. Koklu, and A. Beskok, *Quantification of Cell Death Using an Impedance-Based Microfluidic Device.* Analytical chemistry, 2019.
119. Mansoorifar, A., et al., *Dielectrophoresis assisted loading and unloading of microwells for impedance spectroscopy.* Electrophoresis, 2017. **38**(11): p. 1466-1474.
120. Buck, R., *Diffuse layer charge relaxation at the ideally polarized electrode.* Journal of Electroanalytical Chemistry and Interfacial Electrochemistry, 1969. **23**(2): p. 219-240.
121. Ferguson, T.R. and M.Z. Bazant, *Nonequilibrium thermodynamics of porous electrodes.* Journal of The Electrochemical Society, 2012. **159**(12): p. A1967-A1985.
122. Newman, J. and W. Tiedemann, *Porous-electrode theory with battery applications.* AIChE Journal, 1975. **21**(1): p. 25-41.
123. Bazant, M.Z., *Theory of chemical kinetics and charge transfer based on nonequilibrium thermodynamics.* arXiv preprint arXiv:1208.1587, 2012.
124. Bai, P. and M.Z. Bazant, *Charge transfer kinetics at the solid-solid interface in porous electrodes.* arXiv preprint arXiv:1404.0859, 2014.
125. Ferguson, T.R. and M.Z. Bazant, *Phase transformation dynamics in porous battery electrodes.* Electrochimica Acta, 2014. **146**: p. 89-97.
126. Dydek, E. and M.Z. Bazant, *Nonlinear dynamics of ion concentration polarization in porous media: The leaky membrane model.* AIChE Journal, 2013. **59**(9): p. 3539-3555.
127. Bard, A.J. and L.R. Faulkner, *Fundamentals and applications.* Electrochemical Methods, 2001. **2**: p. 482.
128. Butt, H.-J. and M. Kappl, *Surface and interfacial forces*. 2010: Wiley Online Library.
129. Bagotsky, V.S., *Fundamentals of electrochemistry*. Vol. 44. 2005: John Wiley & Sons.
130. Young, H.D., et al., *University physics*. Vol. 9. 1996: Addison-Wesley Reading, MA.
131. Huang, J., et al., *Curvature effects in carbon nanomaterials: Exohedral versus endohedral supercapacitors.* Journal of Materials Research, 2010. **25**(8): p. 1525-1531.
132. Masliyah, J.H. and S. Bhattacharjee, *Electrokinetic and colloid transport phenomena*. 2006: John Wiley & Sons.
133. Guoy, G., *Constitution of the electric charge at the surface of an electrolyte.* J Physique, 1910. **9**: p. 457-67.
134. Lyklema, J., *Fundamentals of interface and colloid science. Volume 2: Solid-liquid interfaces. With special contributions by A. de Keizer, BH Bijsterbosch, GJ Fleer and MA Cohen Stuart.* 1995.
135. Ohshima, H., *Theory of colloid and interfacial electric phenomena*. Vol. 12. 2006: Elsevier.
136. Huang, J., et al., *Effect of diffuse layer and pore shapes in mesoporous carbon supercapacitors.* Journal of Materials Research, 2010. **25**(8): p. 1469-1475.

137. Bazant, M.Z., et al., *Towards an understanding of induced-charge electrokinetics at large applied voltages in concentrated solutions.* Advances in colloid and interface science, 2009. **152**(1-2): p. 48-88.
138. Vlachy, V., *Ionic effects beyond Poisson-Boltzmann theory.* Annual review of physical chemistry, 1999. **50**(1): p. 145-165.
139. Kornyshev, A.A., *Double-layer in ionic liquids: paradigm change?*, 2007, ACS Publications.
140. Bikerman, J., *XXXIX. Structure and capacity of electrical double layer.* The London, Edinburgh, and Dublin Philosophical Magazine and Journal of Science, 1942. **33**(220): p. 384-397.
141. Borukhov, I., D. Andelman, and H. Orland, *Steric effects in electrolytes: A modified Poisson-Boltzmann equation.* Physical review letters, 1997. **79**(3): p. 435.
142. Silalahi, A.R., et al., *Comparing the Predictions of the Nonlinear Poisson− Boltzmann Equation and the Ion Size-Modified Poisson− Boltzmann Equation for a Low-Dielectric Charged Spherical Cavity in an Aqueous Salt Solution.* Journal of chemical theory and computation, 2010. **6**(12): p. 3631-3639.
143. Chu, V.B., et al., *Evaluation of ion binding to DNA duplexes using a size-modified Poisson-Boltzmann theory.* Biophysical journal, 2007. **93**(9): p. 3202-3209.
144. Biesheuvel, P.M., F.A. Leermakers, and M.A.C. Stuart, *Self-consistent field theory of protein adsorption in a non-Gaussian polyelectrolyte brush.* Physical Review E, 2006. **73**(1): p. 011802.
145. Biesheuvel, P. and J. Lyklema, *Sedimentation–diffusion equilibrium of binary mixtures of charged colloids including volume effects.* Journal of Physics: Condensed Matter, 2005. **17**(41): p. 6337.
146. Alijó, P., F. Tavares, and E. Biscaia Jr, *Double layer interaction between charged parallel plates using a modified Poisson–Boltzmann equation to include size effects and ion specificity.* Colloids and Surfaces A: Physicochemical and Engineering Aspects, 2012. **412**: p. 29-35.
147. Tresset, G., *Generalized Poisson-Fermi formalism for investigating size correlation effects with multiple ions.* Physical Review E, 2008. **78**(6): p. 061506.
148. Li, B., *Continuum electrostatics for ionic solutions with non-uniform ionic sizes.* Nonlinearity, 2009. **22**(4): p. 811.
149. Wen, J., et al., *Competitive adsorption and ordered packing of counterions near highly charged surfaces: From mean-field theory to Monte Carlo simulations.* Physical Review E, 2012. **85**(4): p. 041406.
150. López-García, J., M. Aranda-Rascón, and J. Horno, *Excluded volume effect on the electrophoretic mobility of colloidal particles.* Journal of colloid and interface science, 2008. **323**(1): p. 146-152.
151. López-García, J.J., et al., *Electrokinetics of charged spherical colloidal particles taking into account the effect of ion size constraints.* Journal of colloid and interface science, 2011. **356**(1): p. 325-330.
152. Borukhov, I., D. Andelman, and H. Orland, *Adsorption of large ions from an electrolyte solution: a modified Poisson–Boltzmann equation.* Electrochimica Acta, 2000. **46**(2-3): p. 221-229.

153. Kilic, M.S., M.Z. Bazant, and A. Ajdari, *Steric effects in the dynamics of electrolytes at large applied voltages. I. Double-layer charging.* Physical review E, 2007. **75**(2): p. 021502.
154. Pell, W. and B. Conway, *Voltammetry at a de Levie brush electrode as a model for electrochemical supercapacitor behaviour.* Journal of Electroanalytical Chemistry, 2001. **500**(1-2): p. 121-133.
155. Conway, B. and W. Pell, *Power limitations of supercapacitor operation associated with resistance and capacitance distribution in porous electrode devices.* Journal of power sources, 2002. **105**(2): p. 169-81.
156. Yoon, S., et al., *Complex capacitance analysis on rate capability of electric-double layer capacitor (EDLC) electrodes of different thickness.* Electrochimica Acta, 2005. **50**(11): p. 2255-2262.
157. Chu, K.T. and M.Z. Bazant, *Nonlinear electrochemical relaxation around conductors.* Physical Review E, 2006. **74**(1): p. 011501.
158. Olesen, L.H., M.Z. Bazant, and H. Bruus, *Strongly nonlinear dynamics of electrolytes in large ac voltages.* Physical Review E, 2010. **82**(1): p. 011501.
159. Dickinson, E.J. and R.G. Compton, *How well does simple RC circuit analysis describe diffuse double layer capacitance at smooth micro-and nanoelectrodes?* Journal of electroanalytical chemistry, 2011. **655**(1): p. 23-31.
160. Kilic, M.S., M.Z. Bazant, and A. Ajdari, *Steric effects in the dynamics of electrolytes at large applied voltages. II. Modified Poisson-Nernst-Planck equations.* Physical review E, 2007. **75**(2): p. 021503.
161. Pillay, B. and J. Newman, *The influence of side reactions on the performance of electrochemical double-layer capacitors.* Journal of the Electrochemical Society, 1996. **143**(6): p. 1806-1814.
162. Ghosal, S., *Electrokinetic flow and dispersion in capillary electrophoresis.* Annu. Rev. Fluid Mech., 2006. **38**: p. 309-338.
163. Wang, H. and L. Pilon, *Intrinsic limitations of impedance measurements in determining electric double layer capacitances.* Electrochimica Acta, 2012. **63**: p. 55-63.
164. Wang, H. and L. Pilon, *Physical interpretation of cyclic voltammetry for measuring electric double layer capacitances.* Electrochimica Acta, 2012. **64**: p. 130-139.
165. Baker-Jarvis, J., B. Riddle, and A.M. Young, *Ion dynamics near charged electrodes with excluded volume effect.* IEEE transactions on dielectrics and electrical insulation, 1999. **6**(2): p. 226-235.
166. Zhao, H., *Diffuse-charge dynamics of ionic liquids in electrochemical systems.* Physical Review E, 2011. **84**(5): p. 051504.
167. Eisenberg, B., Y. Hyon, and C. Liu, *Energy variational analysis of ions in water and channels: Field theory for primitive models of complex ionic fluids.* The Journal of Chemical Physics, 2010. **133**(10): p. 104104.
168. Lu, B., et al., *Poisson–Nernst–Planck equations for simulating biomolecular diffusion–reaction processes I: Finite element solutions.* Journal of computational physics, 2010. **229**(19): p. 6979-6994.
169. Horng, T.-L., et al., *PNP equations with steric effects: a model of ion flow through channels.* The Journal of Physical Chemistry B, 2012. **116**(37): p. 11422-11441.

170. Chu, K.T. and M.Z. Bazant, *Surface conservation laws at microscopically diffuse interfaces.* Journal of colloid and interface science, 2007. **315**(1): p. 319-329.
171. Cervera, J., V. García-Morales, and J. Pellicer, *Ion size effects on the electrokinetic flow in nanoporous membranes caused by concentration gradients.* The Journal of Physical Chemistry B, 2003. **107**(33): p. 8300-8309.
172. Aranda-Rascón, M., et al., *Influence of the finite ion size on the predictions of the standard electrokinetic model: Frequency response.* Journal of colloid and interface science, 2009. **336**(2): p. 857-864.
173. Davidson, J.D. and N. Goulbourne, *Nonlinear capacitance and electrochemical response of ionic liquid-ionic polymers.* Journal of Applied Physics, 2011. **109**(8): p. 084901.
174. Macdonald, J.R., *Impedance spectroscopy: old problems and new developments.* Electrochimica Acta, 1990. **35**(10): p. 1483-1492.
175. Geddes, L., *Historical evolution of circuit models for the electrode-electrolyte interface.* Annals of biomedical engineering, 1997. **25**(1): p. 1.
176. Pajkossy, T. and L. Nyikos, *Scaling-law analysis to describe the impedance behavior of fractal electrodes.* Physical Review B, 1990. **42**(1): p. 709.
177. Pajkossy, T., *Impedance of rough capacitive electrodes.* Journal of Electroanalytical Chemistry, 1994. **364**(1-2): p. 111-125.
178. Stoneman, M., et al., *Correction of electrode polarization contributions to the dielectric properties of normal and cancerous breast tissues at audio/radiofrequencies.* Physics in medicine and biology, 2007. **52**(22): p. 6589.
179. Bordi, F., C. Cametti, and T. Gili, *Reduction of the contribution of electrode polarization effects in the radiowave dielectric measurements of highly conductive biological cell suspensions.* Bioelectrochemistry, 2001. **54**(1): p. 53-61.
180. Lastochkin, D., et al., *Electrokinetic micropump and micromixer design based on ac faradaic polarization.* Journal of Applied Physics, 2004. **96**(3): p. 1730-1733.
181. Zhang, P., et al., *Programmable fractal nanostructured interfaces for specific recognition and electrochemical release of cancer cells.* Advanced Materials, 2013. **25**(26): p. 3566-3570.
182. Paunovic, M. and M. Schlesinger, *Fundamentals of electrochemical deposition*. Vol. 45. 2006: john wiley & sons.
183. Plieth, W., *On The Electrochemical Properties of Small Clusters of Metal Atoms and Their Role in the Surface Enhanced Raman Scattering.* Lawrence Berkeley National Laboratory, 2010.
184. Armstrong, R.D. and R. Burnham, *The effect of roughness on the impedance of the interface between a solid electrolyte and a blocking electrode.* Journal of Electroanalytical Chemistry and Interfacial Electrochemistry, 1976. **72**(3): p. 257-266.
185. Cui, X. and D.C. Martin, *Fuzzy gold electrodes for lowering impedance and improving adhesion with electrodeposited conducting polymer films.* Sensors and Actuators A: Physical, 2003. **103**(3): p. 384-394.
186. McAdams, E., et al. *Characterization of gold electrodes in phosphate buffered saline solution by impedance and noise measurements for biological applications*. in *Engineering in Medicine and Biology Society, 2006. EMBS'06. 28th Annual International Conference of the IEEE*. 2006. IEEE.

187. Valero, A., T. Braschler, and P. Renaud, *A unified approach to dielectric single cell analysis: Impedance and dielectrophoretic force spectroscopy.* Lab on a Chip, 2010. **10**(17): p. 2216-2225.
188. Mansoorifar, A., et al., *Accuracy of the Maxwell–Wagner and the Bruggeman–Hanai mixture models for single cell dielectric spectroscopy.* IET Nanobiotechnology, 2017. **11**(7): p. 874-882.
189. Haruta, H., *The impedance measurement handbook: a guide to measurement technology and techniques*. 2000: Agilent Technologies.
190. Squires, T.M., *Induced-charge electrokinetics: fundamental challenges and opportunities.* Lab on a Chip, 2009. **9**(17): p. 2477-2483.
191. Wu, S.-L., et al., *The influence of coupled faradaic and charging currents on impedance spectroscopy.* Electrochimica Acta, 2014. **131**: p. 3-12.
192. Chechirlian, S., et al., *A specific aspect of impedance measurements in low conductivity media. Artefacts and their interpretations.* Electrochimica Acta, 1990. **35**(7): p. 1125-1131.
193. Fuller, T.F., M. Doyle, and J. Newman, *Simulation and optimization of the dual lithium ion insertion cell.* Journal of the Electrochemical Society, 1994. **141**(1): p. 1-10.
194. Abramoff, M., P. Magalhaes, and S. Ram, *Image processing with ImageJ. Biophotonics Int. 11: 36–42.* Google Scholar, 2004.
195. Koklu, A., et al., *Pressure-driven water flow through hydrophilic alumina nanomembranes.* Microfluidics and Nanofluidics, 2017. **21**(7): p. 124.
196. Huang, V.M.-W., et al., *The apparent constant-phase-element behavior of an ideally polarized blocking electrode a global and local impedance analysis.* Journal of the Electrochemical Society, 2007. **154**(2): p. C81-C88.
197. Brug, G., et al., *The analysis of electrode impedances complicated by the presence of a constant phase element.* Journal of electroanalytical chemistry and interfacial electrochemistry, 1984. **176**(1-2): p. 275-295.
198. Das, S., S. Chakraborty, and S.K. Mitra, *Redefining electrical double layer thickness in narrow confinements: Effect of solvent polarization.* Physical Review E, 2012. **85**(5): p. 051508.
199. Koklu, A., A. Mansoorifar, and A. Beskok, *Self-Similar Interfacial Impedance of Electrodes in High Conductivity Media.* Analytical chemistry, 2017. **89**(22): p. 12533-12540.
200. Koklu, A., et al., *Self-Similar Interfacial Impedance of Electrodes in High Conductivity Media: II. Disk Electrodes.* Analytical chemistry, 2018. **91**(3): p. 2455-2463.
201. Valmianski, I., C. Monton, and I.K. Schuller, *Microscopy image segmentation tool: Robust image data analysis.* Review of Scientific Instruments, 2014. **85**(3): p. 033701.
202. Huwaldt, J.A. and S. Steinhorst, *Plot digitizer*, 2013.
203. Diao, P., et al., *Studies of structural disorder of self-assembled thiol monolayers on gold by cyclic voltammetry and ac impedance.* Journal of Electroanalytical Chemistry, 1999. **464**(1): p. 61-67.
204. Piret, G., et al., *3D-nanostructured boron-doped diamond for microelectrode array neural interfacing.* Biomaterials, 2015. **53**: p. 173-183.